Kinetic Model Based Factor Analysis of Cardiac ^{82}Rb PET Images for Improved Accuracy of Quantitative Myocardial Blood Flow Measurement

BY

RAN KLEIN

Thesis submitted to the

Faculty of Graduate and Postdoctoral Studies

in partial fulfillment of the requirements for the degree in

PhD degree in Electrical and Computer Engineering

School of Information Technology and Engineering

Faculty of Graduate and Postdoctoral Studies

University of Ottawa

Abstract

Coronary artery disease is a leading cause of death, is routinely diagnosed using myocardial perfusion imaging (MPI), and can be managed effectively with proper therapy. However, uniform reduction in flow throughout the heart due to disease in multiple arteries may not be detected with MPI. Myocardial blood flow (MBF) quantification using positron emission tomography (PET) can overcome this limitation, but has limited clinical application due to a need for an onsite cyclotron. [82]Rb PET MPI does not require a cyclotron and is being applied widely.

In this work, a region-of-interest (ROI) based method to quantify MBF from dynamic [82]Rb PET images was developed. Blood and myocardium time-activity-curves (TACs) were generated from dynamic PET images and used as input and output functions respectively to a tracer kinetic model. MBF was resolved by fitting the model to the TACs. The highly automated method had little operator-dependent variability of MBF. However, due to the limited resolution of PET, signal from myocardial tissue can spillover into blood regions, contaminate the blood TACs, and can degrade the accuracy of MBF.

Factor analysis (FA) can decompose dynamic images into underlying components of the image, but requires constraints to ensure physiological accuracy. A model-based FA method (MB) that incorporates the tracer kinetic model into the FA process as a constraint is developed and compared with a previously proposed minimal-structure-overlap FA method (MSO). In simulations, MB was more accurate and reproducible than MSO. In rat experiments with arterial blood sampling as a standard, MB resolves more physiologically accurate blood TACs. Structures were more reproducible with MB vs. MSO in repeat images of the same dog with variable-length [82]Rb infusion durations, and MBF estimates tended to be more reproducible.

The accuracy of MBF in humans using ROI-based and MB-based methods was evaluated using ^{15}O-water imaging as a standard, but no significant differences were found. However, MBF regional uniformity in normals was significantly improved over ROI based methods. In a patient population uniformity was not significantly different between methods, indicating that uniformity was not artificial. Thus MB based MBF values may be more sensitive to detect small changes in MBF.

Contents

Overlap Constrained Factor Analysis of Dynamic Cardiac ^{82}Rb PET Images   56

Kinetic Model-Based Factor Analysis   65

MBF Quantification Using FA   90

Discussion and Future Directions   113

References   123

List of Figures

List of Tables

Acronyms

API	Application Programming Interface
CA	Cluster Analysis
CAD	Coronary Artery Disease
CPT	Cold Pressor Test
CPU	Central Processing Unit
CT	Computer Tomography
CV	Coefficient of Variation
DV	Distribution Volume
EF	Extraction Fraction
FA	Factor Analysis
FADS	Factor Analysis of Dynamic Structures (or Sequences)
FDG	18F-Fluorodeoxyglucose
FOV	Field of View
FWHM	Full width at Half Maximum
ICA	Independent Component Analysis
GPU	Graphics Processing Unit
GUI	Graphical User Interface
HLA	Horizontal Long Axis
KM	Kinetic Model
LA	Left Atrium
LAD	Left Anterior Descending artery
LCX	Left Circumflex artery
LOR	Line Of Response
LV	Blood cavity of the Left Ventricle (of the heart)
LVBF	Left Ventricle Blood Fraction (in tissue)
MB	Model Based
MBF	Myocardial Blood Flow
ΔMBF	Difference Myocardial Flow Reserve (stress MBF – rest MBF)
MFO	Minimal Factor Overlap
MFR	Myocardial Flow Reserve (stress MBF/rest MBF)
MPI	Myocardial Perfusion Imaging
MRI	Magnetic Resonance Imaging
MSO	Minimal Spatial Overlap
MYO	Myocardium (typically of the left ventricle of the heart)
PCA	Principal Component Analysis
PET	Positron Emission Tomography
PS	Permeability-Surface area product (of the capillaries)
QA	Quality Assurance
RC	Recovery Coefficient
RCA	Right Coronary Artery
RMSE	Root Mean Squared Error
ROC	Receiver Operating Characteristic

ROI	Region Of Interest
RPC	Reproducibility Coefficient
RV	Blood Cavity of the Right ventricle (of the heart)
RVBF	Right Ventricle Blood Fraction (in tissue)
SA	Short Axis
TAC	Time-Activity-Curve
TBF	Total Blood Fraction (in tissue)
TR	Total Recovery
TV	Transverse
VLA	Vertical Long Axis

Frequently Used Variables and Notation

$C_a(t)$	Measured arterial blood TAC
$C_{meas}(t)$	Measured myocardial TAC
$C_{model}(t)$	Modeled myocardial TAC
$C_t(t)$	Modelled myocardial tissue response
N	Number of pixels in an image matrix
K	Number of factors to decompose
M	Number of time frames in a dynamic image sequence
$\boldsymbol{Y}$	Image matrix (size $N{\times}M$)
$\boldsymbol{F}$	Factors matrix (size $N{\times}P$)
$\boldsymbol{S}$	Structures matrix (size $P{\times}M$)
$\boldsymbol{\varepsilon}$	Error matrix (size $N{\times}M$)
E	Extraction fraction
E_k	Eigenvector k (length M)
λ_k	Eigenvalue k
RC	myocardial Recovery Coefficient
TBF	Total Blood Fraction
TR	Total Recovery
$TRco$	Total Recovery Image cut-off
K_1	One tissue compartment model uptake rate
k_2	One tissue compartment model washout rate
MBF	Myocardial blood flow

$\boldsymbol{X}$ – Bold variables denote matrices.

$\bar{X}$ – bars denote mean of variable X.

$\boldsymbol{X}^{\mathrm{T}}$ – Superscript T denotes matrix transpose operation.

$x_{i,j}$ – denotes the i$^{\text{th}}$ row and j$^{\text{th}}$ column element of matrix $\boldsymbol{X}$.

Chapter 1.

Introduction

Coronary artery disease (CAD) can result in reduced blood supply to regions of the heart muscle (myocardium) and is the leading cause of death in Western society. CAD can be clinically detected with relative myocardial perfusion imaging (MPI). However, uniform, reductions in blood flow due to disease in multiple large coronary arteries or diffused disease in the small arteries may not be detected with MPI. Quantitative myocardial blood flow measurements (MBF) are sensitive to uniform changes in flow and can be measured most accurately, and non-invasively, using positron emission tomography (PET). In PET a radio-active molecule, called a tracer, is injected to the patient and is imaged using a special camera. The images are then analyzed to quantify MBF.

While PET is an excellent modality for measuring MBF, it has some limitations. In order to address these limitations several image analysis techniques have been developed. This work focuses on image analysis techniques for quantifying MBF from ^{82}Rb PET images using factor analysis. A novel technique, referred to as kinetic model based factor analysis (MB) is developed and evaluated.

The objective of this work is to improve quantification of MBF. Clinically, MBF is desired as a means to detect heart disease more accurately and to guide therapy. In a research setting, quantification is desirable to accurately measure changes in MBF during disease progression and to measure response to therapy. Chapter two introduces the background knowledge and terminology and describes the goal of this work.

Chapter three describes a region-of-interest (ROI) based method for quantifying MBF from dynamic ^{82}Rb PET images. The ROIs were defined using a novel, highly-automated method designed to minimize operator variability. The operator-dependent variability of this method is evaluated and compared with other software packages. The content of this chapter has been published in Klein R., *et al.*, J. Nucl. Cardiol., 2010 (Online prepress).

Chapter four evaluates the physiological accuracy of dynamic image decomposition using constrained factor analysis. A newly proposed, minimal factor overlap (MFO) method is compared with a previously published minimal spatial (MSO) method. The limited physiological merit of both methods and the need for a physiologically accurate constraint is highlighted. The content of this chapter has been published in Klein R., *et al.*, IEEE-Med. Imag. Conf Record 2007;5(10):3268-72.

Chapter five introduces the kinetic model based factor analysis method (MB) as a physiologically accurate image decomposition method. MB and MSO are compared using

simulation and experimental data. Experimental validation of factors was achieved using simultaneous arterial blood sampling in rats and structure validation was achieved using blood pool imaging in a dog. In addition reproducibility of structures in the same dog using different imaging conditions is described. Likewise, reproducibility of MBF quantification in the same dog under varying imaging conditions is described. MB agreed better with simulation data and experimental measurements, indicating improved physiologic accuracy of the decomposed factors and structures compared with MSO. Global MBF values in the same dog and with varying tracer infusion intervals also tended to be more reproducible with MB, indicating that MB may resolve more precise MBF values. The content of this chapter has been published in Klein, R., *et al.*, Med. Phys., 2010 (In Press).

Chapter six evaluates MBF quantification using MB factor analysis. MBF values are compared to those obtained using the ROI based method described in chapter 2, and previously described spillover correction methods. Accuracy is evaluated in comparison to ^{15}O-water PET imaging as a gold-standard. While MB did not significantly improve the accuracy of MBF values, the regional uniformity of flow measurements in a healthy human population was significantly improved. This same trend was confirmed in a patient population along with the ability to resolve regional variability in flow. These results indicate that MB based MBF quantification can reduce the sensitivity to image noise and detect smaller regional MBF variations, while maintaining quantification accuracy. Some of the content of this chapter has been published in Klein, R., *et al.*, Society of Nuclear Medicine Annual Meeting Abstracts, 2010 (In Press).

The final chapter summarizes the results and discusses future work.

Parts of this work have been published in:

- Klein, R., Lortie, M.,Adler, A., Beanlands, R. S., deKemp, R. A., "*Fully Automated Software for Polar-Map Registration and Sampling from PET Images*", Nucl. Sci. Symp. & Med. Imag. Conf. Record 2006:pp 3185-88.

- Klein R., Bentourkia M., Adler A., DaSilva J., Wassenaar R., Beanlands R.S., deKemp R.A., "*Anatomical accuracy & variability in factor analysis of dynamic structures (FADS) with cardiac ^{18}FDG PET imaging.*", S. of Nucl. Med. annual meeting proceedings, 2007;48:408.

- Klein R., Bentourkia M., Beanlands R.S., Adler A., deKemp R.A., "*A Minimal Factor Overlap Method for Resolving Ambiguity in Factor Analysis of Dynamic Cardiac PET*", IEEE-Med. Imag. Conf Record 2007;5(10):3268-72.

- Lortie, M., Beanlands, R. S., Yoshinaga, K., Klein, R., DaSilva, J. N., deKemp, R. A., "*Quantification of myocardial blood flow with 82Rb dynamic PET imaging*", Eur. J. Nucl. Med. and Mol. Imaging., 2007;34(11):1765-74.

- Klein, R., Beanlands, R.S., Adler, A., deKemp, R.A., "*Model-Based Factor Analysis of Dynamic Sequences of Cardiac Positron Emission Tomography*", IEEE-Nucl. Sc. Symp. Conf. Record, October 2008;(10):5198-202

- Klein R., Katoh C., Yoshinaga K., Adler A., Beanlands R.S., deKemp R., "*Evaluation of Myocardium to Blood Pool Spillover Correction in Quantification Myocardial Blood Flow with ^{82}Rb PET*", WMIC 2009 Abstract #1159, Montreal, QC, Canada, http://www.wmicmeeting.org/

- Yoshinaga K., Klein R., Tamaki N.,"*Generator Produced Rubidium-82 Positron Emission Tomography Myocardial Perfusion Imaging – From Basic Aspects to Clinical Applications*", J. of Cardiol. 2010;55(2) 163-73.

- Klein R., Renaud J. M., Ziadi M. C., Thorn S. L., Adler A., Beanlands R. S., deKemp R. A., "*Intra- and inter-operator repeatability of myocardial blood flow and myocardial flow reserve measurements using Rubdium-82 PET and a highly automated analysis program*", J. Nucl. Cardiol., 2010 (online prepress)

- Klein, R., Beanlands, R. S., Wassenaar, R. W., Thorn, S., Lamoureux, M., DaSilva, J. N., Adler, A., deKemp, R. A., "Kinetic m*odel based factor analysis of dynamic sequences for 82-rubidium cardiac positron emission tomography*", Med. Phys., (in press).

- Klein, R., Beanlands, R. S., Wassenaar, R. W., Thorn, S., Lamoureux, M., DaSilva, J. N., Adler, A., deKemp, R. A., "Model Based Factor Analysis of Dynamic Sequences of Cardiac Positron Emission Tomography", Med. Phys. (in press).

- Klein, R., Yoshinaga, K., Katoh, C., Adler, A., Beanlands, R., Tamaki, N., deKemp R., "*Improved homogeneity of normal MBF using factor analysis with 82Rb PET*", S. Nucl. Med. Annual Meeting Abstracts #1327, 2010 (in press).

- Ziadi M. C., deKemp R. A., Williams K., Guo A., Renaud J. M., Tee R. E., Klein R., Chow B., Ruddy T. D., D'Mello N., Aung M., Garrard L., Beanlands R. S. B., "*Clinical Characterization of Patients with Preserved and Reduced Myocardial Flow Reserve Measured using Rubidium-82 Positron Emission Tomography*", J. Nucl. Med. (under review).

Chapter 2.

Background

Coronary artery disease (CAD) is the leading cause of death worldwide [1,2,3]. The economic burden in the US alone in 2006 was estimated to be $400 billion [4]. Early detection of disease can lead to more effective intervention and is therefore vital to improving patient outcome. Quantification of myocardial blood flow with positron emission tomography may detect CAD at its earliest stages and help guide therapy [5,6,7].

The heart is primarily composed of muscle tissue (myocardium) that contracts and dilates in a manner that pumps blood through the entire body via a circulatory system as demonstrated in Figure 2-1. The veins aggregate the blood in the body and deliver it to the right atrium and then on to the right ventricle (RV) of the heart, where a contraction of the heart pushes the blood through the lungs. In the lungs CO_2 is extracted and the blood is oxygenated. The blood is then returned to the left atrium of the heart and onto the left ventricle (LV) where a contraction returns the blood to the body through arteries, thus completing the cycle.
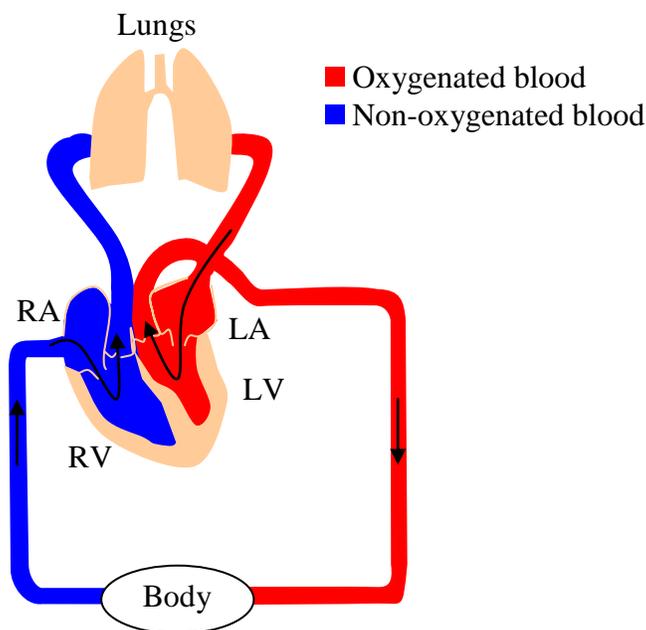
Figure 2-1 – Circulatory system diagram showing the four chambers of the heart, lungs and body. Oxygenated blood from the lungs is pumped through the left atrium and ventricle to the body (and the heart muscle) through arteries. The non-oxygenated blood is returned by the veins to the right atrium and ventricle to be pumped back to the lungs for oxygenation.

Immediately at the output of the LV into the main artery (aortic root), the left and right coronary arteries branch off to feed blood to the heart itself. In the event that these arteries (or their distal branches) become narrowed (stenosis), blood supply to dependent regions of the heart is restricted or altogether stopped (occlusion). The tissue downstream from the stenosis can become deprived of oxygen (ischemia) which is necessary for cell

survival and function. When the heart is exercised (stressed) the demand for oxygen increases, and ischemia can worsen. Acutely, coronary artery occlusion can result in a heart attack and death. Chronically, stenosis can lead to reduced heart function, muscle damage, and eventually scarring. While therapies exist to restore blood flow, they can only benefit patients that are diagnosed sufficiently early and are treated successfully.

In the heart myocardium, the arteries branch off into smaller and smaller arteries in a fractal manner [8] until they become capillaries. The capillaries receive oxygen-rich blood from the arteries, exchange oxygen, nutrients, CO_2, and waste with the surrounding tissue, and deliver the waste-rich blood to the veins [9]. The small arteries, capillaries, and veins (<100 μm in diameter) are sometimes referred to as the micro-vasculature. Widespread (diffused) disease of the micro-vasculature can affect the supply of blood to the myocardium [9].

Myocardial blood flow (MBF) quantifies the rate at which blood perfuses the myocardial tissue and is usually measured in units of mL/min/g, read as mL/min of blood per g of tissue. MBF measurement, therefore, is an increasingly important screening, diagnostic, and prognostic tool [10,11,12], as it enables detection of disease at its earliest stage [7,13,14]. Clinically, an accurate means of measuring MBF is crucial for early detection of disease and tracking its development during therapy. In research settings, accuracy is critical for understanding disease progression, and evaluating the efficacy of new therapies. MBF can be most accurately measured *in vivo* using dynamic positron emission tomography and suitable tracer kinetic models.

2.1 Cardiac Positron Emission Tomography

With the ability to image the physiological distribution of specific molecules within the body in a relatively non-invasive manner, nuclear medicine imaging has become a leading diagnostic tool, including for measurement of MBF [15]. A compound labelled with a radioactive isotope is introduced to the patient, usually by intravenous injection, and its location in the body is later imaged using a scanner sensitive to the emitted radiation. The compounds, referred to as radio-labelled tracers, are designed to interact within the patient so that they aggregate in a region of interest by participating in a biochemical process of interest. The compounds are introduced in trace amounts so that they do not have a significant effect on the physiology of the subject and are therefore commonly referred to as tracers. Over time, the radioactive label in the tracer decays, resulting in emission of radiation. The emitted radiation is proportional to the concentration of the labelled molecule.

Given a closed system containing radioactive material, an exponential decrease of activity is observed as time progresses [16]. The rate of decay is a characteristic property of the radioactive isotope, and is measured as a statistical average of the elapsed time until half the original activity remains. This measure is referred to as one half-life, $T_{1/2}$, and can vary from split seconds to many millennia depending on the isotope. In molecular imaging, one

would like an isotope that lasts long enough to perform the measurement, but short enough to minimize exposure to the patient. A short half-life also carries the benefit of reducing the time between repeated scans of the same subject. Typical imaging applications use isotopes with a half-life ranging from several seconds to several hours.

When imaging the patient, regions containing high tracer concentration radiate strongly, contrasting with the surroundings. A scanner that measures the radiation from the patient can reconstruct tomographic images through the field of view. The concentration of activity is dependent on the interaction of the tracer within the body and is therefore indicative of a corresponding biochemical and physiological **function** within the body, in contrast to **anatomical** images produced by modalities such as conventional x-ray computed tomography (CT) and magnetic resonance imaging (MRI).

Positron Emission Tomography (PET) is the leading nuclear imaging modality in terms of precision, ability to make quantitative radiation concentration measurements, and minimizing the patient's radiation dose [17]. The radioactive label is an isotope that decays by positron emission. In the nucleus, a proton is converted into a neutron and excess positive charge is ejected in the form of a positron (positively charged electron). The positron travels a few mm through the surrounding medium and eventually interacts with an electron resulting in a mutual annihilation. The combined mass of the electron and positron is converted into two equal energy (511keV) collinear photons as shown in Figure 2-2-left. These high energy photons travel through the body and can be detected by dense scintillating crystals coupled to photomultiplier tubes.
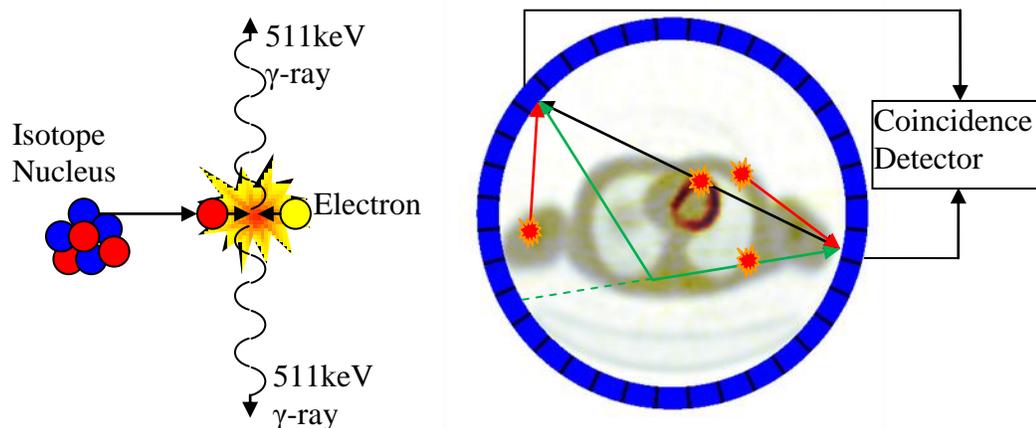
Figure 2-2 – Positron emission tomography. The positron discharge followed by annihilation with an electron producing two collinear photons (γ-rays) on the left. The projected line of response based on a detection of coincident events by the scanner is shown on the right. The image is a cross-section of the chest with red depicting tracer uptake in the heart muscle. A transmission image is fused in gray, showing the lungs and arms for anatomical reference.

A typical PET scanner consists of planar rings of detectors containing hundreds of detectors. Since the two photons formed during a decay are created at the same time and travel in opposite directions at the speed of light, their detection is expected to occur almost

simultaneously (i.e. in coincidence) by detectors on opposite sides of the event (black arrows Figure 2-2-right). If two coincident photons are detected by the scanner it is assumed that the decay event occurred along the line of response (LOR) connecting the two detectors. Coincident detections can be processed through various mathematical algorithms, such as filtered back projection or iterative algorithms, to reconstruct tomographic images (a volume made up of slices) of the scanner field of view (FOV).

The quality of the image is degraded by scattered and random events which are detected by the camera and cannot be discerned from unscattered coincident events. Scatter results from interaction of a photon with the medium it is travelling through, resulting in a change of the photon's direction of travel (green arrows in Figure 2-2-right). In this case, the LOR connecting the coincident detectors does not traverse the location of the decay event. Random events result from two separate decay events which occur almost simultaneously and one photon from each (red arrows in Figure 2-2-right) is detected by the camera. The reconstruction algorithm treats these events as a single decay along the LOR connecting the detectors (along the same LOR shown with black arrows in Figure 2-2-right). Scatter and random events may result in a biasing (background offset), noise, and reduced resolution [16]. While scatter correction and randoms rejection and correction techniques are continuously being improved, the accuracy of PET is still limited by these events.
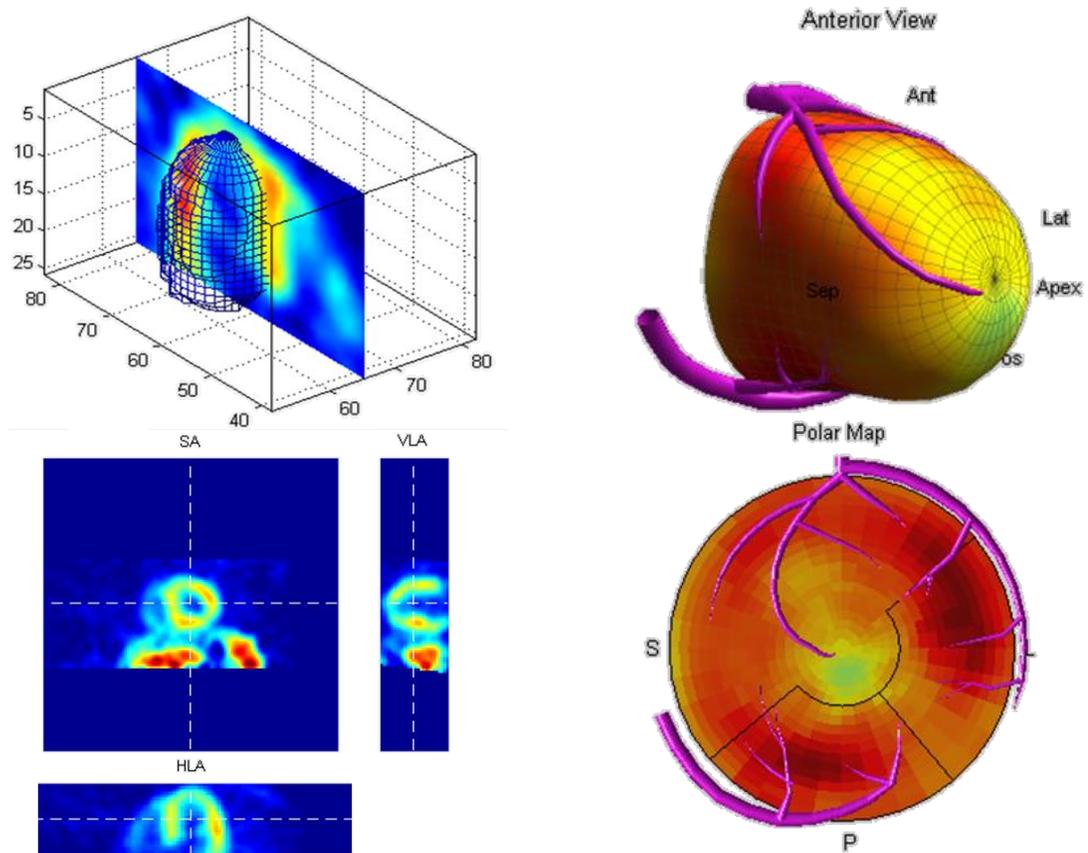
Figure 2-3 – Various views of pet image volumes after reorientation to the LV reference frame.

The reconstructed PET image volumes can be viewed using specialized software that renders slices through the FOV (Figure 2-3 top left). Image units can be in activity concentration (Bq/cc) or raw counts, but for viewing purposes, images are often normalized to peak image intensity. In cardiac applications, the image is typically reoriented to the heart reference frame to generate short axis (SA), vertical long-axis (VLA), and horizontal long-axis (HLA) slices through the LV (Figure 2-3 bottom left). The image may be registered to a mesh (top right) for viewing of the LV surface. The LV surface is often viewed in polar-map form (bottom-right) which presents the entire LV surface in one image (without visual occlusion). Synthetic artery structures (purple) can be superimposed to the LV mesh and polar-map.

All PET tracers must be labelled with a positron-emitting isotope. A major advantage of PET over other molecular imaging modalities is that oxygen, carbon, and nitrogen, which are common building blocks in organic chemistry, have positron-emitting isotopes with practical half-lives (Table 2-1). These isotopes give the potential to synthesize almost any organic compound as a PET tracer.

TABLE 2-1 – COMMONLY USED POSITRON-EMITTING ISOTOPES [18]

Isotope		Half Life ($T_{1/2}$) [min]	Mean distance to annihilation in water [mm]
Cyclotron Produced	[15]O (oxygen-15)	2.1	1.1
	[13]N (nitrogen-13)	10.0	0.72
	[11]C (carbon-11)	20.3	0.56
	[18]F (fluorine-18)	110	0.35
	[68]Ga (gallium-62)	67.8	1.1
Generator Produced	[82]Rb (rubidium-82)	1.27	2.4

Various tracers have been developed to image different organs, tissue, and functions. Increased glucose consumption, for example, is used for detection of cancerous tumours [19,20,21] and distinguishing between hibernating (live) and necrotic (dead) tissue in the heart [22,23,24] using ^{18}F-Fluorodeoxyglucose (FDG). In neuroscience FDG has been used to locate hypoactive and hyperactive regions in the brain to diagnose disease such as epilepsy and schizophrenia [18,25]. Another application used PET imaging to assess the integrity of the blood brain barrier [26] using [82]Rb as a tracer. The list of applications goes on and is continuously growing.

Although FDG scans for detection of tumours are by far the most common application of PET today, potential applications are only limited by the available tracers and image analysis techniques. As research into these fields progresses PET promises powerful new tools both for research and clinical applications. One of the most actively sought applications is accurate, efficient, and cheap measurement of MBF.

2.1.1   MBF Tracers

Currently ^{15}O-water (water that is labelled with an 15-oxygen radionuclide) PET is considered to be the most accurate method for measuring MBF non-invasively [7]. Water is injected into the blood stream and diffuses freely across capillary and cell membranes and is therefore distributed to the body organs in proportion to the flow of blood. ^{15}O-water is manufactured using an onsite cyclotron and must be administered immediately to the patient due to its short half-life (2.1 min) requiring specialized delivery and infusion equipment. Good coordination between the cyclotron lab, imaging technologists, and nursing staff is critical to successful water exams. Consequently, water imaging studies are prohibitively expensive for routine use and alternative tracers are being sought.

Ammonia is taken up by cells from the blood stream through a variety of active transporters as well as passive diffusion. The cyclotron produced 13-nitrogen is synthesized to produce $^{13}NH_3$. The 10 minute half-life of ^{13}N makes administration of the tracer much simpler than water; however, the need for an onsite cyclotron and radiochemistry lab remains. ^{13}N-ammonia is seen as a practical alternative to ^{15}O-water with similar accuracy for perfusion imaging [7].

Rubidium (and its positron emitting isotope [82]Rb) is a cation that is bio-chemically similar (analogous) to potassium [6,7,27]. Potassium is extracted by all living cells through ionic pumps that are present in the cell membrane [28]. Potassium analogues are taken up by the heart muscle cells at a rate that is dependent on blood flow [29,30]. After injection of [82]Rb into the blood stream activity concentration in the myocardium increases, while activity concentration in the blood decreases over time. Several minutes after injection, PET images show retained activity in the heart contrasting with the low activity of the blood (as demonstrated in tomographic images in Figure 2-4).

Normal Perfusion   **Abnormal Perfusion**
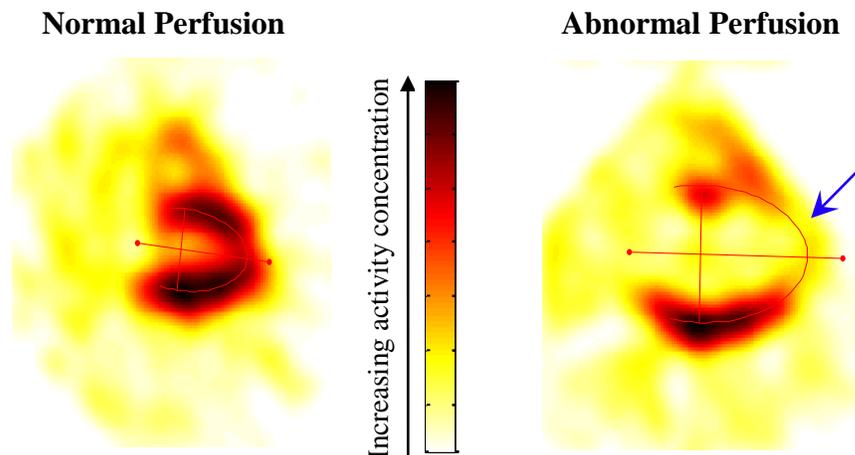
Figure 2-4 – Sample horizontal-long-axis images though the heart in [82]Rb PET uptake images used to measure perfusion in the myocardium. A normal heart is shown on the left depicting the elliptic shape characteristic of a long axis cross section. The image on the right reveals reduced blood flow to the septal wall and apex of the left ventricle (blue arrows), shown by a relatively lower concentration of activity. Also, the larger heart may be indicative of heart failure.

[82]Sr/[82]Rb generators have been developed as an alternative to cyclotron produced tracers. The generators are loaded with [82]Sr and can be used for 4-8 weeks as a constant source of [82]Rb [31]. With sufficient patient throughput, [82]Rb, can be very cost effective [32,33,34] (as much as 10 times cheaper than water/ammonia). In addition, the generators enable centres without a cyclotron to provide PET perfusion imaging services that would not be possible otherwise. During the life of the generator, [82]Rb may be infused as frequently as every ten minutes, enabling fast serial imaging and high patient throughput.

A dedicated infuser is required to flush [82]Rb activity from the generator and administer it to the patient. In [35] a custom [82]Rb infuser to deliver a reproducible infusion profile regardless of the age of the generator is described, which may improve the reproducibility of MBF quantification [35,36]. The infuser also flushes the injection line automatically at the end of the infusion to remove activity outside the scanner field of view, which is important with the industry's transition from 2D to 3D PET instrumentation [37,38].

The shortcoming of using [82]Rb is that its longer positron range (as listed in Table 2-1) results in lower resolution images. In addition, [82]Rb decay discharges a 777KeV prompt photon with ~15% of the positron discharges, which may be detected in coincidence with an annihilation photon. The accumulation of these events leads to a nearly uniform background in the image which must be estimated and subtracted [16]. Finally, the extraction of [82]Rb is dependent on flow and must be corrected for as part of the quantification process [39]. The benefits of [82]Rb when compared to alternative perfusion agents outweigh these challenges. In the past five years [82]Rb has seen exponential growth in the US market as well as increasing interest in Europe and Japan [40]. As [82]Rb PET becomes routine in clinics, the demand for accurate diagnostics based on quantified cardiac blood flow has grown.

2.2 Myocardial Perfusion Image Interpretation

Relative myocardial perfusion imaging (MPI), after tracer uptake by the heart, is a well-established technique for the diagnosis and prognosis of CAD. Static uptake images are interpreted by physicians that evaluate the uniformity in tracer uptake between different regions of the heart under rest and stress conditions. A region with maximal uptake is assumed to be normally perfused, and regions with significantly reduced uptake are interpreted as abnormally perfused. Arteries associated with regions having reduced uptake at stress and normal uptake at rest are assumed to be narrowed (stenosis), as demonstrated in Figure 2-5. Arteries associated with regions having reduced uptake at rest and stresses are assumed to be completely occluded. Arteries associated with region having normal uptake at rest and stress are assumed healthy.

Rest MPI   **Stress MPI**
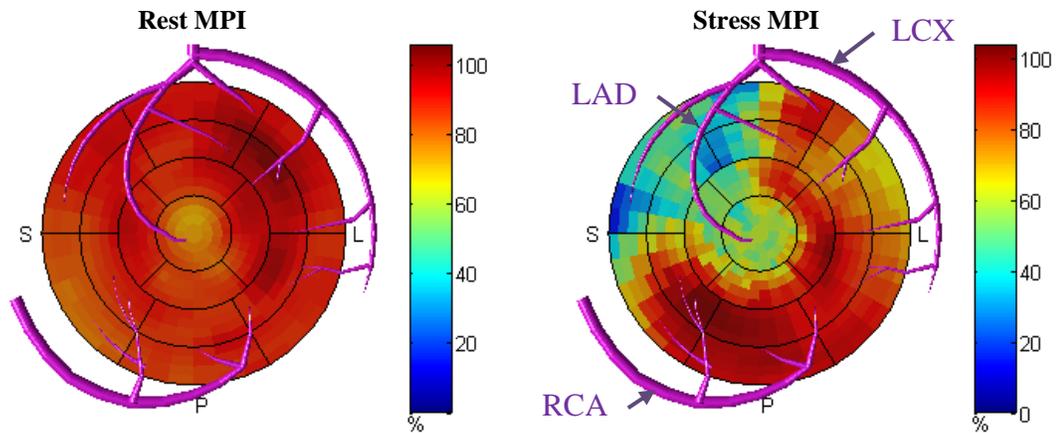
Figure 2-5 – Relative MPI (Uptake) at rest (right) and stress (left) demonstrating partial stenosis of the LAD artery. The arteries are demonstrative of typical anatomy.

False interpretation is common in cases where all regions of the heart exhibit reduced uptake [41]. This is particularly common in cases of multi-vessel disease [42], abnormal micro-vasculature function, and diabetes [43]. As a consequence, some of the most severe cases may go undetected or their severity may be underestimated [44].

2.3 Dynamic PET Imaging

Absolute myocardial blood flow (MBF), as opposed to relative MPI, quantifies the rate of blood supply to tissue in units of mL/min/g (millilitres of blood per minute per gram of tissue). MBF can indicate whether the most highly perfused regions in the image are indeed normal as demonstrated in Figure 2-6. In normal patients rest MBF values are expected to be approximately 0.7-1.0 mL/min/g while at stress MBF values greater than approximately 2.5 mL/min/g are considered normal (demonstrated in Figure 2-6 left). In the presence of disease stress MBF may decrease below 2.0 mL/min/g (demonstrated in Figure 2-6 right). In severe disease rest MBF may also be reduced.

In order to quantify MBF, the rate at which the tracer is extracted from the blood and accumulated in the tissue is measured. To do so, a series of PET images are created sequentially from time of tracer injection until uptake is achieved.

Dynamic image sequences are designed to have a minimal number of time frames to reduce image reconstruction time, to have sufficient temporal resolution to sample the tracer kinetics, and to accumulate enough photons to reconstruct good quality images. Typically, early time frames are short (2-20 s) and capture the fast redistribution of the tracer, and late time frames are longer (1-10 min) to reduce the image reconstruction time and accumulate sufficient coincidences when the tracer has decayed and dispersed in the patient's body.

The administration of the tracer must also be optimized so that enough activity is present in the late time frames to support good image quality. However, one must not introduce so much activity so as to saturate the camera. While MPI tracer injections are commonly performed with a fast bolus, dynamic image infusions are often performed over a

longer duration (10-30 s). With the generator produced ^{82}Rb tracer, a specialized infuser is required to administer the tracer at a constant rate over a predefined infusion interval [35].
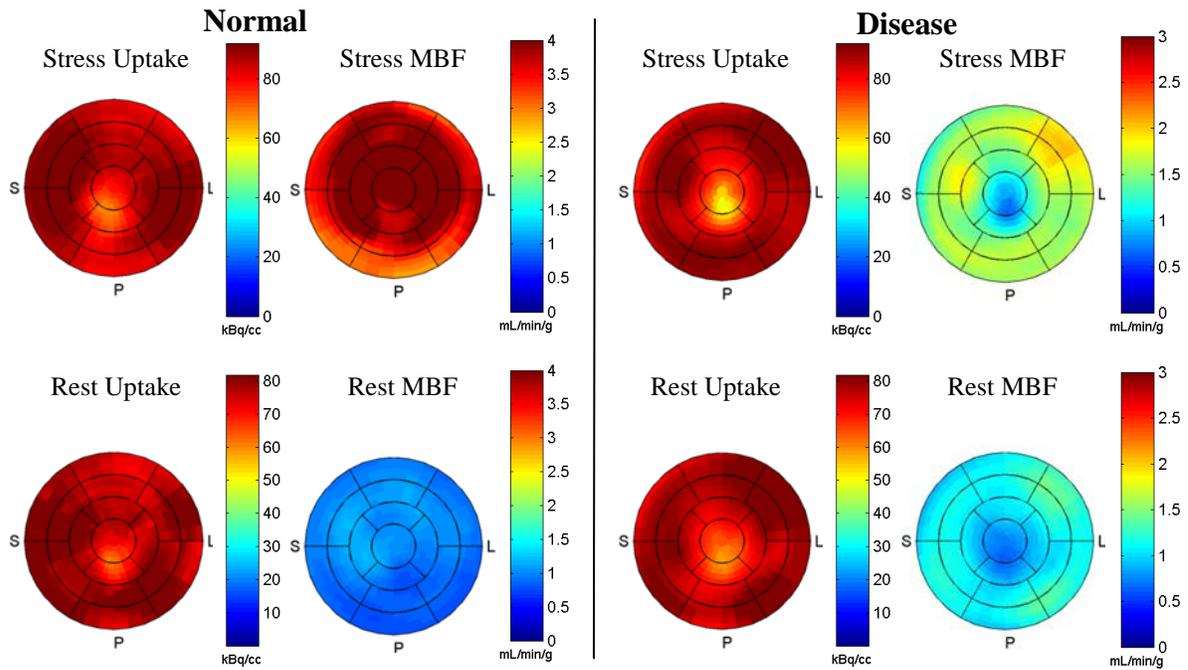
Figure 2-6 – Relative MPI uptake and absolute MBF in two patients with uniform uptake. In the normal patient (left), MBF is normal at rest and stress, while in the diseased patient (right) MBF is uniformly low at stress.
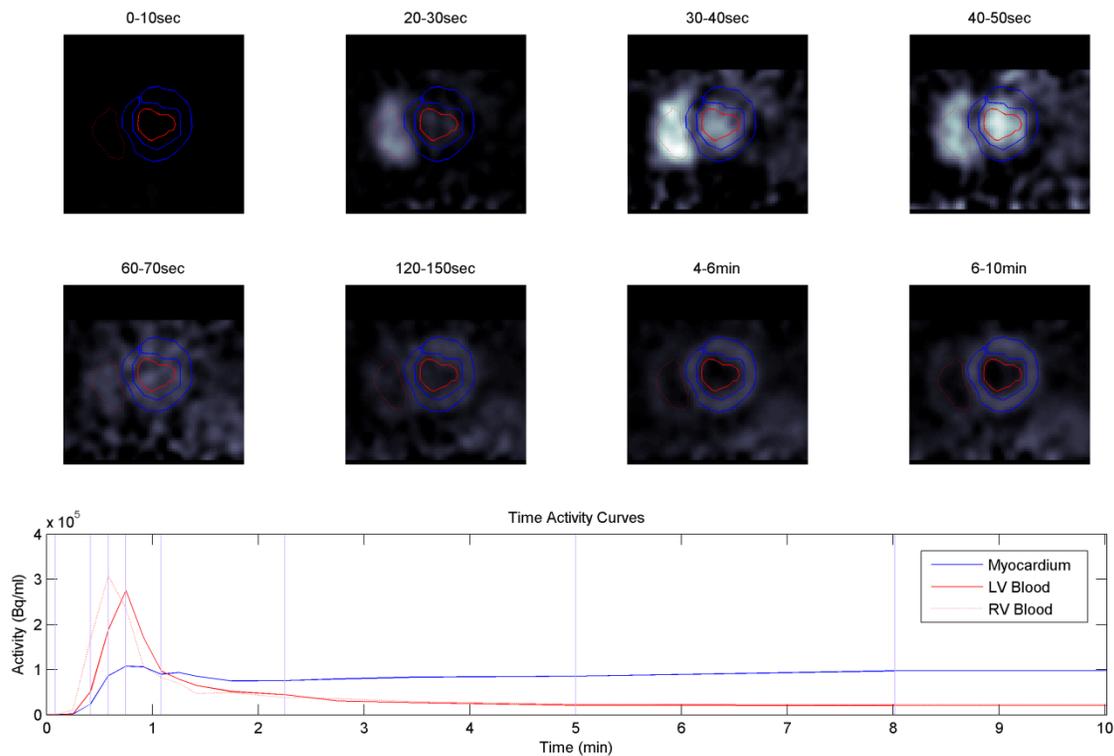
Figure 2-7 – Regions of interest in a dynamic image sequence and their corresponding time-activity-curves (TACs) shown below.

Time-activity-curves (TACs) can be generated by defining regions-of-interest (ROIs) and sampling the image over all time frames. An arterial blood input function is created by sampling a region in the image with high blood concentration and minimal contribution from other organs. Typically the left ventricle blood pool ROI is used [45], as demonstrated by the solid red curve in Figure 2-7. Since the LV blood pool is immediately upstream from the coronary arteries, it can be regarded as an arterial blood TAC, $C_a(t)$. Similarly, sampling of the myocardium region over the image sequence generates a myocardial TAC, $C_m(t)$. To assess regional variability, the myocardium ROI can also be segmented into several smaller ROIs [46,47].

A kinetic model relating arterial blood and myocardium activities can be assumed to describe the physiology with respect to the tracer molecule. The parameters of the kinetic model are obtained by minimizing the error between the measured and modeled myocardium TACs. Kinetic modeling may be equated to measuring system parameters by enforcing an input function (arterial blood TAC) and recording the system generated output function (myocardium TAC).

The complexity of models varies based on the biochemical interaction of the tracer *in vivo* and the physical effects that are accounted for. However, the number of free parameters in a model is limited by the quality of the data, often requiring the use of simplified models [48,49]. Kinetic modelling results are validated for accuracy using a physiologic standard. In addition test-retest reproducibility is an important characteristic of the quantification method. While kinetic modeling is versatile and can be adapted to many tracers and physiologic functions of interest, this work focuses on quantification of MBF using [82]Rb PET.

2.4 MBF Quantification

The kinetics of rubidium have been described using a two-compartment model consisting of blood, interstitial compartment, and tissue compartments [50,51]. However simplifications of the model have been favoured due to the complexity of the two compartment model compared to the quality of the data and also since the transfer of tracer from blood to tissue is of primary interest for quantification of MBF.

The transfer of Rb from blood to myocardium tissue may be described by a model consisting of a compartment that is perfused by a flow of blood and an uptake rate, K_1, describing the transfer of Rb into the compartment, as shown in Figure 2-8. An additional rate constant, k_2, models the washout of Rb from the tissue compartment. The change in Rb concentrations in the compartment can be expressed using the following differential equation [39,52]:

$$\frac{dC_t(t)}{dt} = \rho K_1 C_a(t) - k_2 C_t(t)$$

<div align="right">2-1</div>
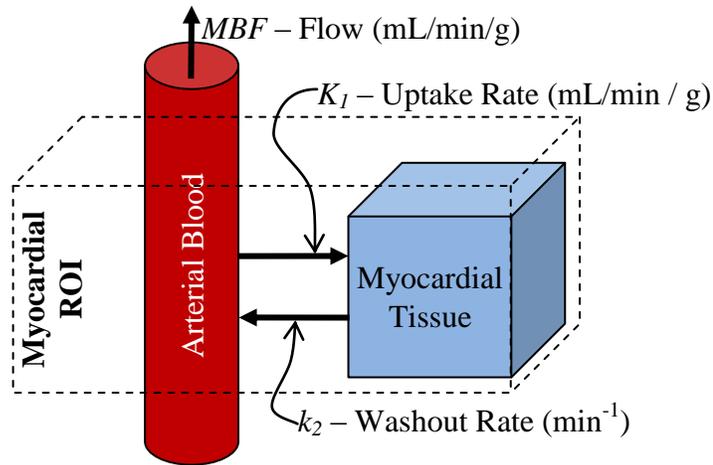
Figure 2-8 – One compartment model for MBF quantification using ^{82}Rb depicting that a voxel in the myocardium region of interest is composed of blood and a myocardium compartment. Tracer is taken up at rate K_1 and is washed back out to the blood at rate k_2.

The uptake rate, K_1, is measured in units of mL/min/g, read as mL/min of blood per g of tissue. The washout rate, k_2, is measured in units of min^{-1}. The density of myocardial tissue, ρ=1.04g/mL, must be included for units to agree. The same equation may be expressed using the convolution operation (equation 2-2) where $C_t(t)$ [Bq/g] and $C_a(t)$ [Bq/mL] are the respective tracer concentrations in the myocardial tissue and blood at time t. The convolution kernel ($m(t)$) is expressed as an exponent as in equation 2-3.

$$C_t(t) = C_a(t) \otimes m(t) \tag{2-2}$$

$$m(t) = \rho K_1 e^{-k_2 t} \tag{2-3}$$

A region of interest overlapping the myocardium contains signal from the myocardial tissue as well as from arterial blood perfusing the tissue. Due to the limited resolution of PET, additional blood signal may "spillover" into the myocardium region increasing the proportion of blood in the ROI. Therefore, the corresponding myocardial TAC, $C_m(t)$, may be modelled as a linear combination of myocardial tissue and arterial blood signals ($C_t(t)$ and $C_a(t)$ respectively) as demonstrated in Figure 2-8. The respective scalars P_t and P_a account for the fraction ($0 \leq P \leq 1$) of the ROI volume that can be attributed to either signal as in equation 2-4. P_t may also be referred to as the tissue recovery coefficient (RC). The recovery parameter P_a may also be referred to as the total blood fraction (TBF) which accounts for the combined contributions of signals from the tissue-blood volume and spillover from the blood in the adjacent LV cavity.

$$\begin{aligned}C_m(t) &= P_a C_a(t) + P_t C_t(t) \\ &= TBF \cdot C_a(t) + RC \cdot C_t(t)\end{aligned} \tag{2-4}$$

By substitution of 2-2 and 2-3 for $C_t(t)$ the following form may be obtained.

$$C_m(t) = TBF \cdot C_a(t) + \{RC \cdot K_1\} \cdot \rho \cdot C_a(t) \otimes e^{-k_2 t} \qquad \textbf{2-5}$$

The impracticality of this approach becomes evident as the product contained in the curly brackets, which quantifies the myocardial signal, cannot be resolved into RC and K_1 without additional information or assumptions. The literature contains several methods for estimating RC including selection of calibrated values [42,53] and automatic estimation [54,55]. More commonly, it is assumed that the signal in the myocardial ROI is entirely composed of blood and myocardium signals, thus RC can be substituted by 1-TBF [56] giving

$$C_m(t) = TBF \cdot C_a(t) + (1 - TBF)C_t(t) \qquad \textbf{2-6}$$

This algebra would not be beneficial for quantifying flow, MBF, if it were not for a relationship with the uptake rate, K_1. The relationship is through an extraction fraction that represents the micro-anatomy and the cell physiology with regards to the tracer. The extraction fraction refers to the ratio of the tracer in the blood that participates in the extraction process.

The two primary means of tracer transport from blood into the compartment (tissue) are through diffusion and extraction [7]. Water has ideal properties as it diffuses freely, meaning that K_1 directly represents flow and needs no extraction correction. ^{82}Rb, ^{13}NH$_3$ (Ammonia), ^{62}Cu-PTSM, and ^{99m}Tc-sestamibi are extracted from blood through diffusion and active transport, thus their extraction fractions decrease as the flow increases [29,30,39]. The Renkin-Crone model [29,30] shown in equation 2-7 can be used to compute K_1 from MBF. The inverse is achieved by iteratively solving for MBF for a given K_1 value.

$$K_1 = \left(1 - a \cdot e^{-b/MBF}\right)MBF \qquad \textbf{2-7}$$

Some previously published extraction parameters are shown in Table 2-2 along with a plot of their modeled response in Figure 2-9. Extraction functions are either determined experimentally [57] or more commonly calibrated based on known flow properties of a given population [39,55]. Population derived extraction function parameters can also serve as a calibration that compensate for biases introduced during the image acquisition and analysis processes. Variations in reported a and b values may be attributed to different sample populations as well as variations in scanning protocol, image reconstruction, ROI definitions, tracer kinetic model, and the quantification process.

MBF values may be reported either globally or regionally. Global values may be used to characterize the overall health of the subject, while regional MBF may provide additional information on the distribution of the disease. Regional quantification may be used to discriminate between disease affecting a particular vessel and a homogenous reduction in blood flow.

TABLE 2-2 – REPORTED RENKIN-CRONE MODEL EXTRACTION FRACTION PARAMETERS

Tracer	Citation	a	b
$H_2{}^{15}O$	[5,7,58]	0	0
$^{13}NH_3$	Schelbert 1981 [59]	0.096	1.083
^{62}Cu-PTSM	Beanlands 1992 [60]	0.89	0.45
^{82}Rb	Lortie 2007 [39]	0.77	0.63
	Katoh 2008 [55]	0.86	0.54
	Schelber 2004 [61,62]	0.73	0.593
	Yoshida 1996 [41]	0.85	0.45
^{99m}Tc-Sestamibi	Phelps 2004 [62]	0.77	0.45
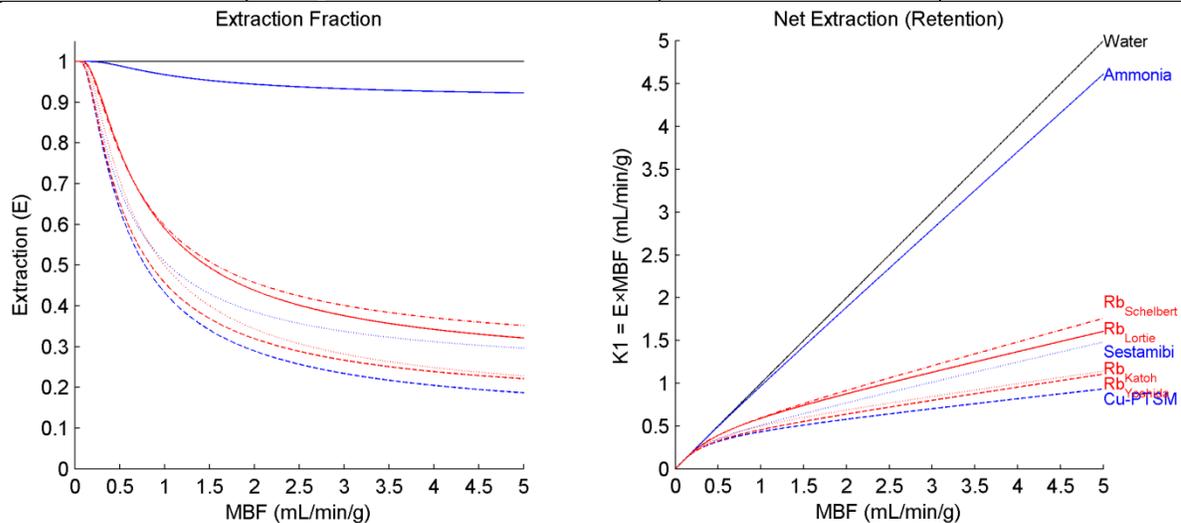
Figure 2-9 – Extraction fractions in relationship to *MBF* values.

2.4.1   Myocardial Flow Reserve

The capacity of the heart to increase blood flow with physical load is referred to as myocardial flow reserve (MFR) and is defined as the ratio of flow between state of peak stress and state of rest. To measure MFR the imaging protocol includes a baseline scan at rest and after induced stress. While stress can be achieved through physical exercise (using treadmill or resistance pedaling) [63], it is more practical to use drugs (some of which are listed in Table 2-3) while the patient is positioned in the PET camera [7,38].

Assessment of absolute MBF and MFR (the ratio of stress to rest MBF) using dynamic PET may represent a more sensitive tool to detect multi-vessel disease [44,41,42,64,65] as well as pre-symptomatic CAD [7,13,14]. Others have proposed that the difference between MBF at stress and rest may be more suitable for detection of CAD [42,66]. Assessment of MFR using PET has also been shown to yield prognostic value for the prediction of adverse patient outcomes [10,12,67,68].The principal use of quantitative analysis has been limited mainly to research applications [69], but recent advances in PET instrumentation [70] and tracer availability may facilitate the routine application of flow

quantification in clinical practice. Various software packages have been developed to process dynamic image sequences and to quantify MBF [39,71,72,73].

TABLE 2-3 – COMMON CARDIAC STRESSING DRUGS

Chemical name	Generic Name	Cardiac stressing mechanism
Dobutamine	-	Stimulation of sympathetic nervous system
Persantine	Dipyridamole	Vasodilation
Adenosine	-	Vasodilation

2.5 Validation of MBF

The accuracy of MBF and MFR quantification with PET has been validated *in vivo* using microspheres [44,57,67,74,75,76,77,78] or other invasive measurements [41,79]. As their name implies, microspheres are microscopic spheres that are radio-active (or fluorescent). They are administered into the arterial blood stream using a surgically installed catheter to the LA. The microspheres become lodged in the small capillaries of downstream myocardial tissue in proportion to MBF. After sacrificing the animal, the heart is excised and segmented. Each segment is weighed, and the microspheres are counted based on the radioactivity of the segment. MBF is calibrated to microspheres counted in a blood sample from a distal artery that was withdrawn at a fixed and known flow rate simultaneously with the microsphere injection. These experiments are limited to animal studies and at a single session. Microsphere blood flow measurements can be unreliable without skilled staff and if too few microspheres are aggregated in the target organ and/or reference samples [74]. Variability in blood flow measurements with injection site and location of reference samples has been demonstrated [74].

Doppler ultrasound [79] or electromagnetic flow meters [41] using a catheter that is inserted into an artery permit direct blood flow measurement, but is limited to the major arteries (which are sufficiently large for the probe), and therefore gives little insight into regional blood flow (only large territory estimates). In addition, the probes are not compatible with small animal experiments and are invasive [80], limiting their use in humans.

In humans, accuracy has been measured through agreement of MBF using different PET tracers, of which ^{15}O-water PET is considered to be the most accurate [39,72,81,82]. However, MBF quantification processes with different tracers may have commonalities that could introduce similar biases, limiting the ability to measure accuracy with regards to the physiology.

Inverse correlation between MBF and lesion sizes measured using x-ray angiography or CT-angiography have also been reported [83]. However, angiography pertains to the large coronary arteries and not the micro-vasculature. Furthermore there is evidence that angiography is complimentary to PET, not equivalent [15].

High precision is important for detection of serial changes during disease progression or therapy [66,84] and is evaluated through test-retest reproducibility [58,63,81,76,82,85,86,87,88], of which operator-dependent variability [53,71,72,85,89,90] is an important factor [91]. Test-retest repeatability is assessed by repeating the imaging and quantification on close and separate occasions [38,53]. The quality of the MBF measurement is judged by the reproducibility of the measurements. Thus the more reproducible a method is, the more sensitive it is to detecting small changes due to progression of disease, efficacy of therapy, or differences in populations.

Classification performance of competing methods can be compared in an experiment consisting of two (or more) populations, such as normal/diseased [83] or normal/risk-factor [13]. In this context, sensitivity refers to the proportion of cases that are correctly classified as first population (true-positive) while specificity refers to the proportion of cases that are correctly classified as second population (true-negative). Thus a trade-off usually exists between improving sensitivity or specificity as visualized by receiver operating characteristic (ROC) curve analysis, but together they indicate the classification accuracy. Sensitivity and specificity, even if not related directly to physiology, are important characteristics of the application as they quantify the ability to discriminate between healthy and diseased MBF.

2.6 The Effect of Image Resolution on MBF Quantification

The accuracy of kinetic model analysis is often limited by the lack of pure arterial blood and myocardium signals [54], which results from the finite resolution of PET, cardiac/respiratory motion, and uncorrected scatter. Signal mixing, also referred to as spillover, results in arterial blood input functions that are biased by activity from the myocardium and myocardium functions that include more blood signal than is explained by the anatomy. In addition, signals from other organs that are adjacent to the heart may spillover into the myocardium and/or blood regions, further degrading the accuracy of the measured signal. Both scatter correction and the resolution of PET are continuously being improved. However, spatial resolution is inherently limited by the positron range, and scatter correction may never be perfect.

The shortcomings of ROI based methods have prompted development of alternative ways to determine image based TACs for tracer kinetic modelling, in addition to methods of correcting for recovery losses that affect the scaling of the output signal [92]. This section discusses some of these methods in the context of [82]Rb MBF quantification. A more precise explanation of the effects of image resolution on the MBF quantification process follows.

The resolution of cardiac PET is limited by an accumulation of blurring effects. The blurring effect is often estimated as a three-dimensional Gaussian response function characterized by the full-width-at-half-maximum (FWHM) [93]. FWHM is defined as twice the distance between the centre of the response function and the point where the response is

half of the maximum. Assuming that all blurring effects have a Gaussian spatial distribution, the final image resolution can be expressed as:

$$FWHM_{image} = \sqrt{FWHM_{effect\ 1}^{2} + FWHM_{effect\ 2}^{2} + \cdots}$$ **2-8**

In cardiac PET some blurring effects include:

1. Radiation physics – Positron range, photon scatter, photon noncollinearity, and prompt coincidences are all physical effects that contribute to blurring the image. While scatter and randoms corrections do help, the range that the positron travels from its ejection during nuclear decay until its annihilation is currently seen as a fundamental limit of PET resolution.

2. Motion – Cardiac contractile and respiratory motion cannot be avoided as their periods are orders of magnitude shorter than the image acquisition times. Furthermore motion in some pixels and not others means that the blur is spatially variant. Cardiac and respiratory gated images with specialized reconstruction algorithms have been sought as a means to overcome motion blur [94,95].

3. Scanner design – the intrinsic resolution of the scanner is limited by the size of detectors and their photon stopping power [18]. In addition, limited temporal resolution of the crystals and electronics limit the size of coincidence windows which could help reject random events. Limited energy resolution also limits the ability to reject scattered photons [16].

4. Image reconstruction and image processing - Inherent and explicit smoothing are built into most reconstruction and image processing algorithms in order to accelerate computation, ensure convergence, and reduce noise [96].

Image resolution typically refers to the combined effects of scanner intrinsic resolution, image reconstruction, and radiation physics. While the image resolution in practice is rarely uniform throughout the image, in the small region of the heart (which is nearly centred in the camera field of view) the image resolution is typically assumed uniform if the effects of motion are neglected.

Intuitively, one may attempt to remove the image blur using image sharpening techniques. Extensive research has been done into image sharpening, but this ill-posed problem often results in unsatisfactory results as noise is often amplified [97]. Non-uniform image resolution, as in cardiac PET [98], further complicates image sharpening, thus this approach has had limited success [93]. This work is primarily targeted at improving MBF quantification in the presence of recovery losses and signal mixing due to limited spatial resolution.

2.6.1   Recovery Loss

Figure 2-10 demonstrates a series of profiles representing the myocardial wall with an arbitrary width and having uniform, unity intensity (blue). The profiles are smoothed using Gaussian kernels with varying FWHM ranging from 0.1 to 2 times the object width. The resulting, blurred, profiles are shown with superimposed red lines. With a small blur (FWHM = 0.1) the intensity of the structure may be recovered sufficiently accurately (although never exactly), however, as the blur reaches the same order as the structure size (FWHM>0.5), the intensity of the structure cannot be recovered from the blurred image without some recovery correction. The recovery loss depends on the structure size, geometry, and the degree of smoothing. Thus recovery may not be uniform throughout the image and requires additional information to resolve accurately.
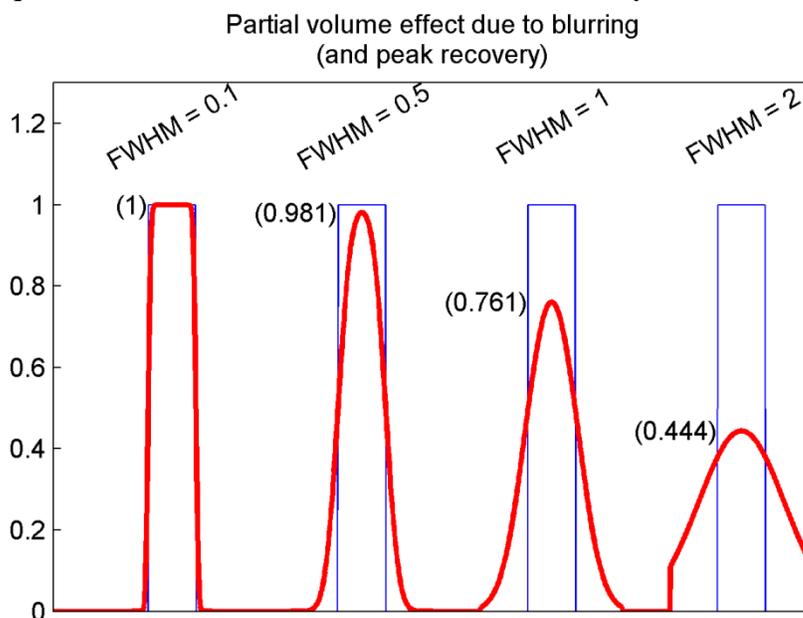
Figure 2-10 –Blurring due to finite spatial resolution leads to reduced recovery of image intensity. If the blur is much smaller than the object, full recovery is possible; however, as the blur increases image intensity (contrast) is reduced.

2.6.2   Signal Mixing

Recovery loss can also be regarded as a mixing problem [99] in which the object signal is mixed with the signals of the surrounding objects. In some cases the surroundings may consist of objects that contain no signal (no activity in all time frames) as in the example of Figure 2-10. The example in Figure 2-11 depicts a short-axis slice through a simulated LV (top row). The LV cavity consists of 100% blood and is surrounded by myocardium that is composed of 80% myocardial tissue and 20% blood. The total recovery in the heart region is uniformly 1 (or 100%) in both cavity and myocardium regions. The right-most plot shows a recovery profile along a line through the center of the image including blood recovery (red), myocardium recovery (blue), and their total recovery (TR) in black.

After applying a uniform Gaussian (FWHM = 2×myocardial wall thickness) smoothing the resulting recovery images and profiles are shown in the second row. The

profiles through the smoothed image reveal 90% blood signal and 10% myocardium signal in the center of the LV cavity as opposed to 100% blood signal in the unsmoothed case. In the myocardial region, the profile of the smoothed image recovers about 40% myocardium signal and 25% blood signal as opposed to 80% and 20% respectively in the unsmoothed example. Blurring effects result in increasing recovery errors as object sizes decrease relative to the image resolution.
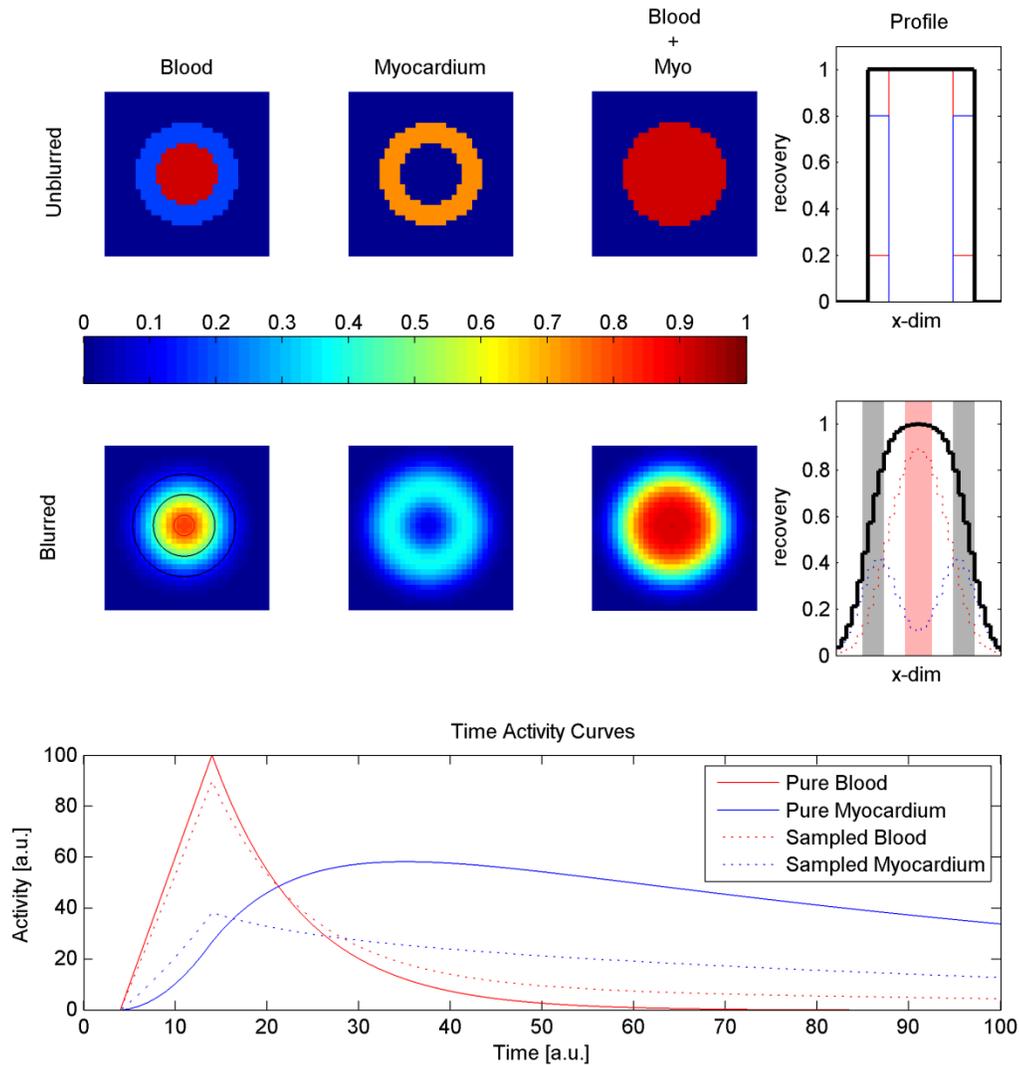
Figure 2-11 – Blurring effects on signal mixing and recovery losses. Pure blood and myocardium contributions are shown in the top row along with their sum and a profile along a line in the center of the image. After blurring the recovery in the myocardium is much reduced, as well as a slight reduction in the blood recovery. Pure TACs and sampled TACs (ROIs shown in blurred blood image) are compared in the bottom figure.

In Figure 2-11, blood and myocardium ROIs were defined as respective red and black regions in the blurred blood image (also shown as bars in the profile). The sampled blood TAC (dashed red line in the Time Activity Curve plot) and the sampled myocardium (dashed

blue line) can be compared with the respective pure TACs used during simulation (solid lines). Note that during late time frames the pure blood signal drops to zero, but the sampled blood reaches an asymptote that corresponds to ~10% of the myocardial signal which results from spillover from the myocardium into the blood sampling region. The sampled myocardial TAC is distorted, having an early peak activity relating to high blood contribution and low activity in the late frames due to recovery loss and the presence of blood in the ROI.

The TR in the blood region is nearly unity as in the unsmoothed image. In the myocardium region, however, the TR is ~65% which is ~35% less than in the unsmoothed image. Within the extent of the myocardium region, signal mixing with a third structure, outside the heart and having no activity, takes place which decreases the perceived TR. The effect becomes more pronounced as the sampling region is shifted further radially outward as demonstrated by the blurred total recovery image and profile.

2.6.3   Blood TAC Contaminations

Typically, blood input functions are sampled inside the LV or LA cavities. This region consists of a large blood pool, the size of which is favourable for reducing spillover effects. In addition, there is negligible transfer delay to the myocardium as the LV cavity is immediately upstream from the coronary arteries that perfuse the myocardium [45]. While TR loss may be small in the LV blood cavity, signal mixing can include as much as 60% myocardium signal in small rodents [54], children, or adults with small hearts. Consequently blood input functions may not be pure, resulting in inaccurate MBF quantification [75].

Contamination of the blood input function by myocardium signal is often observed as curves that either plateau in uptake phase to non-zero levels or even an increase in tracer concentrations. Perfusion tracers are designed to be taken up by the perfused tissue and retained. Thus, over time, the tracer is extracted from the blood. Although labelled-metabolites can accumulate in the blood (as with ammonia), this is not the case with ^{82}Rb [45].

Alternative ROIs such as the LA, ascending aorta, or descending aorta, which are fairly isolated from high uptake organs, may exhibit less signal contamination. However, these regions have been largely ignored due to their smaller feature sizes which results in reduced signal recovery, and therefore do not benefit MBF quantification.

Some have attempted to correct for recovery losses of the blood input function by measuring activity in an arterial blood sample taken from the subject during imaging [100,101]. The activity concentration of this sample is measured using an external apparatus and is then used to scale the blood input function. The assumption is that the shape of the blood input function is accurate, but it is scaled incorrectly. This approach has been limited to research applications due to increased technical complexity and the invasiveness of extracting arterial blood.

2.6.4   Myocardial TAC Contamination

Mixing of arterial blood and myocardium signal occurs in the myocardium ROI due to the limited resolution of PET as well as due to existence of arterial blood that perfuses the myocardium. The signal in the myocardial tissue ROI, $C_m(t)$, can be expressed as a weighted sum of arterial blood and pure myocardial signal as in equation 2-4. This form disregards contributions from neighbouring organs (e.g. lungs, RV blood, liver, and stomach). This equation does however accommodate non-active tissue, as its signal is zero at all time points and can therefore be removed from the summation of signal contributions.

To resolve ambiguity of tissue uptake and recovery loss, the myocardium TAC is more commonly expressed in the form of equation 2-6. While equation 2-6 can be uniquely solved, it neglects to account for contamination from non-active tissue outside the heart. One way to mitigate this inaccuracy is to sample the myocardium in a region that is slightly shifted towards the interior of the LV cavity (endocardium), thus minimizing the contribution of signals from tissues outside the heart [92]. This is equivalent to shifting the myocardial ROI in Figure 2-11 radially inwards. In doing so, the TR in the ROI increases, thus lowering the recovery loss. However, this approach is not likely to completely eliminate recovery loss.

In [92], the extra-vascular (non blood) RC was estimated by subtracting an image of the blood (using a [11]CO PET scan) from attenuation images to obtain an extravascular density image. A more clinically practical approach was also proposed in which early time frames of the perfusion scan were used to estimate a blood pool image, thus mitigating the need for a separate, co-registered [11]CO scan. Both techniques however, assume that certain regions in the blood pool contains 100% blood signal. This assumption may be naïve, due to limited resolution and uncorrected scatter.

Thus three major limitations of ROI based methods of MBF quantification have been illustrated: 1) Measuring pure blood input functions, 2) resolving RC, and 3) determining ROIs. Image decomposition approaches have been used in the past to estimate pure blood input functions, and may be beneficial for estimating RC as well. The next section introduces image decomposition with respect to MBF quantification.

2.7 Dynamic Image Sequence Decomposition

Image decomposition has been used successfully for many applications [102-113] in nuclear imaging. Each dixel (a pixel in a dynamic image sequence) represents the concentration of activity (Bq/cc) that is sampled in a finite volume over a sequence of time frames. Assuming that no motion has occurred between the patient and the camera during acquisition, each dixel represents the amount of tracer in a finite volume of the patient over time, and can be represented as a vector.

Each dixel may be treated independently of others in the image and can represent any temporal pattern. However, one may assume that the image is composed of a finite number

of components that have a spatial structure and a uniform temporal response. Under this assumption, one can decompose the original image sequence into a finite set of factors (temporal response) and associated structures (spatial distribution). Each dixel, $y(i,j)$, can then be reproduced through a linear combination of K factors, $f_k(j)$, which are weighted by K structures, $s_k(i)$, as demonstrated in equation 2-9, where j indexes the time frame and i indexes the pixel in the image. The product of corresponding factor and structure pairs define the dynamic image sequence of a single component. The sum of these components estimates the original image sequence. The remaining part of the image that is not modelled by the factors and structures, $e(i,j)$, is referred to as the error or residue.

$$y(i,j) = \sum_{k=1}^{K} f_k(j)\, s_k(i) + e(i,j)$$

where, $y(i,j)$ – i^{th} dixel at time frame j **2-9**
$f_k(j)$ – the jth time frame of factor k
$s_k(i)$ – the ith pixel in the structure k
$e(i,j)$ – the error in the ith pixel at time frame j

The literature refers to factors and structures using different names depending on the field, author, application, and context. Some of these terms are listed in Table 2-4.

TABLE 2-4 – FACTOR AND STRUCTURE TERMS

Name in this work	Factors	Structures	
Other names	Basis Vectors	Factor Images	Image Coefficients
	Profiles	Factor Coefficients	Projections

Different tissues interact differently with the tracer and therefore may exhibit different temporal responses (or TAC shapes). This notion has led to decomposition of images based on characteristic temporal responses of the tissues which comprise the image. In the context of cardiac PET images, decomposition attempts to recover components of the heart image such as right cavity blood, left cavity blood, and myocardium (shown in order from top to bottom on the left half of Figure 2-12). The factors define the time-activity curves of the components, while the structures define the spatial distribution of these factors. Each dixel signal is composed of signals from several types of tissues which may spatially overlap in the image due to anatomy, uncorrected scatter, finite image resolution, and motion. The summed products of well defined factors and their structures should reconstruct the measured signal (minus some noise or excluded component) as demonstrated in Figure 2-12.
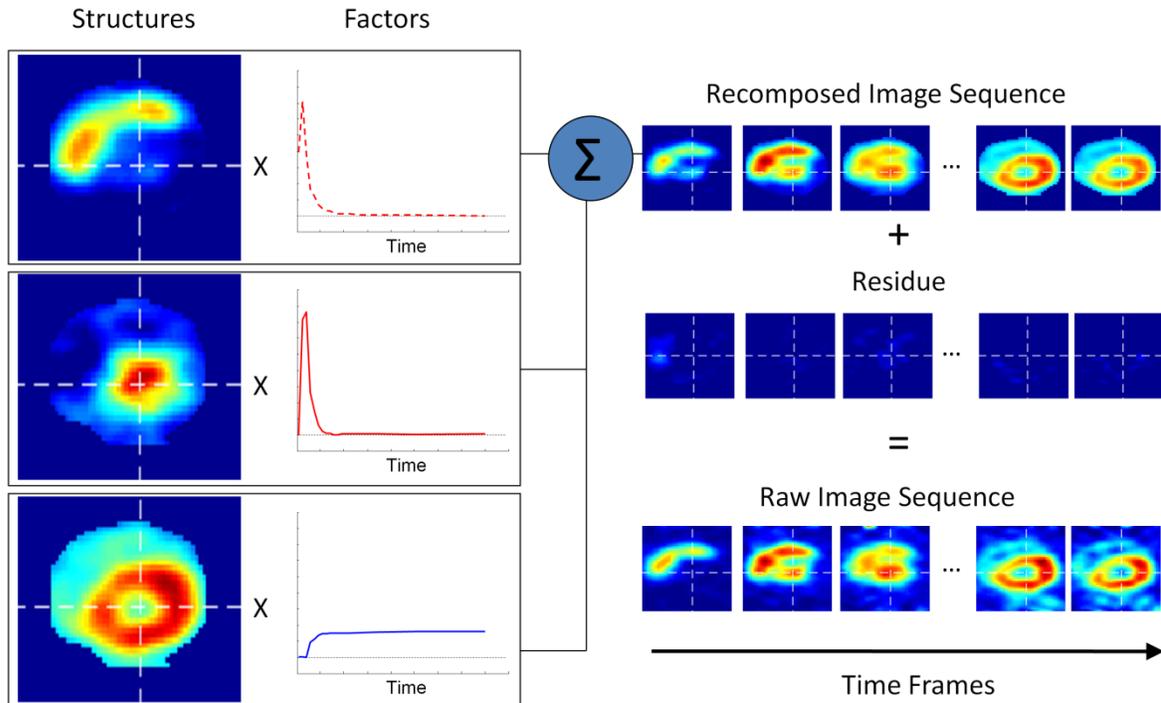
Figure 2-12 – Image decomposition into structures (spatial distribution) and corresponding factors (temporal response) can be used to reconstruct the original image sequence minus some residual signal. Diagram is from a short axis slice through a canine heart showing RV, LV, and myocardium components (from top to bottom on left).

Dynamic PET images are represented as 4D data sets (3 spatial dimensions and one time dimension). In most cases, decomposition does not place an emphasis on the spatial relation between dixels; it is, therefore, convenient to rearrange the data in a 2D dataset. The columns of the data matrix, *Y*, represent the time samples while the rows contain the dixels in an order that can be reversed to reform the images. Thus a more convenient matrix notation may be used as in equation 2-10 where *Y* is the measured data, *S* is the structures matrix, *F* is the column-wise factor matrix and *ε* is error or noise in the image.

$$Y=FS+\varepsilon \qquad\qquad \textbf{2-10}$$

Decomposition is a double blinded problem, meaning that both structures and factors are unknown, and for this reason there is no single solution to the decomposition problem. Various decomposition approaches (some of which are listed in Table 2-5) have been developed for different applications and rely on different assumptions and goals. While some decomposition methods are general and rely on general mathematical concepts, others are ad-hoc and target a specific application.

TABLE 2-5 – COMMON IMAGE DECOMPOSITION METHODS

Name	Description (with relation to sequences of images)
PCA - Principal Component Analysis	Maximizes the variability in the image that is accounted for by each factor in decreasing order.
ICA - Independent Component Analysis	Maximizes the independence between factors under the assumption that the sum of independent random distributions has a Gaussian distribution.
CA - Cluster Analysis	Groups together adjoined clusters with similar temporal characteristics. Typically designed to restrict spatial overlap between components.
FA - Factor Analysis	A broad definition that typically encompasses application dependent constraints. Typically optimizes the linear combination of PCA derived factors to compute new basis (factors).

2.8 Matrix Decomposition Methods

As stated above, a dynamic image may be represented as a two-dimensional matrix with the dixels running along the rows and time frames along the columns or vice-versa. Once the dynamic image is represented in a matrix form common matrix decomposition processes may be applied. Matrix decomposition methods have been developed for a wide range of applications including data-mining, data compression, noise removal, group classification, and separation of signal sources. The following is a brief overview of common matrix decomposition methods and their relevance to image decomposition of dynamic ^{82}Rb cardiac PET image sequences.

2.8.1   Principal Component Analysis – PCA

The most common and simplest decomposition method is PCA [11]. This technique determines the Eigenvectors of the covariance matrix and uses them as a basis for decompositions. In doing so, the resulting basis contains orthogonal vectors that represent the maximal amount of image variance. The relative amount of variance represented by each Eigenvector is proportional to the corresponding Eigenvalue. Therefore PCA is ideal for determining the number of basis vectors required to represent a given percentage of the variance of a data set (section 2.9.2). PCA is useful for data compression and noise removal and benefits of a simple, well defined implementation that executes quickly on modern computers even for very large data sets. The PCA algorithm consists of the following steps:

1. Subtract the data mean, $\overline{Y}$, from the data, Y, along each dimension, so that the resulting mean is zero $Y_C = Y - \overline{Y}$
2. Compute the covariance matrix $C = Y_C^{\mathrm{T}} Y_C$
3. Compute the Eigenvalues ($\lambda_1, \lambda_2, ..., \lambda_N$) and Eigenvectors ($E_1, E_2, ..., E_N$) of the covariance matrix C.

4. The Eigenvectors form the basis of the data, and the Eigenvalues may be used to order them by the amount of variance in the data that they represent. The factor matrix columns are composed of the $K \leq N$ Eigenvectors ($\boldsymbol{F}=[E_1 \quad E_2 \quad \ldots \quad E_K]$).

5. The structures are then computed as $\boldsymbol{S} = \boldsymbol{FY_C}$

The original image may be recomposed using: $\tilde{\boldsymbol{Y}} = \boldsymbol{F}^T\boldsymbol{S} + \bar{\boldsymbol{Y}}$ since $\boldsymbol{F}^T\boldsymbol{F}=\boldsymbol{I}$ in this case due to $\boldsymbol{F}$ being orthonormal. If the condition $\sum_{i=1}^{K} \lambda_i = \sum_{i=1}^{N} \lambda_i$ is met, then $\tilde{\boldsymbol{Y}} =\boldsymbol{Y}$, and the original image can be completely recomposed.

2.8.2   Cluster Analysis - CA

Cluster analysis is a classification method that categorizes samples into groups with similar attributes by measuring the distance between each sample and group bases [114]. The attributes by which samples are classified can either be based directly on the samples themselves (for example based on the temporal response of each dixel) or derived indirectly from the samples (for example using the kinetic model parameters corresponding of each dixel). Cluster Analysis is a broad term as it does not specify how the groups are defined nor does it specify how the distances (or similarity) between samples and groups is measured.

Being a classification method, cluster analysis may be most suitable for defining dixels as belonging to one tissue or another. However, cluster analysis is not intended to define the mixing of signals in an image and therefore is not ideal for decomposing dynamic image sequences in a physiologically accurate manner.

2.8.3   Independent Component Analysis - ICA

ICA focuses on resolving basis vectors (factors) which are independent and non-Gaussian based on the central limit theorem, which states that the sum of independent random non-Gaussian signals approaches a Gaussian distribution [115]. ICA iteratively resolves basis vectors that are non-Gaussian. The Gaussian properties may be determined in several manners, such as kurtosis, negentropy (negative entropy), and approximations of the negentropy, all of which (in theory) should give similar measures. The measure of a Gaussian's kurtosis should be zero (3 by some definitions), thus a minimization function may be implemented to reduce the kurtosis of all components.

The underlying assumptions of ICA may also be its limitation in the case of decomposition of cardiac PET images into physiological components. There are no strict physiological reasons why the factors cannot have a Gaussian distribution. More importantly, it is known that the activity concentrations in different tissue types are related (as is demonstrated by tracer kinetic models), which violates the independence assumption of the central limit theory.

2.8.4　Factor Analysis - FA

FA is typically presented as an expansion of PCA [11] in which the PCA derived basis vectors are rotated to enforce specific conditions on the solution [116]. These constraints are intended to provide a solution with favourable properties for the specific application. Methods of rotation can be broken up into two types:

- Orthogonal rotation – The basis vectors are rotated in such a manner so that they remain orthogonal (linearly independent) to one another.
- Oblique rotation – The vectors may be rotated in any manner. This more general method accommodates cases in which factors are not necessarily independent of one another

Regardless of which approach is used to rotate the basis vectors, these remain a linear combination of the basis vectors derived by PCA. Therefore, factor analysis still accounts for the maximum possible variance in the image given the number of factors [117,118,119].

2.8.4.1　Factor Analysis of Dynamic Structures (FADS) and Factor Analysis of Medical Image Sequences (FAMIS)

The FADS algorithm was introduced in 1980 [120] for decomposition of dynamic planar scintigraphy. FADS has subsequently been expanded to other applications [121] and is still popular within the medical image analysis community. In 1992 FADS was incorporated into FAMIS, a software package for decomposition of multidimensional images, as its decomposition engine [107]. The FADS method consists of the following steps:

1. Data pre-processing – a subset of dixels is selected by thresholding. These dixels are then scaled and centered.
2. PCA – the scaled and centered dixels are decomposed using PCA to determine the basis vectors.
3. Oblique Rotation – the basis vectors are obliquely rotated using an iterative apex-seeking algorithm with a non-negative constraint which defines a polytope that encompasses the projection of each scaled and centered dixel onto the basis vectors. Thus the factors are determined as the apices of the polytope.
4. Factor Image Computation – The original dixels are finally projected on to the factors to produce the structures.

FAMIS is a general purpose software package that can be used for any multidimensional image (such as SPECT, PET, fMRI, x-ray CT, etc) [122]. FAMIS provides tools to supervise and intervene in the decomposition process, and to view and analyze its results. FADS and FAMIS have been used to decompose dynamic images as well as to decompose energy-dependent images in which the energy dimension replaces the time dimension of the image [112].

2.8.4.2   Least Squares Factor Analysis

The main limitation of the FADS algorithm is the inability to constrain the solution with *a priori* information. Although additional constraints may be applied to the FADS-derived solution [106,122,123], it is not possible to include *a priori* information during the PCA phase in which the solution subspace is determined. Optimization of an objective function is a more general framework that can incorporate any set of *a priori* information [108] and is summarized by the set of equations 2-11. An optimization problem is generally posed as a minimization of a cost function, f_{tot}, by adjusting the factors matrix, $\boldsymbol{F}$, for a given image, $\boldsymbol{Y}$. The cost function includes terms for minimizing the magnitude of the error matrix ($|\boldsymbol{\varepsilon}| = |\boldsymbol{Y}–\boldsymbol{FS}|$) as well as penalties for negative factors ($f_{neg}(\boldsymbol{F})$), negative structures ($f_{neg}(\boldsymbol{S})$), and additional priors ($f_{prior}(\boldsymbol{F},\boldsymbol{S}|\boldsymbol{Y})$). Each penalty must be weighted (w_F, w_S, and w_p) according to predefined criteria.

$$F = \min_{\boldsymbol{F}} f_{tot}(\boldsymbol{F},\boldsymbol{S}|\boldsymbol{Y})$$
$$S = inv(\boldsymbol{F})\boldsymbol{Y}$$
$$f_{tot}(\boldsymbol{F},\boldsymbol{S}|\boldsymbol{Y}) = \|\boldsymbol{Y} - \boldsymbol{FS}\| + w_F f_{neg}(\boldsymbol{F}) + w_s f_{neg}(\boldsymbol{S}) + w_p f_{prior}(\boldsymbol{F},\boldsymbol{S}|\boldsymbol{Y})$$

$$\textbf{2-11}$$

Since the optimization approach always includes a term for minimizing the sum of squares of the error matrix, this approach is commonly referred to as the least squares method [124]. The factor analysis term does not strictly apply to the least squares method as there is no rotation of an orthogonal set of basis vectors.

2.8.5   Other Decomposition Methods

While the above mentioned decomposition methods describe general approaches to decompose a dataset, many applications are addressed by ad-hoc algorithms. Hybrid methods may combine the principles of more than one decomposition method. For example CA may be applied to ICA derived structures in order to determine cluster regions with similar dynamics [125]. In addition, a known stimulus may be used as one of the factors [125], or one of the factors may assume to have a temporal response defined by a function with free parameters which are resolved during decomposition. Since many ad-hoc approaches have been referred to as factor analysis, in the context of nuclear medicine factor analysis is often used as a general term for decomposition of image sequences.

2.9 Quantitative PET Image Decomposition

2.9.1   Scaling of Factors and Structures

The units of the image, $\boldsymbol{Y}$, are defined by the experiment. In the case of PET, images are typically expressed in units of activity concentration (e.g. Bq/cc). When the image is decomposed, the units may also be decomposed; however the product of the factor and structure units must always be equal to the units of the original data to remain quantitative.

Thus the factor and structure units are coupled. Example decompositions of activity concentration units include:

$$
\begin{array}{rcccc}
[\text{Bq/cc}] = & & [\text{Bq/cc}] & \times & [1] \\
& & [\text{Bq}] & \times & [\text{cc}^{-1}] \\
& & [\text{Bq/cc / cc}] & \times & [\text{cc}]
\end{array}
$$

The relationship stated in equation 2-10 can also be expressed in the form of equation 2-12 where S' and F' represent the structures and factors respectively on an arbitrary scale. A rotation matrix, R, can be used to convert S' and F' to S and F respectively. If R is a diagonal matrix, then it simply scales the factors and structures without changing their pattern. This representation demonstrates that scaling factors and structures is not unique without an additional constraint.

$$
Y - E = FS = \underbrace{F'R}_{F}\ \underbrace{R^{-1}S'}_{S}
\qquad \textbf{2-12}
$$

In the literature the units of factors and structures are often not disclosed [106,108], or the factors are normalized to unit integral [104]. For quantification of physiologic function from images it is desirable that factors quantify the activity concentration in a volume of pure tissue [Bq/cc] and, correspondingly, structures quantify the recovery [0-1] of each component to each dixel [108].

2.9.2   Number of Components

Regardless of the decomposition methods the number of components in the image must be predetermined. The quality of the image, number of organs, uniformity of the organ kinetics, and time frame intervals all play a role in the number of unique components that can be resolved reliably. If too few components are resolved, tissues with similar kinetics may be lumped together, each having error in different phases of the image sequence. If an excessive number of components are decomposed, an organ may be split between two or more components having different kinetics. As the number of components grows the decomposition process may become excessively sensitive to noise [126].

The number of factors, K, must be greater than one and less than or equal to the smallest dimension in Y. Since the number of time frames, M, is usually much smaller than the number of pixels, N, in an image, then $2 \leq K \leq M$.

In cardiac imaging, one may expect to resolve a myocardium component and either one or two blood components, depending on the early frame lengths relative to the blood transit time between right and left heart chambers [110]. An additional component may be resolvable if other tissues (i.e. liver or stomach) are included in the field of view and have kinetics differ significantly from the myocardium [109].

It is common practice to set the number of components based on the nature of the image and/or user experience. Alternatively, a desired variance in the image sequence that should be reproduced by the components can be set [104,120]. The Eigenvalues of the covariance matrix (loading factors), which can be obtained using PCA, are normalized to a sum of 1. The loading factors are then sorted in decreasing order, cumulatively summed, and thresholded by the desired image variance. This method is demonstrated in Figure 2-13 with the threshold shown in blue. The vertical axis of the plot is the cumulative normalized and sorted Eigenvalues and the horizontal axis is the number of factors. The data points in a high quality image will increase rapidly within the first few factors giving the curve a knee shape, while a noisy image will approach a diagonal from the origin to the point (M,1).
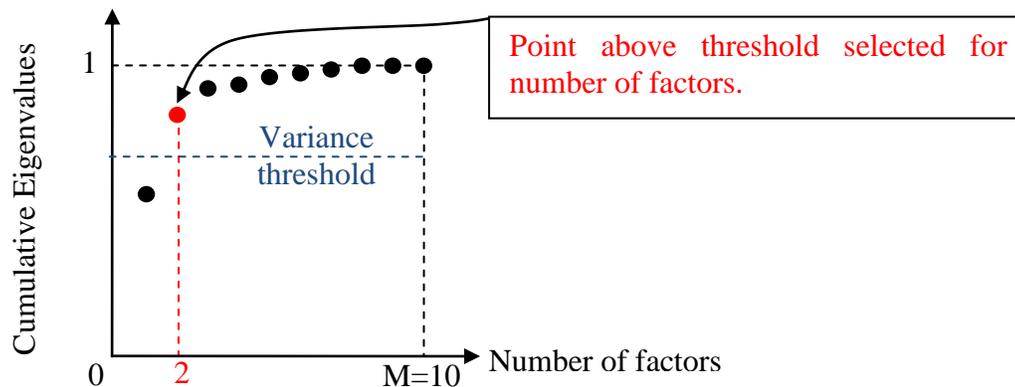
Figure 2-13 – Demonstration of a method for resolving number of factors, K, based on the cumulative Eigenvalues of the image covariance matrix, which corresponds to the image variance.

2.9.3   Assumptions of Image Decomposition

2.9.3.1   No Motion

Dynamic imaging inherently assumes that the subject has remained stationary relative to the camera during the entire imaging process so that each dixel corresponds to the same finite volume of the subject throughout the scan. This assumption may be violated either by motion of the patient (coughing, relaxing, fidgeting, etc.), or by motion of the organs as they settle under the patient's posture during the scan. Patient motion is kept to a minimum through coaching, ensuring patient comfort, and restraints, whereas animals are placed under anaesthesia. However, little can be done to counter the motion of internal organs aside from providing sufficient time between subject placement in the camera and beginning of the image acquisition.

In the presence of motion, dixels in heterogeneous regions (having organs with diverse physiology) may exhibit signals that are not physiologic. For example a region in the epicardium (outer wall of the myocardium) may contain myocardial signal in early frames, and lung signal in later frames. A region in the endocardium (inner wall of the myocardium) may contain myocardial signal in early frames and blood signal in later frames.

The effect of motion on factor analysis results may be unpredictable. One possible scenario is the need for a greater number of factors to account for the same amount of variance in an image without motion. Another possibility is that some dixels may be composed of an erroneous linear combination of factors (error in structures). Finally it is possible that erroneous factors will be resolved. In any case, without the use of motion detection and correction, the scan may be of little value for accurate quantification. Common practice assumes that motion is non-existent and is only investigated in extreme cases. Typically, as is in this work, cases with motion are disqualified from further interpretation.

2.9.3.2   No Scatter

Scatter results from interactions of the photons in the medium, and is typically corrected during reconstruction. However, scatter may not be completely removed from the image. Scatter is a relatively uniform background activity within the heart, but its pattern may change with the distribution of activity. Therefore it can be regarded as an additional spatial blur of the image with a very broad kernel and its most likely effect is myocardium scatter into the blood pool.

2.9.4   Physiologic Validation of Factors and Structures

The limited application of image decomposition techniques for MBF quantification may be partially due to poor validation of the results from a physiologic perspective. In the absence of suitable standards to which factors and/or structures can be compared, simulations are often the only means. A set of structures and factors are defined and used to compose a dynamic image sequence. The image is then decomposed and the results are validated against the simulation data. Varying simulations can be used to characterize the decomposition results and assess robustness. Simple structures can be advantageous to qualitatively evaluate the accuracy of the structures and their preservation of intensity uniformity. Varying factors can give insight to the accuracy with varying physiology.

A drawback of simulations is that relevance to real images may be limited by the accuracy of the simulation in replicating the real imaging process. While simulations are becoming ever more sophisticated, the need for anatomic and physiologic standards remains.

Blood sampling is by far the most common means by which a factor may be validated [110,127,128,129]. Blood samples may be taken at set time intervals and assayed with an external activity counter and adjusted for volume so as to obtain activity concentration samples to which a blood factor may be compared. Alternatively, a continuous withdrawal of blood using a pump can be fed through an activity counter that samples the activity every few seconds. The blood-sampler can generate curves of the activity concentration in the sampled blood over time [45,130].

While structures are only validated qualitatively in the literature, images obtained by other means may serve as anatomical standards. Images of the blood pool may be obtained

with PET using either ^{11}C or ^{15}O labelled carbon-monoxide (CO), which binds to the haemoglobin in the blood [92]. Blood pool imaging may be a good anatomical standard by which to validate blood structures. Magnetic resonance imaging (MRI) or contrast-enhanced x-ray CT may both be used to generate images of the myocardium by which to validate the myocardial structure. However, these images would have to be averaged over the entire cardiac and respiratory cycles and sufficiently blurred in order to reproduce PET image quality.

In the absence of anatomic or physiologic standards, experimental data could be used to evaluate desirable properties of the decomposition process. For example, repeat imaging of the same subject under variable conditions could ensure that the structures are reproducible and reflect the constant anatomy.

2.10 Summary

While factor analysis has been the focus of research for over three decades, it still has not delivered an improvement in quantification of cardiac function. Factor analysis has been useful in defining myocardial regions of interest [75,90,111,131], and has been shown to resolve accurate input functions [102,110]. The failure of factor analysis therefore can be attributed to poor ability to derive accurate output functions [48] and/or to poor ability to scale factors and structures to correct for recovery losses.

The following chapter describes an ROI based method for quantification of MBF that has been previously validated [39] and the operator-dependent variability is evaluated. In the subsequent two chapters (Chapter 4 and Chapter 5) a physiologically accurate method for decomposing dynamic cardiac PET image sequences is developed. Finally, Chapter 6 evaluates MBF quantification using factor analysis.

Chapter 3.

Highly-Automated Region of Interest Based [82]Rb MBF Quantification

This chapter discusses operator-dependent variability of FlowQuant, a myocardial blood flow quantification software package that is being developed at the University of Ottawa Heart Institute. Ran Klein is the primary author on this publication and has developed the FlowQuant menu interface, image orientation method, and LV segmentation method. This section also explains methods that are referred to in later chapters. This work is used as the standard of comparison for the factor analysis methods that are developed in subsequent chapters. The content of this chapter has been published [132] and a few changes (particularly in the background section) have been made to the text to improve readability as part of this thesis.

3.1 Background

Accurate MBF measurement using [82]Rb PET has been previously demonstrated [39], but precision has not been evaluated. High precision is important for detection of serial changes during disease progression or therapy [66,84] and is evaluated through test-retest reproducibility [58,63,76,81,82,85,86,87,88], of which operator-dependent variability [53,71,85,89,90] is an important factor [91]. However, there are few reports of reproducibility of MBF quantification using [82]Rb PET [72].

Several software packages with the ability to quantify MBF from cardiac PET images have recently become available [71,72,73]. In this work, a highly automated image processing workflow to reduce operator variability in MBF quantification by minimizing user interactions [91,133], is presented. Assessment of the inter-operator and intra-operator variability for quantification of MBF, flow reserve, and flow differences using [82]Rb PET follows. The operator-dependent variability for MPI, which is referred to as relative uptake in this study, is also evaluated.

3.2 Methods and Materials

3.2.1 Patient Cohort

Thirty consecutive clinical patients that underwent a rest-stress [82]Rb perfusion scan at the University of Ottawa Heart Institute, National Cardiac PET Centre, between the 15th and 26th of June, 2009 were selected. All patients gave informed consent under a cardiac PET registry study approved by the Ottawa Heart Institute Research Ethics Board. Patients were

instructed to abstain from caffeine intake for 12 hours prior to the exam, beta-blockers for 24 hours, and fast for at least 4 hours.

3.2.2   Image Acquisition

Scans were acquired according to the standard clinical protocol as outlined in Figure 3-1. Following a scout scan for patient positioning, a low-dose (0.5 mSv) fast CT scan (1.5 s) was performed for attenuation correction of the rest data. ^{82}Rb (10 MBq/kg) was administered intravenously using a custom infusion system [35] over a 30 s interval to limit the deadtime of the camera detectors to <35% and to ensure accurate measurement of the bolus first-pass activity [36]. Dynamic data were acquired in 3D mode using a Discovery RX PET-VCT scanner (GE Healthcare, Waukeshaw, MI), and images of activity concentration were reconstructed using Fourier rebinning and filtered backprojection with a 12 mm Hann filter, into 15 time frames (10s × 9, 30s × 3, 60s × 1, 120s × 1, 240s × 1).

Dipyridamole (0.14 mg/kg/min) was infused for 5 min, and ^{82}Rb imaging initiated 3 min later following the same protocol used at rest. A second low-dose CT scan was then performed for attenuation correction of the stress ^{82}Rb data.
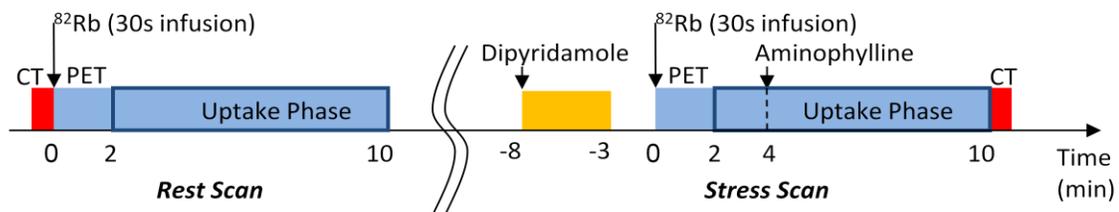
Figure 3-1 – Clinical rest-stress ^{82}Rb PET/CT protocol using Dipyridamole pharmacologic stress.

3.2.3   Image Analysis

A software program (FlowQuant, Ottawa, Canada) was developed for quantification of cardiac molecular function using a variety of tracers and in several different species. The rest-stress workflow started with processing of the rest scan, continued with a nearly identical process for the stress scan, and ended with the stress-rest flow reserve analysis as illustrated in Figure 3-2. Default software settings in version 2.1.3 (July 2009), as shown in Table 3-1, were used in this study.

TABLE 3-1 –SOFTWARE PROCESSING PARAMETERS USED IN ANALYSIS

Parameter	Value		Parameter	Value
Uptake frames	Last 5		Dynamic polarmap smoothing Type	Gaussian
Uptake frame sum weighting	Off		Dynamic polarmap smoothing kernel	1.5 pixels
Uptake image resolution	12 mm		Blood spillover correction	Off
Myocardium radial search range	140%		Global recovery coefficient estimation	Off
Endocardial radial sample	2 mm		Blood input function ROI	ABC
Epicardial radial sample	2 mm		Kinetic modeling fast flag	On

3.2.4   Volume Reorientation

Uptake images were generated by averaging the last 5 time frames (8 minutes) to maintain high myocardium:blood pool contrast and reduce image noise. The uptake images were automatically processed to detect the location, orientation, and size of the LV myocardium (Figure 3-3A,B). Ellipses were fit to the myocardial data in 3 orthogonal planes in an evolving reference frame. The benefits of working with 2D planes rather than the full 3D volume are reduced computational complexity and the ability of the operator to supervise the process and intervene as needed. The process was fully visualized using the reorientation graphical user interface (GUI) shown in Figure 3-3C.
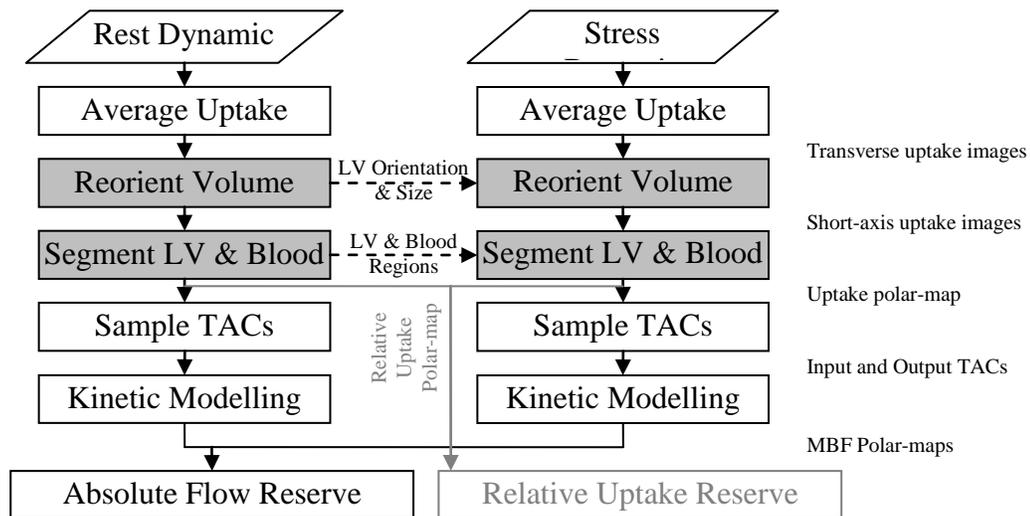
Figure 3-2 – Dynamic [82]Rb rest-stress analysis workflow. Rest and stress dynamic images are used to generate relative uptake, absolute MBF, and flow reserve polar-maps. The process is fully automated, with some user interaction possible at the reorientation and segmentation stages (gray filled boxes).

The LV processing began with automatic selection of a transverse plane intersecting the LV. In this transverse plane, the LV position was estimated using the center of mass of the pixel intensities. A full ellipse was then optimized to correlate with the uptake image as follows. An optimization function maximized the correlation between the region overlapping a partial ellipse and its neighbourhood, by modifying five free parameters (x and y translation, ellipse rotation, and two ellipse dimensions (*a* and *b* in Figure 3-3B). A mid vertical-long-axis (mid-VLA) image was created orthogonal to the transverse plane, along the estimated long-axis. A partial ellipse (4/3 of the long axis) was optimized in a similar manner with initial estimates of the ellipse location and dimensions derived from the previous stage. In theory, the LV orientation and position should be completely measured at this point, but a third orthogonal image along the mid horizontal-long-axis (mid-HLA) plane was also processed to further optimize the transverse rotation.

For quality assurance (QA) purposes a fourth orthogonal, short-axis (basal-SA) image was displayed, which should have a circular pattern centered on the long axis, shown with

cross-hairs in Figure 3-3C. For further validation the operator could toggle the display to view a mid-ventricle-SA image.

For the rest scans, the initial parameter estimates at each orientation stage were based on characteristic values for the species type (human in this case). For stress scans, the LV myocardium size (ellipse dimensions) and orientation (angles) were presumed to be fixed and equal to those of the rest scan, but the positions could change. The LV position in the rest image was used as an initial estimate of the LV position in the stress image.

The graphical report (Figure 3-3C) displays the results of the optimization process, which also enabled the operator to intervene at each stage if necessary by manual adjustment of the fitted ellipses. Automated processing would continue from the point of intervention to minimize operator bias on the final results. If no operator intervention was performed, then the reorientation process was fully automated as described. Any operator interaction was labelled on the report for retrospective QA.
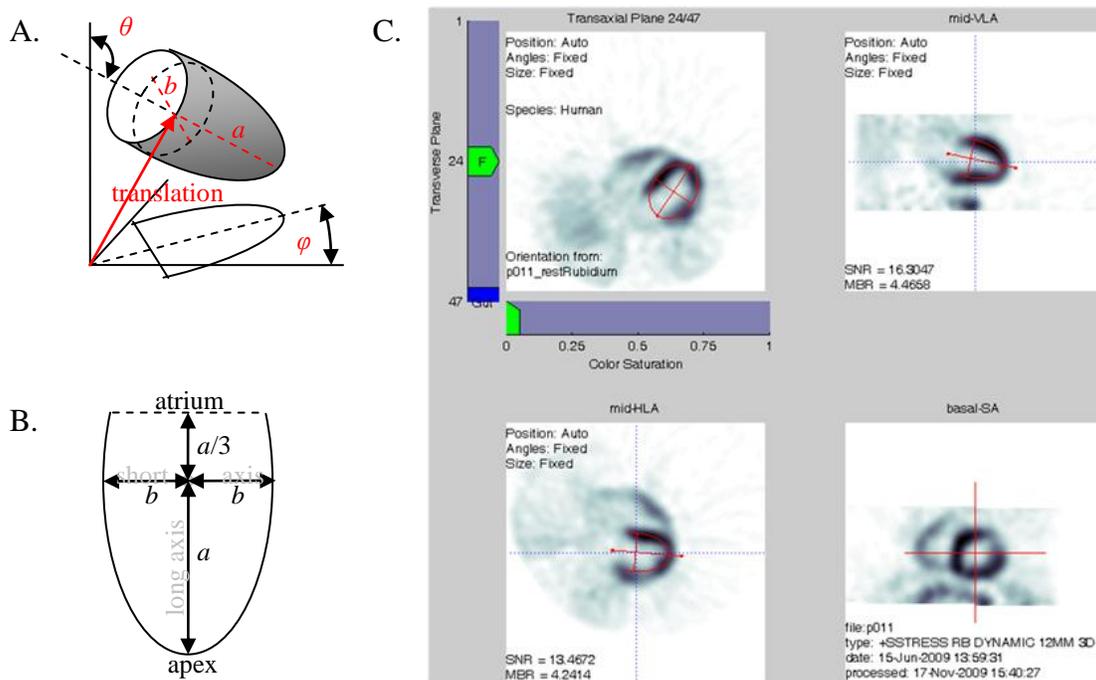
Figure 3-3 – A. LV ellipse model and orientation in relation to the scanner reference frame. The axial angle φ and the sagittal angle θ describe the orientation in 3D. B. Partial ellipse used to model a mid-VLA cross-section. The ellipse dimensions are a and b along the long and short axes respectively. C. Automatic orientation GUI.

3.2.5   LV and Blood Pool Segmentation

The transverse uptake images were reoriented to form 20 standard SA slices from apex to base, plus 3 slices beyond the apex and 3 slices past the base (in the atrium), thus the SA slice thickness was determined by the total long axis extent (4/3 *a)*. The SA pixel dimensions were unchanged from those of the original image.

The reoriented SA volume was sampled in a combined conical and planar coordinate system to generate a combined series of LV slices as shown in Figure 3-4. The first 9 slices relate to the conical sampling of the apex, while the remaining 15 slices are SA planes from apex to atrium. The slice planes are superimposed (white dashed lines) on the VLA and HLA images in the right hand side. This coordinate system was used to define myocardial sample points at fixed (10°) angular intervals according to their radial distance from the LV long axis. Rather than fitting each point individually, a spline model was used to optimize the radii of 4 control points (at 90° intervals) in 3 slices (LV cavity, base, and atrium), as well as one control point at the apex as shown in Figure 3-4.
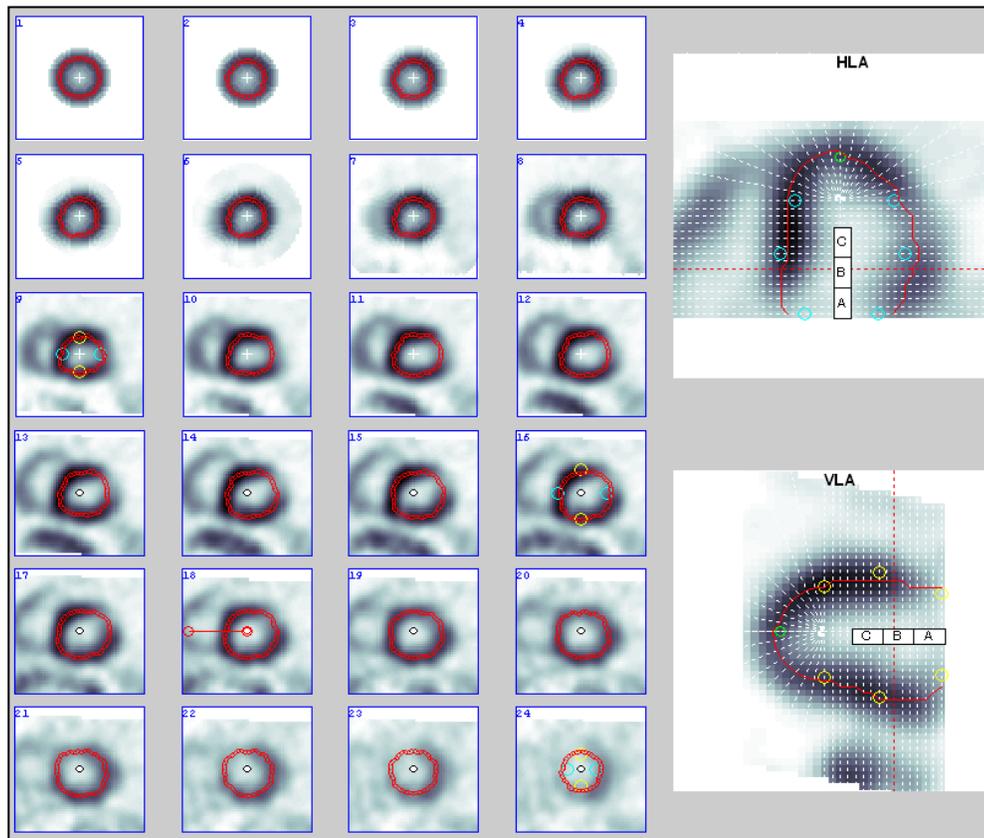
Figure 3-4 – Myocardial segmentation on conical (1-9) and planar (10-24) slices of the same case as in Fig. 3c. Vertical and horizontal long axis slices are also shown on the right, with the dashed lines depicting the locations of the slices to the left. The red contour lines show the myocardial sampling regions, and the yellow and cyan circles are the spline model control points. The white crosses indicate the long axis and the black circles indicate the blood ROIs.

The spline optimization algorithm minimized a cost function, C_{energy}, that resulted in maximization of the image energy overlapping the spline model, as shown in 3-1, where u_m is the pixel of maximum intensity in the uptake image and u_i is the ith pixel in the ROI defined by the spline model.

$$C_{energy} = \sum_i \frac{u_m - u_i}{u_m} \qquad \textbf{3-1}$$

Penalties, with the weights and limits empirically determined [134], were applied to discourage abnormal myocardial shapes by minimizing the following metrics:

1. Eccentricity of SA – the LV should be somewhat circular, thus if slices with a variation of radii greater than 30% exist, a penalty was applied.

$$C_{elip} = \begin{cases} 0 & e < 0.3 \\ e & e \geq 0.3 \end{cases} \qquad e = \max_i \left[\left| \log(r_{hor_i} / r_{ver_i}) \right| \right] \qquad \textbf{3-2}$$

2. Relative size of atrium – the cross section of the atrium should not be substantially bigger than that of the ventricle, thus a penalty was applied if the mean of its radii was more than 20% larger than the mean of the radii of the basal and cavity sections.

$$C_{atrium} = \begin{cases} 0 & a < 1.2 \\ a & a \geq 1.2 \end{cases} \qquad a = \frac{1}{2} \frac{r_{hor_{atrium}} + r_{ver_{atrium}}}{r_{hor_{cavity}} + r_{ver_{cavity}} + r_{hor_{base}} + r_{ver_{base}}} \qquad \textbf{3-3}$$

3. Offset of center of ellipse from LV long axis - the LV myocardium should be nearly centered on the LV long axis, thus a penalty was applied if the center of the myocardium was displaced from the LV long axis by more than 40% of the mean radius in the same slice.

$$C_{offset} = \begin{cases} 0 & o < 0.4 \\ o & o \geq 0.4 \end{cases} \qquad o = \max_i \left[\frac{2o_i}{r_{ver_i} + r_{hor_i}} \right] \qquad \textbf{3-4}$$

The final cost function, C, defined by equation 3-5 accounted for all the above penalties while rewarding high pixel intensities in the LV model ROI (low C_{energy}). Thus the LV model was constrained to have a characteristic shape, but abnormal myocardial shapes could be accommodated by the model, provided the image intensity is sufficient to offset the penalties.

$$C = C_{energy}(1 + 10 \times C_{elip} + C_{atrium} + C_{offset}) \qquad \textbf{3-5}$$

For the rest scans, initial estimates of the spline points were based on the ellipse sizes determined in the reorientation stage. For the stress scans, the spline points from the rest scan were used as initial estimates. Having a spline model with only 13 degrees of freedom afforded fast execution of the optimization algorithm as well as simple operator intervention. For quality assurance, the operator could monitor the automated sampling and intervene as needed by manipulating the radial position of the spline control points.

The myocardial radii determined from the spline model (36 points per slice x 24 slices= 864 points) were each shifted to the local maximum intensity position to account for regional shape variations. Local smoothness was enforced using a 2D median filter of the myocardial radii. Myocardial uptake values were averaged within regions of interest with specified endo- and epi-cardial extent (4 mm thickness) centered on the 864 LV sample points.

The sampled uptake activity was viewed as a polar-map and as a 3D model for quality assurance of the segmented LV shape, as demonstrated in Figure 3-5. For subsequent analysis in this study the LV polar-map was considered as the inner 16 of 24 slices, which excludes the membranous septum and basal lateral wall.

The standard 17 segment model was applied and segments were averaged according to ASNC guidelines [46] into 3 vascular territories corresponding to the major coronary arteries: left anterior descending (LAD) artery, left circumflex (LCX) artery, and right coronary artery (RCA).

Three blood regions of interest were placed automatically in the LV cavity (C), base (B), and left atrium (A) as shown on the VLA and HLA images in Figure 3-4. The extent of each region was predefined for each given species (8×8 mm in humans), and their length was 4 SA slices each. The regions were shifted in each SA plane to center the ROI in the cavity and maximize the distance from the myocardium, to minimize myocardial spillover into the blood region.

3.2.5.1   TAC Sampling

The sampling points from the registration stage were applied to all of the time frames of the dynamic image sequence to generate time-activity-curves (TAC). In the myocardium, a TAC, $C_{meas}(t)$, was generated for each sample point resulting in 576 TACs (36×16 rings). In the blood, three TACs were generated for the cavity, base, and atrium blood pool regions. In order to reduce noise, the median of the three blood region TACs was used as a blood input function for tracer kinetic modelling (Figure 3-6).
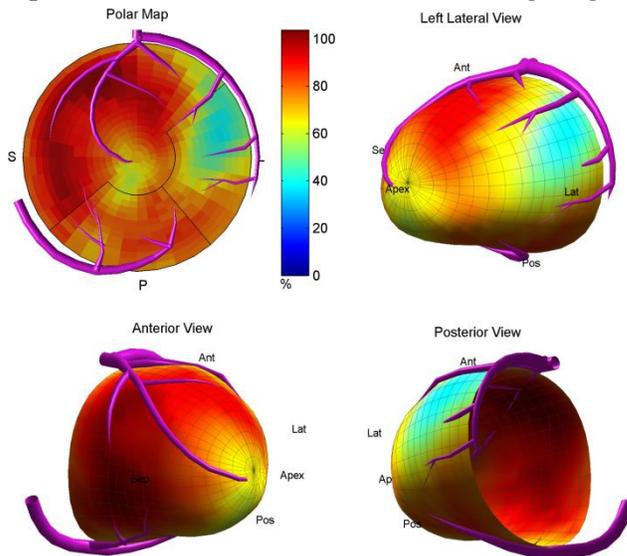
Figure 3-5 – Polar-map (top left) and 3D perspective views of the LV from different angles for the same case as in Figure 3-3C and Figure 3-4. Model coronary arteries are superimposed to relate polar-map regions to the three main vascular territories.
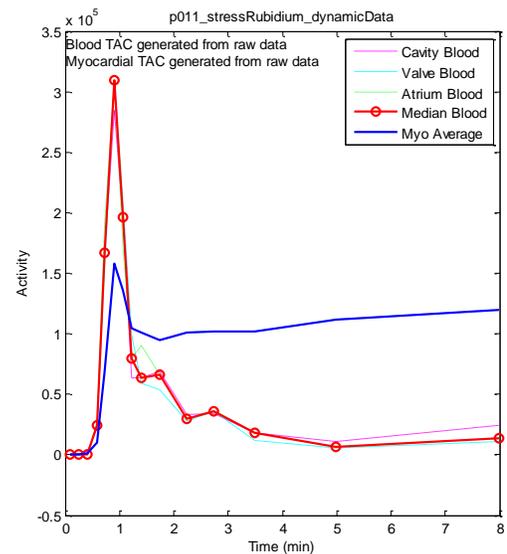
Figure 3-6 – Time-activity-curves (TAC) for blood in three regions and their median (thick red) as well as the mean TAC for the myocardium region (blue) for the same case as in Figure 3-3C. and Figure 3-4.

3.2.5.2 Kinetic Modeling

The last stage in the processing of each scan was to solve the parameters of a kinetic model, based on the blood (input) and myocardium (output) TAC functions. Each polar-map sector of the LV myocardium (apex to base plane) was optimized separately resulting in $36 \times 16 = 576$ sets of kinetic parameters.

The uptake rate of ^{82}Rb, K_1 mL/min/g, was quantified using a one-compartment constant distribution volume (DV) model [135] at both rest and stress states:

$$C_t(t) = K_1 e^{-\left(\frac{K_1}{DV}\right)t} \otimes C_a(t)$$

3-6

$C_t(t)$ represents the modeled tissue activity concentration, $C_a(t)$ is the measured arterial blood concentration as a function of time, t. In the DV model, DV is the ratio of the tissue and blood tracer concentrations when the compartments have reached a state of equilibrium. Since the net exchange of tracer is zero at equilibrium, DV can be expressed as:

$$DV = \frac{K_1}{k_2}$$

3-7

To further simplify the kinetic model, DV was set to a scan-specific, constant value determined by fitting the unconstrained model to the region of normal uptake in the polar-map.

K_1 was related to flow, *MBF* mL/min/g, through $K_1 = MBF \times E(MBF)$, where

$$E(MBF) = 1 - e^{-PS(MBF)/MBF}$$

3-8

E (MBF) is a model-specific extraction fraction that accounts for non-linear tracer extraction as a function of MBF and the effective permeability x surface-area product, *PS* mL/min/g [29,30]. This model is consistent with the observation that tracer extraction typically decreases with flow, despite the *PS* product increasing due to capillary recruitment. The following *PS* function was used, as determined previously in human subjects [39]:

$$PS(MBF) = 0.63 + 0.26 MBF$$

3-9

The measured myocardial image concentration in each polar-map sector, $C_m(t)$, was estimated according to:

$$C_{model}(t) = TBF \cdot C_a(t) + (1 - TBF)C_t(t)$$

3-10

where *TBF* was the estimated total blood volume and (1-*TBF*) corrected for regional recovery loss in the myocardium [64].

The example in Figure 3-7 shows a report for the kinetic modeling stage consisting of polar-maps of kinetic modeling parameters, K_1, k_2, and *TBF*. The *DV* estimate is included in the title. In addition, goodness–of-fit parameters (χ^2, R^2, the optimization convergence flag, and whether any of the parameters hit their upper bounds) are displayed in polar-map format to indicate regional reliability of the kinetic parameters. Finally, MBF (flow) and the uptake

polar-maps are shown. Regional correspondence between uptake and flow patterns is expected.

The blood TAC (red line) and the mean sampled myocardium TAC in the high-uptake (>75% of maximum) regions (blue dots) are shown in the bottom panel of the figure. The recovery corrected myocardial TAC, $C_t(t)$, (cyan) and modeled-determined TAC, $C_{model}(t)$, (blue line) are also included together with the sampled myocardial TAC, $C_{meas}(t)$, (blue dots). The error between sampled and modeled myocardium TACs (green) shows little error and no temporal pattern, also indicating a good fit. The model fits and TAC data can also be viewed for any polar map sector with an interactive cursor selection.
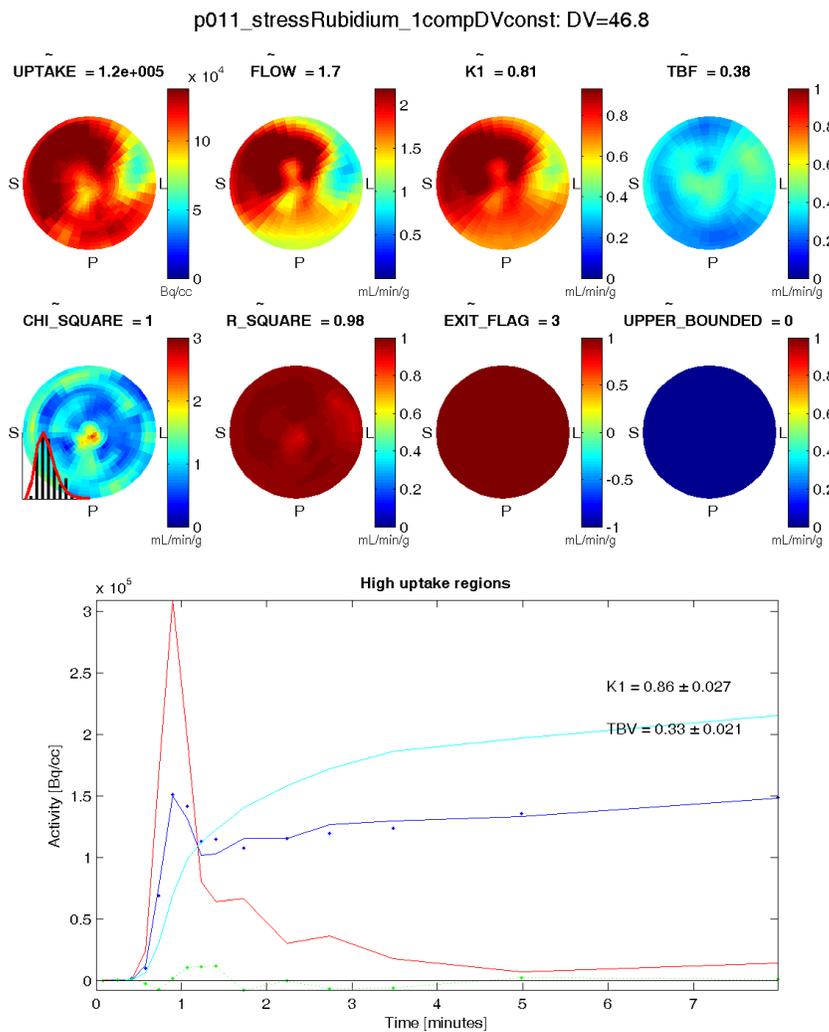
Figure 3-7 – Kinetic modeling report for the same case as in Figures 2-3 through 2-6.

3.2.6   Relative Uptake and MFR Analysis

The rest and stress scans were compared to analyze changes between states using the relative uptake and absolute flow polar-maps. Each report included rest, stress, stress/rest, and stress-rest polar-maps (corresponding to rest MBF, stress MBF, MFR, and ΔMBF for absolute flow), as demonstrated in Figure 3-8. The polar-maps were then segmented into the

three vascular territories [46] to produce regional average values. Global (LV mean) values were also calculated by averaging the same polar-maps over the entire LV.
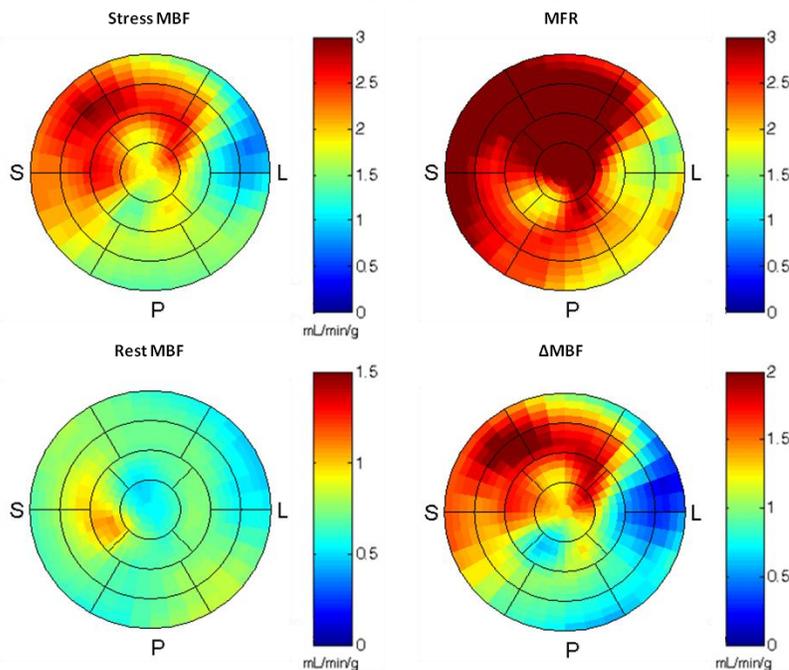
Figure 3-8 – MBF, MFR, and ΔMBF analysis report with the rest case shown in Figures 2-3 through 2-7 indicates uniform rest and stress flows with MFR≈3.1 and ΔMBF≈2.2 mL/min/g, which indicate normal MBF. This case was interpreted as normal using relative uptake images (not shown).

3.2.7   Inter- and Intra-Operator Variability

All patient images were anonymized and copied in random order to two datasets consisting of all 60 images. All scans were first processed automatically (with no operator intervention) from the orientation phase through to the kinetic modeling and MFR analysis.

The processed studies were then reviewed independently by each of two operators, one novice (operator 1) and one expert (operator 2). Thus each scan was processed twice by each of two operators. The novice operator had never used FlowQuant or any other software for quantifying cardiac function from images, while the expert operator had used FlowQuant for over 1 year to review and process hundreds of clinical studies. Both operators were instructed on use of the FlowQuant program and methods for quality assurance review of the automatically processed results, using a separate dataset which is not included in this work.

The operators reviewed the QA reports (Figures 2-3 − 2-8) saved during the reorientation, LV segmentation, and kinetic modeling steps, and reprocessed with manual intervention, any scan that was considered suboptimal. Thus, each scan was processed four times (twice by each operator). Specifically, processing was considered to be suboptimal in cases where: 1) the ellipse did not properly track the myocardium in the LV orientation phase; 2) the sampling points did not properly overlay the myocardium in the LV segmentation step due to the presence of adjacent organ activity ; 3) there was discordance between the TACs for the cavity, base and atrium blood regions; 4) there was discordance between the patterns of relative uptake and absolute MBF polar-maps in the kinetic modeling

phase; 5) the goodness-of-fit parameters indicated suboptimal fitting of the kinetic model to the measured data, i.e. non-uniform R^2, high χ^2 values, or a non-random distribution of the residuals.

The operators were instructed to correct these issues by first ensuring accurate ellipse placement during reprocessing, but intervening as little as possible. This could be accomplished by first changing the transaxial plane to choose an image with optimal contrast between the myocardium and the background and/or cropping the inferior slices to remove adjacent organ activity. The operator could also intervene on the subsequent VLA and HLA slices by properly resizing and repositioning the ellipse over the myocardium, if needed. In the LV segmentation phase the operator could adjust the spline control points to improve overlap of the model contour with the myocardium uptake.

The reprocessed datasets were analyzed for inter- and intra-operator variability in rest, stress, stress/rest and stress-rest both in relative uptake and absolute flow. The analysis was performed in the three vascular territories as well as globally. For intra-operator agreement the two datasets processed by each operator were compared with one another, and the results for each operator were reported separately. For inter-operator agreement, the repeated analyses were combined and then compared between operators.

3.2.8   Statistical Analysis

Agreement between paired datasets was visualized using correlation analysis and a linear regression fit. Pearson's correlation (r^2) was used to report agreement between datasets. Fisher's z-transform was used to calculate the probability of two r values being significantly different. In addition, a Bonferroni correction (n=6) was applied for multiple comparisons between operator and dataset combinations.

Differences between datasets were analyzed using Bland-Altman plots [136] and a reproducibility coefficient (RPC), calculated as 1.96 times the standard deviation of the differences. Thus 5% of the data points are expected to fall outside the range of mean ± RPC, assuming the differences follow a Gaussian distribution. RPC values were compared by conversion to variance ($\sigma=(RPC/1.96)^2$) and then applying an f-test with $p<0.05$ considered significant. In addition, the %RPC was reported as the ratio (%) of the mean rest, mean stress, mean stress/rest, and mean rest and stress for rest, stress, stress/rest, and stress-rest respectively. Likewise, biases were evaluated as the mean of differences between datasets and were reported as the ratio (%) of the bias scaled in the same way as %RPC.

Group mean and variance differences were evaluated using a two-sided student t-test and F-test respectively with Bonferroni correction (n=12) and $p<0.05$ considered significant.

3.3 Results

3.3.1 Patient Demographics

Patient demographics are summarized in Table 3-2. The youngest and oldest patients were 32 and 81 years of age respectively. The mean±sd global MBF, MFR, and ΔMBF are listed for all 4 datasets (2 operators × 2 repeated datasets). No significant differences in means or variance were found between or within operator's repeated datasets (p>0.05).

TABLE 3-2 – CHARACTERISTICS OF STUDY POPULATION (N=30)

Age	[yrs]	64.9±10.0			
Gender (Male)	[N (%)]	11 (37%)			
Normal*	[N (%)]	14 (47%)			
Single vessel disease*	[N (%)]	12 (40%)			
Multi-vessel disease*	[N (%)]	4 (13%)			
MBF (n=30)		Operator 1		Operator 2	
		Dataset 1	Dataset 2	Dataset 1	Dataset 2
Global rest MBF	[mL/min/g]	1.04±0.41	1.04±0.41	1.04±0.41	1.04±0.41
Global stress MBF	[mL/min/g]	2.24±0.92	2.25±0.92	2.25±0.92	2.25±0.92
Global MFR		2.40±1.20	2.40±1.08	2.41±1.21	2.43±1.21
Global ΔMBF	[mL/min/g]	1.20±0.80	1.21±0.79	1.21±0.80	1.22±0.80

* Based on interpretation of standard relative uptake MPI

p=NS for mean differences of all operator/analysis combinations

p=NS for standard-deviation differences of all operator/analysis combinations

3.3.2 Operator Intervention

Operator intervention at each processing stage is summarized in Table 3-3. The intervention of Operator 2 remained consistent between datasets when compared to operator 1. Both operators intervened primarily by cropping adjacent organ activity on the inferior image. Operator 1 cropped 18 images in the first analysis but only 6 in the second analysis, which was more similar to the interventions of operator 2. This suggests some improvement of processing skills as operator 1 gained experience with the software, with less intervention required in the second analysis.

TABLE 3-3 – NUMBER OF OPERATOR INTERVENTIONS PER DATASET (OUT OF 60 IMAGES)

Operator	Dataset	Gut	TV Plane	Position			Angle			Ellipse Size			Segmentation Stage
				TV	VLA	HLA	TV	VLA	HLA	TV	VLA	HLA	
1	1	18	4	0	0	0	0	0	0	0	0	0	5
	2	6	0	0	4	0	0	1	0	0	2	0	4
2	1	4	0	0	0	0	0	0	0	0	0	0	1
	2	4	0	0	2	0	0	0	0	0	1	0	1

TV – Transverse Plane

VLA – Vertical Long Axis Plane

HLA – Horizontal Long Axis Plane
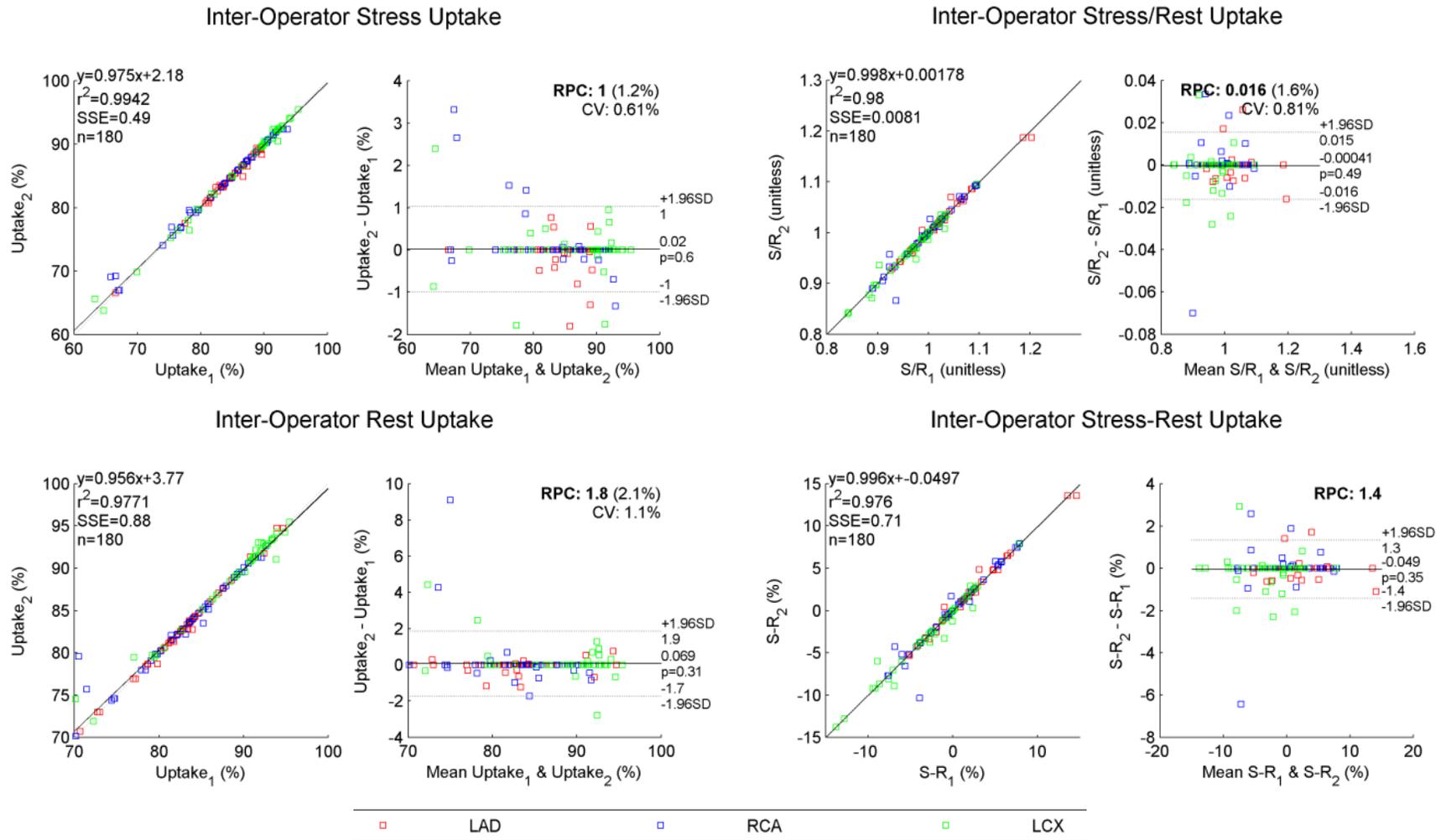
Figure 3-9 – Bland-Altman graphs for inter-operator agreement of rest uptake, stress uptake, stress/rest uptake, and stress-rest (datasets 1 and 2 combined).
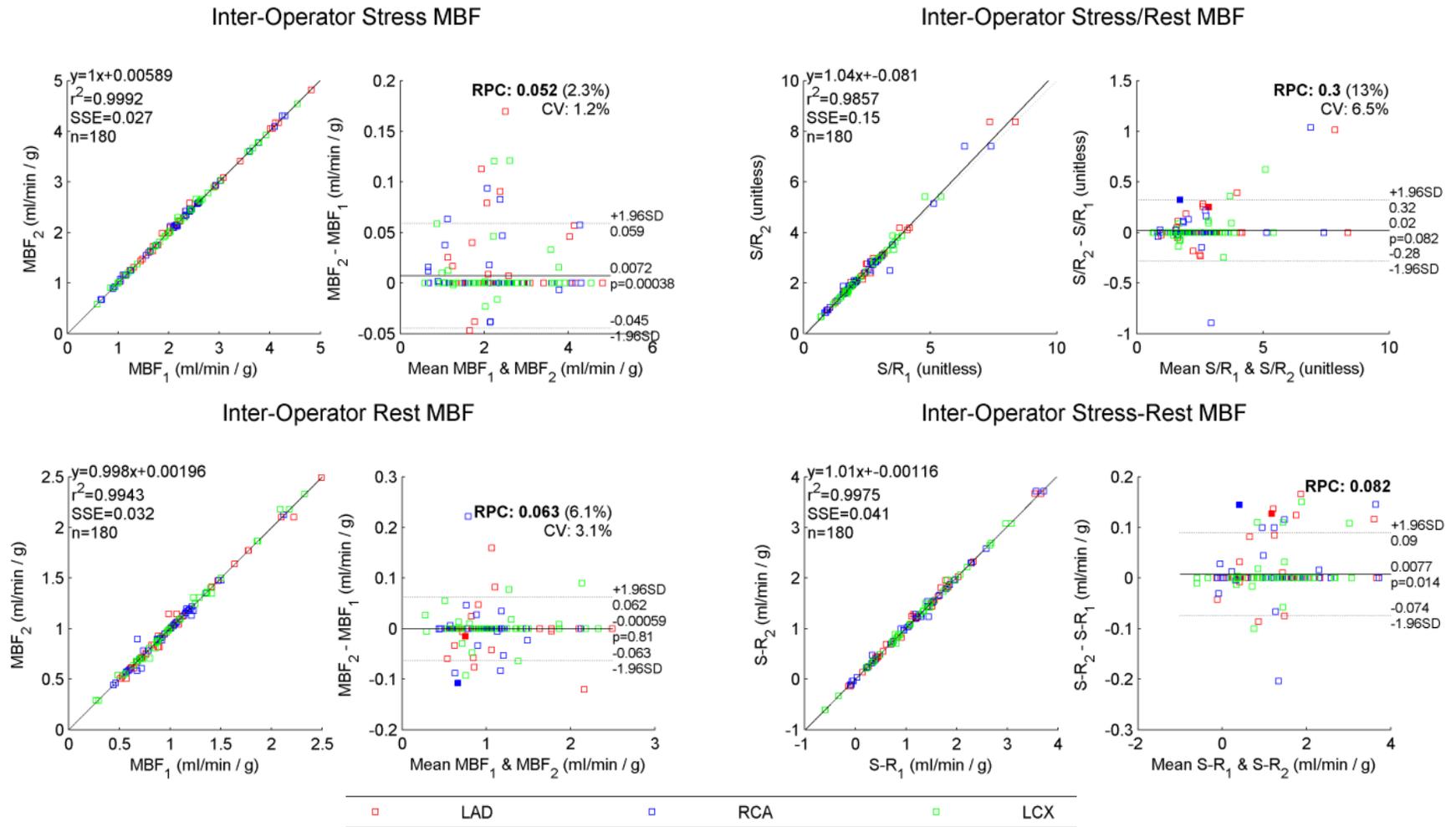
Figure 3-10 – Bland-Altman graphs for inter-operator agreement of MBF, stress/rest MBF, and stress-rest MBF (datasets 1 and 2 combined).

3.3.3   Inter-operator Variability

Relative uptake and absolute flow inter-operator analyses are shown in Figure 3-9 and Figure 3-10 respectively. Both figures contain correlation and Bland-Altman plots for rest (bottom left), stress (top left), stress/rest, (top right), and stress-rest (bottom right) using the data from the three vascular territories. Overall, excellent correlation, and low bias, was demonstrated both for relative uptake and absolute flow. In all cases the slope was close to unity (0.956-1.04) and the intercept was within ±5% of the mean values.

Bias(%), correlation (r^2), and RPC(%) values are summarized in Figure 3-11, Figure 3-12, and Figure 3-13 respectively. While, relative uptake appears to have lower bias than absolute flow, none of the bias values differed significantly from zero (p=ns). All inter-operator correlations were higher for absolute flow compared to relative uptake, but were significant only in the case of rest and stress-rest (p<0.05). Finally, the reproducibility coefficients for relative uptake, were all lower (more reproducible) than for absolute flow (p<0.001).
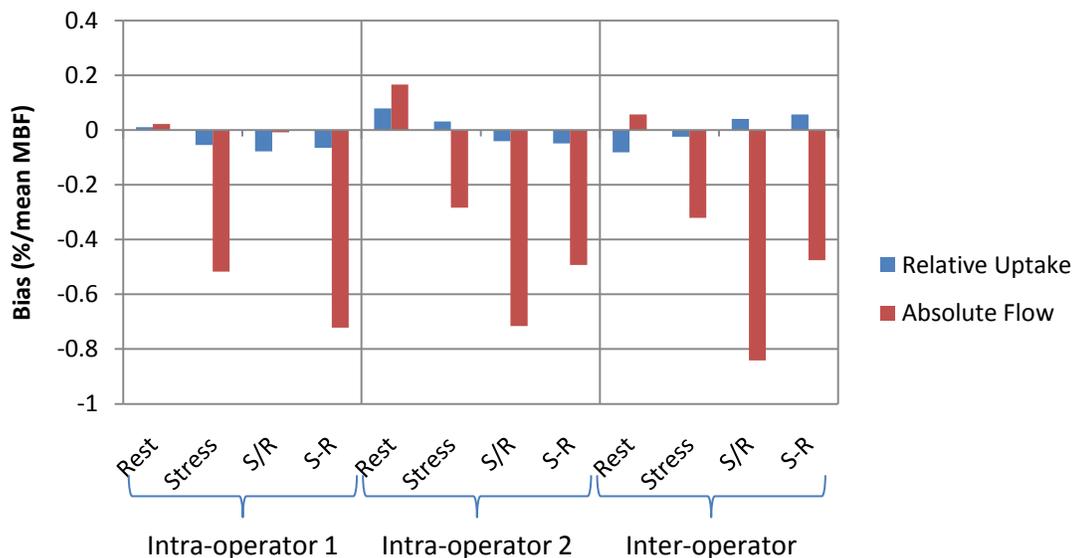
Figure 3-11 – Biases in intra- and inter-operator agreement of relative uptake and absolute flow. All biases were not significantly different from zero (p>0.05) and remained below 1%.
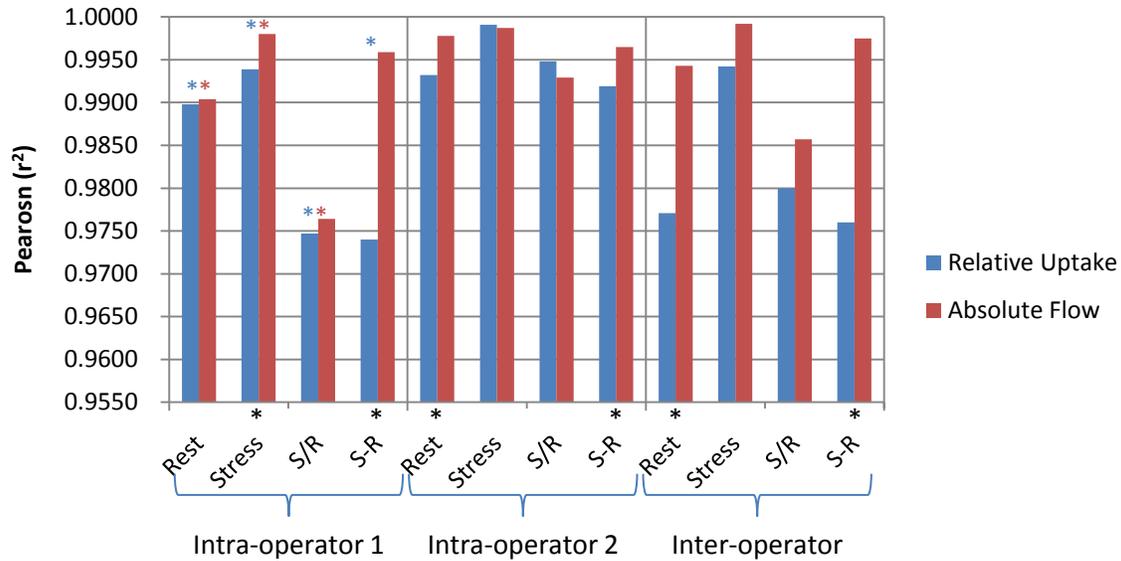
Figure 3-12 – Biases in intra- and inter-operator agreement of relative uptake and absolute flow. All biases were not significantly different from zero (p>0.05) and remained below 1%.
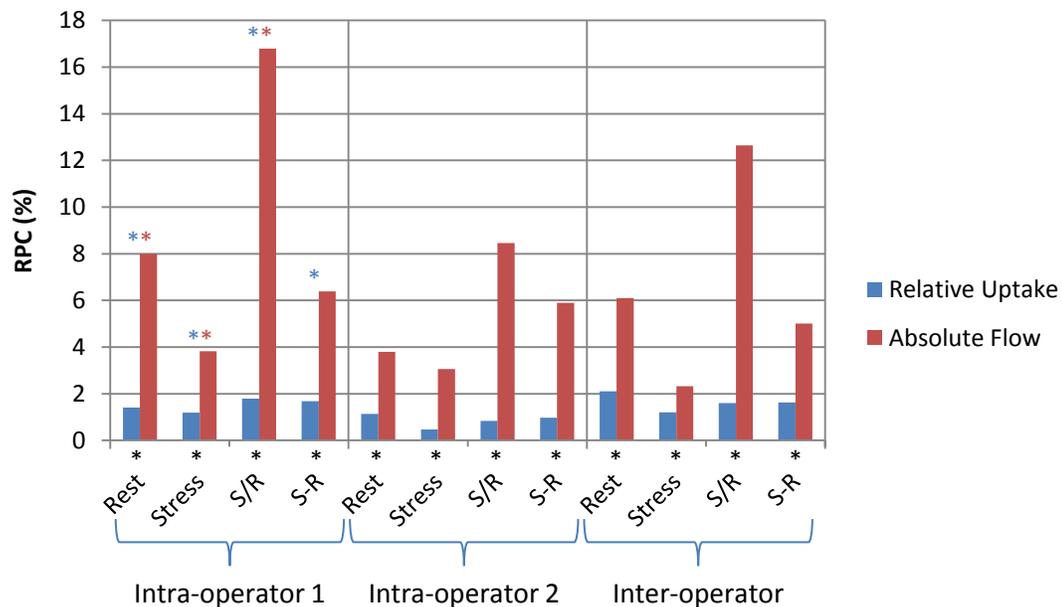
Figure 3-13 – RPC for intra- and inter-operator differences of relative uptake and absolute flow. In all cases relative uptake analysis is less variable than absolute flow (p<0.001) (black *). Generally, operator 2 (experienced) had less variability than operator 1 (novice) for relative uptake (blue *) and absolute flow (red *).

3.3.4   Intra-Operator Variability

Intra-operator biases were also larger with absolute flow compared to relative flow (p<0.001). None of the biases were significantly different from zero (p=ns) as with the inter-operator biases. In all cases correlation was excellent ($r^2 \geq 0.97$).

Generally, intra-operator 2 (expert) had significantly higher correlations (p<0.001) and lower RPC% (p<0.001) for rest, stress, and stress/rest than intra-operator 1 (novice), as shown in Figure 3-12 and Figure 3-13 respectively. Interestingly, only absolute flow stress-rest correlation (p=0.6) and RPC% (p=0.4) did not differ significantly between operators. These results suggest slightly better intra-operator reproducibility with experience, and that absolute stress-rest may be more robust against operator-dependent variability.

3.3.5   Regional Variability

The inter- and intra-operator RPC% for absolute flow values (combined rest and stress) in the three vascular territories and globally are listed in Table 3-4. RPC in absolute units is also presented as 95% confidence intervals that could be used in serial comparisons accounting for operator variability. The results suggest that the LCX region may be less sensitive to operator interaction than the LAD and RCA regions, but the general agreement remains very good, with 95% of disagreements still below 6.1% (0.095 mL/min/g) in the territory with largest variation for intra-operator 1.

TABLE 3-4 – REGIONAL AND GLOBAL RPC FOR INTER- AND INTRA-OPERATOR AGREEMENT OF ABSOLUTE FLOW

	Absolute (mL/min/g)			% (of mean MBF)		
	Intra-operator 1	Intra-operator 2	Inter-operator	Intra-operator 1	Intra-operator 2	Inter-operator
LAD	0.080	0.076	0.065	4.80%	4.52%	3.90%
RCA	0.095	0.049	0.061	6.08%	3.11%	3.88%
LCX	0.075	0.038	0.048	4.51%	2.29%	2.86%
Global	0.068	0.053	0.050	4.13%	3.22%	3.06%

3.4 Discussion

In this chapter we assessed the inter- and intra-operator variability of relative uptake and absolute flow measurements assessed at rest, stress, stress/rest, and stress-rest using the FlowQuant software program with two operators and two identical, anonymized, and randomized sets of images. Operator 2 was an experienced user whereas operator 1 was a novice. Operator 1 was trained on a small, separate set of images and was then left to process the data independently. By measuring the variability with expert and novice users the range of operator variability is defined.

It is possible that the difference in user interactions (Table 3-3) between datasets 1 and 2 corresponds to operator 1's learning curve. As experience was gained by the operator, less intervention was required. Thus operators 1 and 2 form a worst and best case scenario respectively. While the intra-operator agreement of operator 1 remained consistently lower than that of operator 2, both the inter- and intra-operator metrics illustrated excellent agreement.
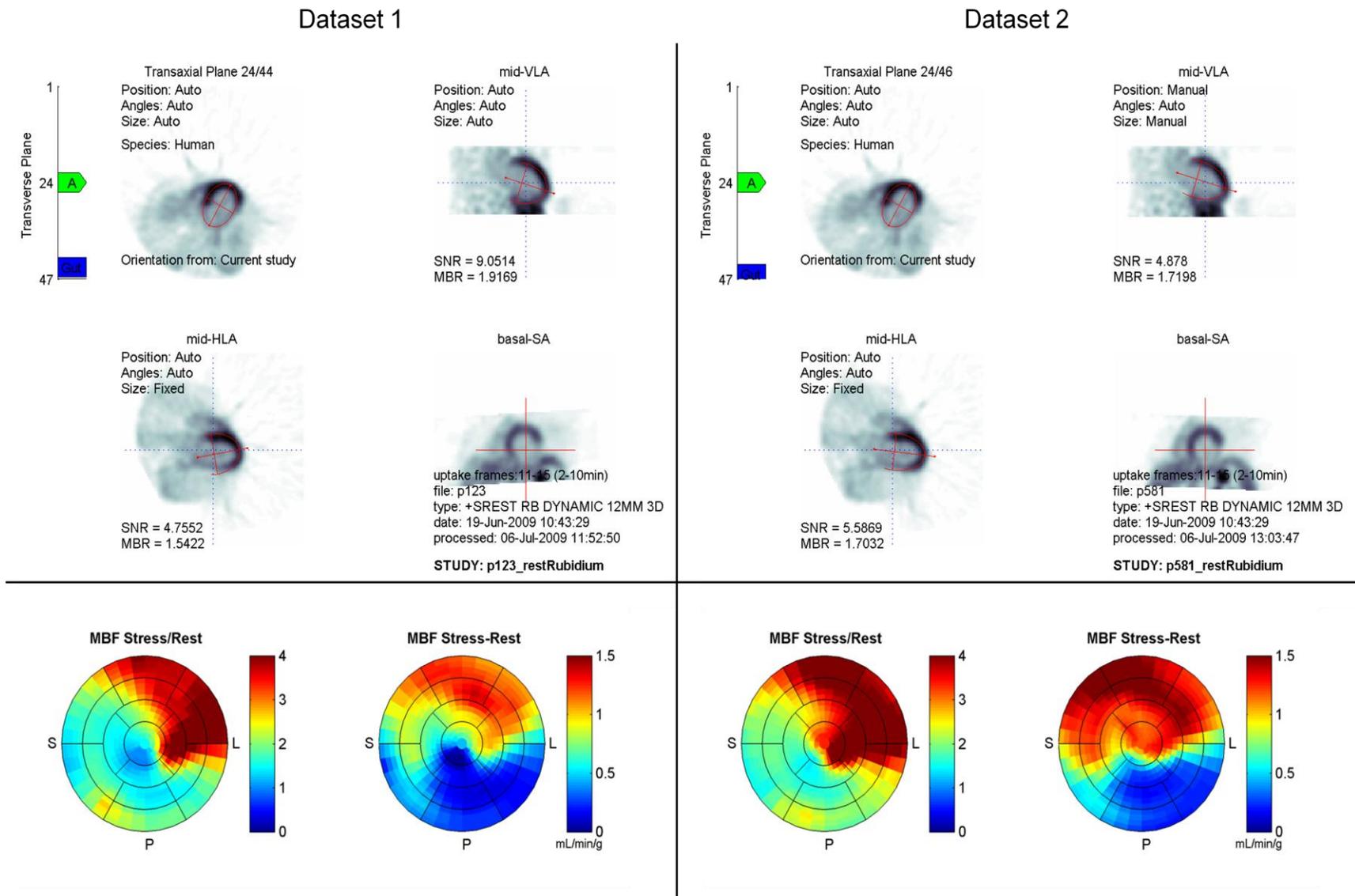
Figure 3-14 – Example of analysis with the largest MBF discordance (intra-operator and inter-operator) demonstrating that the operator failed to correct for suboptimal detection of the LV in the mid-VLA (left) but did intervene in the second dataset (right). Similar orientations were copied to stress without further intervention. Consequently, the stress/rest and stress-rest maps differed mainly in scale, but less in spatial distribution.

One patient scan, with the largest intra-operator discordance in MBF values, is shown in Figure 3-14. In this rest scan the operator neglected to intervene during reorientation in dataset 1 (left), but did intervene in the dataset 2 (right), resulting in an improved fit of the ellipse in the mid-VLA and mid-HLA slices. The MBF differences were in the inferior wall and the apex, corresponding to the RCA and LAD territories. The RCA and LAD data points associated with the dataset 1 are shown in the inter-operator rest, stress/rest, and stress-rest Bland-Altman plots in Figure 3-10 using filled blocks. In a clinical setting, it is expected that this type of registration error should be identified as part of the QA process and that the image would not be interpreted until reprocessed. The importance of the saved graphical reports and their routine review is thus emphasized.

3.4.1   Comparison to other repeatability studies

Previous studies have evaluated intra- and inter-operator variability of MBF and MFR with other software programs. The results of some of these studies are listed in Table 3-5 alongside the results of this study. While the methodology of each study is slightly different, it is reassuring that the method presented here performs similarly or better in most cases. The work of El Fahkri *et al*. [72] used the average across 4 datasets per operator to measure inter-operator variability. Reproducibility across averages is expected to result in higher correlations and lower RPC compared with the standard methodology used in the present study. Comparison of correlations is further complicated since inter and intra-operator correlation coefficients varied considerably. In addition, some of the correlations were reported using a Spearman non-parametric correlation coefficient (ρ) and some were reported using a Pearson correlation coefficient (as performed in this study) which is more sensitive to outliers.

The work of Knešaurek at al. [53] used the PMOD software, which requires manual operator interaction, and may explain the increased operator variability. It is not clear in this paper if both sets of data were processed by the same operator or two different operators (the former is assumed).

Schindler *et al.* [89] measured inter-operator agreement at rest, CPT, and stress. While the rest and stress results are included in Table 3-5, the CPT results (r^2=0.61, RPC=26%) were excluded for simplicity. In addition, while Schindler *et al.* make reference to intra-operator variability, these were performed on separate, repeat scans, and thus include variability resulting from changes in the subject between scans, as well as variability in the imaging process. In Sawada *et al.* [85] and El Fakhri *et al.* [72] repeat measurement agreements were also reported, and referred to as inter-study variability and reproducibility respectively.

Nestrov *et al*. [71] measured inter- and intra-operator variability at rest and stress in 10 patients using 4 operators with various degrees of experience. Each operator processed the data twice at two-week intervals. Analysis included global, 4 coronary artery territories

(apex was isolated from the LAD territory), and 17 segments. Variability increased with the number of segments (inverse to ROI sizes) likely due to increases in noise and physiological MBF heterogeneity [137,138]. Since the segmental and regional analysis was performed using interclass correlation coefficients, direct comparison of with Pearson correlation coefficients was not possible. However, comparison of RPC% values was possible, and showed less variability with the proposed method.

TABLE 3-5 – MBF AND MFR INTRA- AND INTER-OPERATOR CORRELATIONS AND RPC% IN DIFFERENT STUDIES

	Klein *et al.* (Present study)	El Fakhri *et al.* [72][‡]	Knešaurek *et al.* [53]	Schindler *et al.* [89]	Sawada *et al.* [85]א	Adachi *et al.* [90]	Nesterov *et al.* [71]
Software Program	FlowQuant	GFADS	PMOD	n.a.	n.a.	n.a	Carimas™
Radiotracer	[82]Rb	[82]Rb	[82]Rb	^{13}N-ammonia	^{13}N-ammonia	^{15}O-water	^{15}O-water
N	30	22	12	20	12	23	10
Population	Patients	Mixed	Normals	Mixed	Mixed	Normals	Patients
Myocardium Segments	3	3	16	1	5	16	4
Inter-operator Correlation (r[2])							
Rest MBF	0.994	0.827<ρ<0.935	n.a.	0.92	0.99	n.a.	n.a.
Stress MBF	0.999		n.a.	0.76		n.a.	n.a.
MFR	0.986		n.a.	n.a.	0.97	n.a.	n.a.
Intra-operator Correlation (r[2])							
Rest MBF	0.990-0.998	0.99	n.a.	n.a.	n.a.	0.712	≤0.986
Stress MBF	0.998-0.999		n.a.	n.a.	n.a.		
MFR	0.976-0.993	0.97	0.98	n.a.	n.a.	n.a.	n.a.
Inter-operator Reproducibility (RPC%)							
Rest MBF	6.1%	n.a.	n.a.	12.0%	~9%	n.a.	<15%
Stress MBF	2.3%	n.a.	n.a.	28.1%	~13%	n.a.	<15%
MFR	12.6%	n.a.	n.a.	n.a.	~27%	n.a.	n.a.
Intra-operator Reproducibility (RPC%)							
Rest MBF	3.7-8.0%	1.7 %	8.5 %	n.a.	n.a.	~73%	<50%
Stress MBF	3.0-3.8%	1.4 %	6.3 %	n.a.	n.a.		<20%
MFR	8.5-16.8%	2.8 %	10.6 %	n.a.	n.a.	n.a.	n.a.

n.a. – not available

r –Pearson correlation

ρ –Spearman correlation

‡ – means of 4 repeat results for each operator

א – Estimated from reported results

The operator-dependent variability in this study is similar or lower than previously published methods, even when including the results of a novice operator. Thus the results suggest that a highly automated approach with minimal operator intervention is robust against operator induced variability.

3.4.2   Relative Uptake vs. Absolute Flow

The results demonstrated better reproducibility of relative uptake through lower biases and lower RPC compared to absolute uptake, while correlation tended to be better with absolute flow compared to relative uptake. The lower biases and RPC are due to 1) normalization of the relative uptake to a common scale and 2) avoidance of small rest values which amplify variation in stress/rest values. Thus, the improved robustness of relative uptake comes at the expense of sensitivity to physiological global changes in blood flow as previously demonstrated [42].

3.4.3   Stress/Rest vs. Stress-Rest Differences

When using absolute flow, reproducibility of stress/rest was significantly worse than stress-rest as indicated by lower r^2 (p<0.02 for intra-operator 2, and p<0.001 for intra-operator 1 and inter-operator) and higher RPC values (p<0.001 for intra-operator 1, intra-operator 2, and inter-operator) as shown in Figure 3-12 and Figure 3-13 respectively. The reduced reproducibility of stress/rest is due to the higher sensitivity of the ratio to changes in low resting flow values, to which the subtraction operation in stress-rest is more robust. Thus, stress-rest measurements appear to be more reproducible than stress/rest, and therefore may be more sensitive to monitor serial changes. Both the stress-rest difference and ratio reflect the vasodilatory capacity to increase flow over baseline conditions. However, our results suggest that stress-rest is expected to be more robust, particularly in regions of infarction where low resting flow values may cause the stress/rest to appear artificially elevated.

When using relative uptake, a systematic difference between reproducibility of stress/rest and stress-rest was not observed. This is explained by the removal of small rest values through normalization of the rest (and stress) images.

3.4.4   Limitation

This study is limited by having two operators and two datasets each. Furthermore, a single operator represented novices and a single operator represented experts. However, two operators at opposite ends of the spectrum of experience are expected to bound the actual operator variability that will be experienced in the majority of operator groups.

This work has not characterized the accuracy or test-retest reproducibility of this method in quantifying MBF, MFR, or ΔMBF, although previous studies addressed [82]Rb quantification accuracy [39] and diagnostic accuracy in 3-vessel disease [42].

3.5 Conclusion

The FlowQuant software program has been developed for reproducible quantification of myocardial blood flow and myocardial flow reserve using [82]Rb PET in routine clinical practice and in research. Excellent intra- and inter-operator variability was observed both for

absolute flow quantification and for relative uptake analysis between both novice and expert operators. However, better reproducibility was measured in the expert operator. To minimize variability, new operators should be trained using a small set of suitable cases and their performance should be tracked during the learning phase.

Chapter 4.

Overlap Constrained Factor Analysis of Dynamic Cardiac ^{82}Rb PET Images

The contents of this chapter have been presented at the IEEE-Medical Imaging Conference in Honolulu, Hawaii 2007 [139]. Ran Klein was the primary author. The chapter consists of the published manuscript in its entirety and demonstrates the importance of selecting physiologically accurate constraints during image decomposition. A detailed description of the methodology used to resolve the number of components was appended in the beginning of the methods section.

4.1 Background

The success of FADS in resolving physiologically accurate blood input functions has been demonstrated in canine with ^{13}N-ammonia and in humans with ^{18}F-FDG, but has failed in smaller subjects such as small monkeys and paediatrics [110]. It is understood that FADS may succeed when pure pixels exist in the image, but under this assumption FADS has limited application.

A major limitation of factor analysis is non-uniqueness of the solution, even when non-negativity is imposed [140,141,142]. In the mid 1980s ambiguity of FADS solutions was addressed by constraining one of the factors to the time-activity profile of the image background in a method referred to as image based FADS [143]. This approach was limited to resolving factors of isolated organs. Application of maximum entropy as an additional constraint was shown to somewhat improve correspondence of factors with simulated data, and was only validated in canine models using ROI derived curves [144]. ROI derived curves are a poor standard for validation of factors as the whole premise of image decomposition is to overcome the limitations of ROI derived curves. A priori information on the mixing of cardiac tissues was also investigated [108] and in simulations showed improved accuracy of blood factors, but not of myocardium factors. Once again, experimental validation in canines was limited to ROI defined curves.

Instead of addressing the physiology directly, some have attempted to constrain the solution based on the imaging process or image properties. For example, a spatial regularization of FAMIS has been implemented by enforcing uniformity between neighbouring pixels [123]. These results were validated with simulations [123] and later applied to myocardial perfusion reserve in ^{15}O-water imaging [79].

Recently, minimal structure overlap, also referred to as minimal spatial overlap (MSO), has been proposed as an alternative constraint [106,124]. While the MSO approach

may seem intuitive at first, it does violate some knowledge of the nature of the images and of the cardiac anatomy. Arterial blood and myocardial tissue signals overlap in the myocardial region due to the heart muscle being perfused by arterial blood which accounts for as much as 20% of the volume in this region [49,108]. In addition the blurry nature of the images as well as incomplete scatter correction introduces spillover (or cross contamination) of blood and myocardium. Validation of MSO has been limited to simulation and MBF quantification in 8 rest-stress studies [106].

This section explores a new constraint that penalizes against temporal overlap of the factors. The proposed method resolves ambiguity of the solution by producing factors that are as temporally distinct as possible without violating the non-negativity constraints. The method is compared with the MSO constraint and the results are evaluated using simulation and experimental results.

4.2 Methods and Materials

4.2.1 Number of Components

The number of components, K, was determined automatically based on the cumulative variance. The K-dependent cumulative variance was calculated using Eigenvalues of the image co-variance matrix which were normalized, sorted, and cumulated. The cumulative variance (y-axis) may be plotted against the normalized number of time frames (x-axis) as shown with black dots in Figure 4-1. Typically, K is determined by thresholding the variance as demonstrated by the blue line in Figure 4-1 and as described in section 2.9.2. To mitigate an excessively large number of components in the case of noisy images a penalty was included by selecting the point with the shortest Euclidean distance to the point (0,1) as demonstrated by the red dots. The number of frames corresponding to the selected dot was used as the number of components, K.
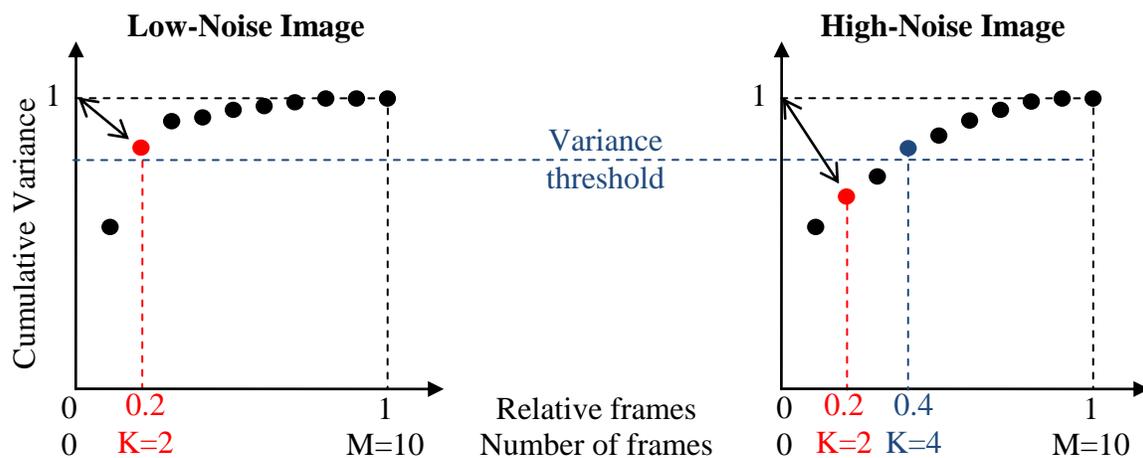
Figure 4-1 – Demonstration of two alternative methods for resolving number of factors, K, base on the cumulative variance in the image.

In a hypothetical low-noise image (Figure 4-1 left) both methods resolve two factors. In a hypothetical image with high random noise (right) the threshold method resolves 4 factors as the cumulative variance increases gradually with more factors while the proposed method maintains 2 factors.

4.2.2   Factor Analysis Algorithms

Dynamic sequence of images were decomposed using FADS [121], as described in section 2.8.4.1, resulting in non-negative factors and structure (**F**' and **S**' respectively). In a subsequent processing stage an additional constraint was introduced in order to resolve non-uniqueness, while maintaining the non-negativity of the rotated factors and structures. Two different constraints were implemented by optimizing the rotation matrix, **R**, so as to minimize the following penalty functions

$$f_{tot}^{MSO}(\boldsymbol{R}|\boldsymbol{F}',\boldsymbol{S}') = f_{neg}(\boldsymbol{F}'\boldsymbol{R}) + f_{neg}(\boldsymbol{R}^{-1}\boldsymbol{S}') + 0.01 f_{ovl}(\boldsymbol{R}^{-1}\boldsymbol{S}') \qquad \text{4-1}$$

$$f_{tot}^{MFO}(\boldsymbol{R}|\boldsymbol{F}',\boldsymbol{S}') = f_{neg}(\boldsymbol{F}'\boldsymbol{R}) + f_{neg}(\boldsymbol{R}^{-1}\boldsymbol{S}') + 0.01 f_{ovl}((\boldsymbol{F}'\boldsymbol{R})^{T}) \qquad \text{4-2}$$

The first two elements in the penalty functions penalize for negative values in the rotated factors ($\boldsymbol{F}=\boldsymbol{F}'\boldsymbol{R}$) and rotated structures ($\boldsymbol{S}=\boldsymbol{R}^{-1}\boldsymbol{S}'$). The negativity penalty, $f_{neg}(\boldsymbol{X})$, was defined by the magnitude of the negative elements in $\boldsymbol{X}$ relative to the magnitude of all the elements in matrix $\boldsymbol{X}$ as described in equation 4-3 and 4-4.

$$f_{neg}(\boldsymbol{X}) = \frac{|\boldsymbol{H}(\boldsymbol{X})|}{|\boldsymbol{X}|} = \frac{1}{|\boldsymbol{X}|}\sqrt{\sum_i \sum_j H(x_{i,j})} \qquad \text{4-3}$$

$$H(x) = \begin{cases} x^2, & x < \epsilon \\ 0, & x \geq \epsilon \end{cases} \qquad \text{4-4}$$

The third element of the penalty functions penalized for overlap between the rows of the input matrix $\boldsymbol{X}$ [106] as shown in equation 4-5. Thus by substituting the arguments with the rotated structures or rotated factors, MSO minimizes spatial overlap between structures, and MFO minimizes temporal overlap between factors.

$$f_{ovl}(\boldsymbol{X}) = \sum_{p=1}^{K} \sum_{q=p+1}^{K} \sum_{i=1}^{P} \frac{|x_{ip}|}{\sqrt{\sum_{j=1}^{N} x_{jp}^2}} \frac{|x_{ip}|}{\sqrt{\sum_{j=1}^{N} x_{jq}^2}} \qquad \text{4-5}$$

4.2.3   Simulated Dynamic Image Sequences

A dynamic image sequence containing two components (shown in Figure 4-2) was simulated. The first region was a centered circle containing 100% blood. The second region was a centered ring containing 85% myocardium and 15% blood factors. 10% Gaussian

noise was added to each time frame and was then smoothed with a 12mm FWHM Gaussian filter. The resulting image sequence (ignoring noise) is a series of linear combinations (defined by the factors) of the structures shown in the top-most row (Simulation) of Figure 4-3.
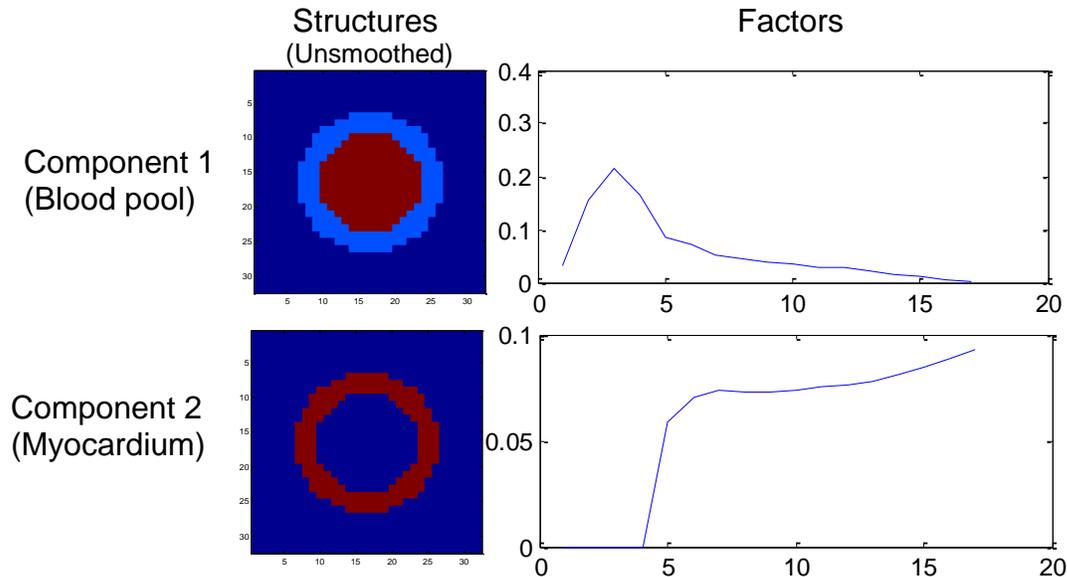
Figure 4-2 – Structures and corresponding factors used to create a simulated dynamic sequence of images.

The simulated image sequence was submitted for decomposition with FADS both with MSO and with MFO constraints. The factors and structures obtained using both constraints were validated against the known results of the simulated data using percent root-mean-squared error and using correlation (r^2) respectively.

4.2.4   Experimental Image Sequences

A single dog underwent a series of dynamic PET scans with varying ^{82}Rb (150 MBq) infusion intervals (15, 30, 60, 120, 240, 240, 120, 60, 30, 15 seconds) with a Siemens ECAT ART scanner. The images were iteratively reconstructed using OSEM with a 12 mm resolution. The reconstructed dynamic image sequence was 10 min long and contained 17 time frames (12×10s, 2×30s, 1×60s, 1×120s, and 1×240s). The images were corrected for radioactive decay.

Since the structures are representative of the anatomy of the subject they are expected to remain constant regardless of the tracer infusion duration. Robustness of the resolved structures against variability with infusion duration was measured using cross-correlation between the structures obtained from all 10 images.

Factors, on the other hand, are expected to reflect the variation in infusion duration. Blood factors are expected to rise from time zero until the end of the infusion and then decrease to near zero activity, as suggested in [45]. The relative decrease from peak activity

to the activity in the final frame was defined as blood clearance, where 100% clearance refers to a drop to zero activity in the final frame and 0% clearance refers to no drop from peak activity. Myocardium factors are expected to increase monotonically past the blood peak and then plateau during the final uptake time frames, consistent with the retention of rubidium in the myocardium.

Contrast between blood pool and myocardium was measured in the myocardium structures using an automated registration algorithm [134]. The algorithm automatically reoriented the myocardium structure to the LV reference frame and then registered the LV by optimizing a spline model of a partial ellipsoid. A fixed size blood pool region of interest was automatically defined in the center of the LV cavity. Contrast was defined as the difference between the mean LV and mean blood intensities relative to the mean LV intensity.

4.3 Results

4.3.1 Simulated Dynamic Image Sequences

The simulated structures were nearly exactly recovered using the MFO method, but not with the MSO method. The MSO derived blood structure was smaller compared to the simulated structure, while the MFO derived blood structure agreed closely with the simulation as shown in the left column of Figure 4-3. The measured error was greater with MSO (RMSE=24%) than with MFO (RMSE= 9%) indicating improved accuracy with MFO.
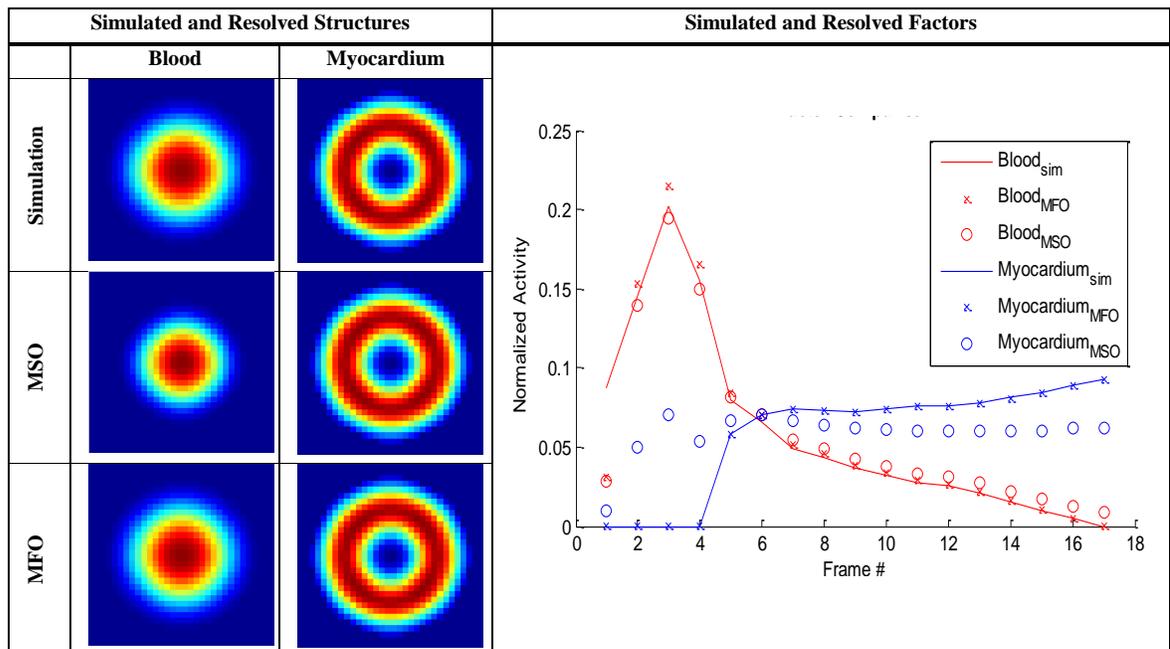
Figure 4-3 – Comparison of resolved blood (red) and myocardium (blue) factors using MFO (x) MSO (o) to the source profiles (lines) used in simulating the dynamic image sequence.

The graph on the right of Figure 4-3 compares the MSO and MFO derived factors with the simulated factors. The blood factors obtained with both MSO and MFO follow the simulated data closely, although MFO appears slightly more accurate (r^2=0.943) than MSO (r^2=0.927). While the MFO obtained myocardium factor follows the simulated data closely (r^2>0.999), the MSO factor does not (r^2=0.247). Most of the error in the MSO myocardium factor occurred in the early time frames, in the form of a local peak associated with blood signal spillover.

4.3.2   Canine Model

All ten images were decomposed into two factors (automatically determined), which accounted for 77-91% of the image variance. Similarly shaped factors were obtained with both MSO and MFO constraints as demonstrated in Figure 4-4. The factors were automatically labelled (and verified) as blood (combined LV and RV) and myocardium.

The myocardium factors obtained with MSO consistently exhibited a larger local peak synchronized with the blood factor peak (insert in top of Figure 4-4), suggesting that the myocardium factor was slightly biased with blood signal.
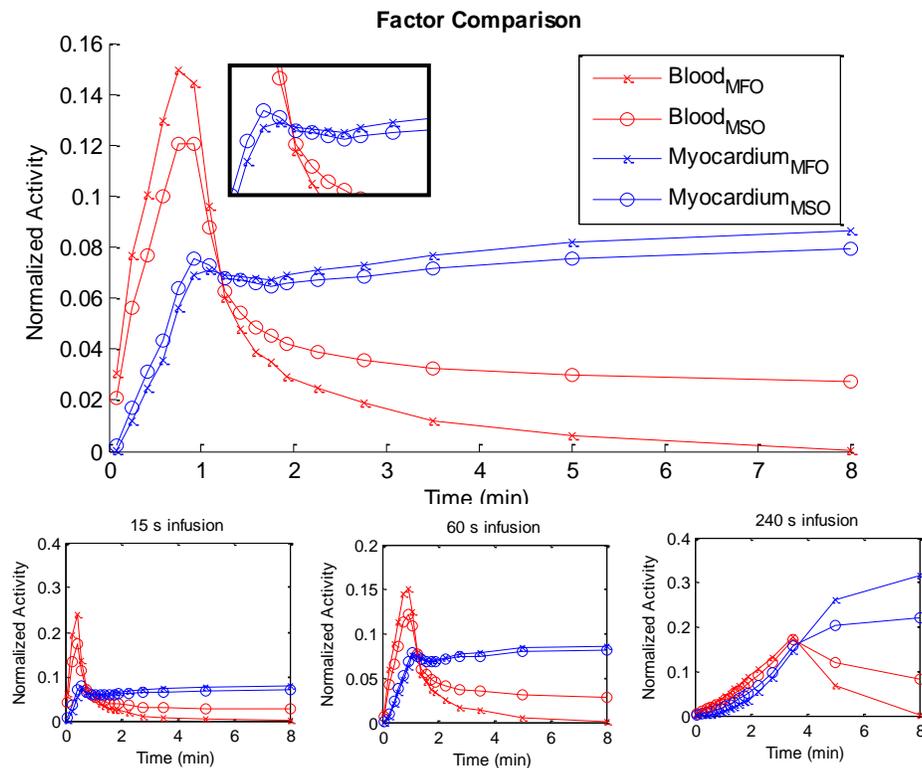
Figure 4-4 – (TOP) Example of comparison of resolved blood (red) and myocardium (blue) factors using MFO (x) and MSO (o) in a dog with a 30 second constant activity rate [82]Rb infusion. The insert emphasizes the local peak in the myocardium factors, which is associated with blood signal contamination. (BOTTOM) MSO and MFO factors with 15, 60, and 240 s infusion durations reflect the infusion duration in the broader blood peaks and more gradual uptake by the myocardium.

The blood factors obtained with the MFO constraint exhibited ~100% blood clearance (near zero activity in the last time frame) in all cases. Blood clearance in MSO blood factors was 60-85%, depending on the infusion interval (Table 4-1). Incomplete blood clearance with MSO is inconsistent with experimental observations [45] and may indicate that the blood factor is biased with myocardium signal.

TABLE 4-1 – BLOOD CLEARANCE

(MEAN OF TWO STUDIES FOR EACH ELUTION DURATION)

Elution duration	MSO	MFO
15 s	84 %	100 %
30 s	80 %	100 %
60 s	76 %	100 %
120 s	65 %	100 %
240 s	60 %	100 %

The structures obtained both with MSO and MFO had similar patterns, as demonstrate in Figure 4-5 for the extreme cases of 15s and 240s elution durations. The MFO blood structure is more dilated than MSO resulting in increased overlap between the blood and myocardium structures. In addition, MFO myocardium structures appear to be thinner in the apex region compared to MSO.
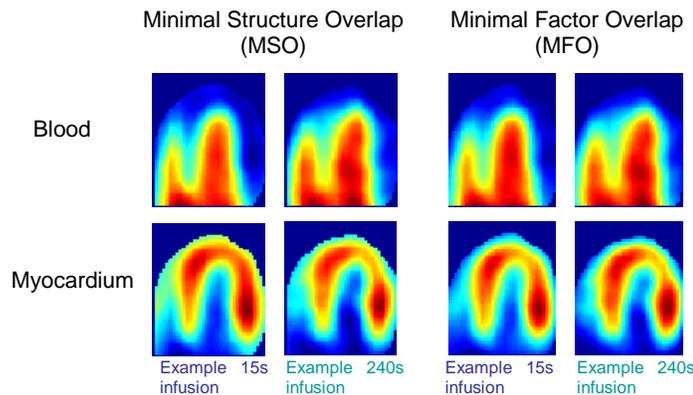
Figure 4-5 – Comparison of structures obtained using both MSO and MFO constraints at extreme elution intervals. Both constraints provide similar structures regardless of the elution duration, indicating robustness of both algorithms. The blood pool image obtained with MFO is consistently more dilated than that obtained with MSO. MSO provides myocardial structures with higher myocardium to blood pool contrast.

Excellent correlation (r^2>0.95) between structures was reported for all infusion times, when the same constraint was used, indicating that the results are highly reproducible with both MSO and MFO constraints. But the constraints do give different results as indicated by lower correlation between structures derived using the different constraints (0.75<r^2<0.87).

Contrast between blood pool cavity and myocardium (red and blue region respectively in Figure 4-6) in the myocardial structures was consistently greater with MSO as demonstrated in Table 4-2. These results are consistent with the MSO constraint which maximizes the spatial separation between factors.

MSO   MFO
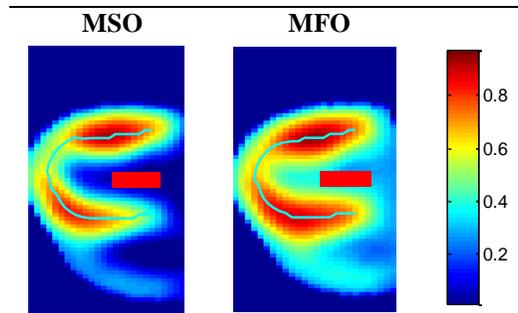
Figure 4-6 – Example of regions used to calculate contrast in myocardium structures. Red blocks show the blood pool region and the blue lines show the myocardium contour. MSO consistently produces higher contrast images than MFO.

TABLE 4-2 – MYOCARDIUM CONTRAST (MEAN OF TWO STUDIES FOR EACH ELUTION DURATION)

Elution duration	MSO	MFO
15 s	0.94	0.53
30 s	0.95	0.54
60 s	0.91	0.52
120 s	0.94	0.57
240 s	0.88	0.56
Mean ± SD	0.92 ± 0.05	0.55 ± 0.04

4.4 Discussion

In this work dynamic image sequences were decomposed using FADS and then applied additional constraints to resolve the ambiguity of the solution. The noise or residue in the image was removed by FADS as part of the decomposition. In all cases the images were decomposed into two factors. Visual inspection of the residue did not reveal any persistent temporal patterns. In addition, the residue was nearly equal in all time frames and was one to two orders of magnitude weaker than the image signal, indicating that the residue consisted primarily of noise.

The dynamic sequence of residue images, demonstrated in Figure 4-7, for 15 s and 240 s infusion intervals using both MSO and MFO revealed similar results regardless of the constraint. The right chambers of the heart could be discerned in the first time frame, indicating that the transport delay between the left and right chambers of the heart is visible and not accounted for by resolving two factors. However, the signal from this residue is very small when scaled to the original image data, as presented in Figure 4-7.
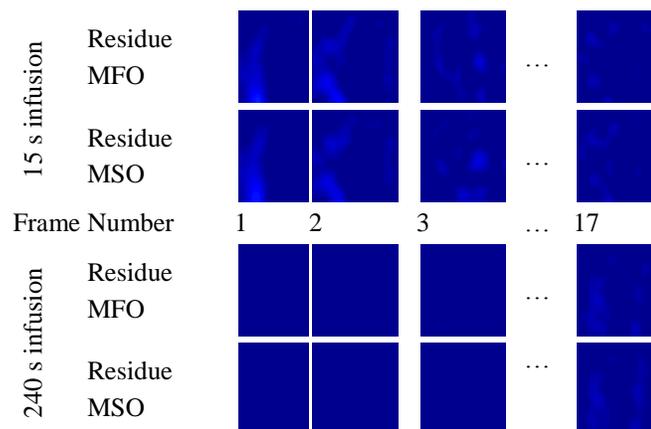
Figure 4-7 – Example of residue in 15s and 240 s infusion images using both MSO and MFO reveals similar patterns regardless of the constraint. In the first time frame some unaccounted residual activity is present due to transport delay between left and right chambers of the heart, but this signal is very low compared to the original image.

The reproducibility of the structures regardless of infusion duration demonstrates the effectiveness of both constraints in resolving a reproducible and unique solution. In addition the importance of a physiologically accurate constrained is emphasized by the difference in the solutions obtained using either constraint.

MSO resolves structures with reduced overlap as expected which may be attractive for applications where improved contrast between regions is desired. The simulation data highlights the inability of MSO to separate blood and tissue signals in the myocardium region. Consequently the myocardium factor consists of tissue signal which was biased by blood signal. A similar effect may be expected in the blood factor, where incomplete separation of myocardium signal is manifested as non-zero activity in late time frames as was observed in both the simulation and canine data.

While MFO appears to overcome the limitations of MSO, this section lacks validation against a physiological standard. In the absence of such a standard, it is especially important to use a constraint that describes the physiology in an accurate and robust manner. There is no physiologic evidence that strictly supports the merit MFO. Thus a need exists for a physiologically accurate constraints and/or physiological validation standards.

4.5 Conclusion

Constraints must be placed on the solutions of decomposed dynamic PET image sequences in order to ensure a unique solution. These constraints must be consistent with knowledge of the physiology in order to ensure physiologically accurate solutions. This section demonstrates that MSO violates our knowledge of spatial overlap between arterial blood and myocardial structures and therefore results in less accurate factors and structures in simulations than the proposed MFO constraint. In repeat images of the same dog MSO results were more variable than MFO results. However, there is no strict evidence to support the validity of MFO and a need remains for a physiologically accurate constraints. In addition a need exists for physiological standards by which to validate the solutions. Both these needs are addressed in the next chapter.

Chapter 5.

Kinetic Model-Based Factor Analysis

The need for physiologically accurate constraints on the decomposition process was demonstrated in the previous chapter. The same chapter also demonstrated the need for better validation of the decomposition results with regards to their physiologic accuracy. This section presents a novel model-based decomposition process that includes a model of the cardiac physiology as part of the decomposition process. The method is validated using both simulation data and physiologic standards. The performance of the proposed method is compared with the performance of MSO. The content of this chapter has been accepted for publication [145].

5.1 Background

Quantification of myocardial blood flow (MBF) from dynamic nuclear image sequences has been pursued as a diagnostic and prognostic indicator of heart disease [10,67,12]. Traditionally, an input and output function are derived using image regions of interest. These functions are then used to optimize the parameters of a tracer kinetic model representing a physiologic process of interest such as blood flow. However, the limited spatial resolution and signal-to-noise-ratio of these modalities can limit the accuracy and precision of the image-derived functions [48,49].

Factor analysis techniques have been explored as a means to obtain functions that are free of noise and spillover contamination from adjacent structures [101]. A dynamic series of images is decomposed into a finite number of temporal factors and their corresponding spatial structures which, ideally, should correspond to the physiology of the imaged tissue. The decomposition may be expressed in matrix form as:

$$Y = FS + \varepsilon \qquad \text{5-1}$$

where Y is the dynamic image sequence (the N pixels of each of M time frames in a row), the columns of F contain the time-activity profiles of the P factors, the rows of S contain the spatial structure of the factor, and ε is error, or residual signal not accounted for by the factors.

Scaling of factors and structures is arbitrary [11], which is evident from their product in equation 5-1. Typically the factors are normalized to unity area during decomposition and are later scaled based on the identification of assumed 'pure' pixels in the image [102,110], or based on blood sampling [101]. Even before scaling, decomposition is non-unique [110,115,146], requiring constraints that reduce the range of valid solutions. In cardiac

positron emission tomography (PET), these constraints have historically defined non-negative factors and structures [104] based on the physical imaging process. In addition, Poisson statistics have been used to model the imaging process [103], but these constraints still do not ensure a unique solution.

Minimization of the spatial overlap between the structures has been proposed as an additional constraint that ensures uniqueness of the solution. The minimal overlap constraint was originally incorporated as part of a penalized least-squares minimization problem [109,124] and later applied as a successive step [72,106]. Unfortunately, minimal structure overlap partially violates *a priori* knowledge of structure overlap that exists between blood and myocardium signals due to the limited spatial resolution of PET, and the normal anatomic presence of 10-15% arterial blood within the myocardial wall. An alternative constraint was proposed that minimizes factor overlap under the assumption that the factors should be as distinct as possible temporally [139]. However, there is no absolute physiologic evidence to support this assumption either.

In this work an alternative approach is developed that couples the factors using kinetic models that describe their physiological relationship in time. These models relate the three main components of the cardiac image dynamics – right cavity blood, left cavity blood (including myocardial vasculature), and myocardium (excluding myocardial vasculature). Consequently, model-based factor analysis is specific to this target application and is expected to benefit from increased *a priori* physiologic information. Cardiac PET with ⁸²Rb may be expected to benefit more than other tracers due to the relatively long positron range, which results in increased image blur, greater mixing of signals and more structure overlap. Implementation for ⁸²Rb is relatively simple due to its kinetics being described with a one-compartment model [39], and factor validation is simplified due to lack of blood or tissue metabolites.

In this study the performance of model-based and minimal-spatial overlap constrained factor analyses was compared using simulation data and experimental data, in which arterial blood sampling and ¹¹CO blood pool imaging served as anatomical standards [145]. Reproducibility of structures and MBF under varying image conditions was also evaluated. A preliminary evaluation of MBF reproducibility is also included.

5.2 Methods and Materials

5.2.1 Minimal Structure Overlap (MSO) Constrained Factor Analysis

MSO decomposition was achieved in two steps: 1) decomposition of the image and 2) rotation of the resulting factors (basis vectors) to minimize spatial overlap as in [106].

Decomposition consisted of minimizing a cost function, C_{MSO}, defined as a weighted sum of the norm of the error matrix $|\varepsilon|$, with penalties for negative structure and factor values as expressed by equation 5-2, where $W_E = 1/|\varepsilon|$, $W_{NF} = 100$ and $W_{NS} = 1$. Negativity was

defined as the norm of all negative elements in matrix X as a ratio of the norm of all elements in X (equations 5-3 and 5-4). The same negativity function, $f_{neg}(X) \in [0\text{-}1]$, was used for both factors and structures, substituting F' or S' for X respectively.

$$C_{MSO} = W_E |\varepsilon| + W_{NF} f_{neg}(F') + W_{NS} f_{neg}(S') \qquad \textbf{5-2}$$

$$f_{neg}(X) = \frac{1}{|X|}\sqrt{\sum_i \sum_j H(x_{i,j})} \qquad \textbf{5-3}$$

$$H(x) = \begin{cases} x^2, & x < \epsilon \\ 0, & x \geq \epsilon \end{cases} \qquad \textbf{5-4}$$

The cost function, C_{MSO}, was minimized by optimizing F' using a simplex gradient descent algorithm (fminsearch, Matlab, The MathWorks, Boston, MA) that was executed in several iterations (epochs) until the variance of ε stabilized to a value less than 10^{-6} of the mean. In each epoch the error penalty, W_E, was set to the value of $1/|\varepsilon|$ from the previous epoch. This approach iteratively estimated the amount of noise in the image, resulting in consistent relative penalty weights without the need to assume a particular noise level.

In the second step, the MSO constraint was applied to minimize the weighted sum of factor and structure negativity penalties as well as spatial overlap penalty, $f_{ovl}(X) \in [0,1]$, as shown in equations 5-5 and 5-6. The matrices F' and S' are the factor and structure matrices resulting from the decomposition stage and R is a $P \times P$ rotation matrix that is optimized to minimize f_{tot}^{MSO}, where P in the number of factors. The resulting factors and structures were defined as $F=F'R$ and $S=R^{-1}S'$ respectively. The parameter b (=0.001) was used to weight the overlap penalty, giving priority to the non-negativity constraint.

$$f_{tot}^{MSO} = f_{neg}(F'R) + f_{neg}(R^{-1}S') + b f_{ovl}(R^{-1}, S') \qquad \textbf{5-5}$$

$$f_{ovl}(X) = \frac{2}{P(P-1)} \sum_{p=1}^{P} \sum_{q=p+1}^{P} \sum_{i=1}^{N} \frac{|X_{ip}|}{\sqrt{\sum_{j=1}^{N} x_{jp}^2}} \frac{|X_{iq}|}{\sqrt{\sum_{j=1}^{N} x_{jq}^2}} \qquad \textbf{5-6}$$

5.2.2   Model-Based Factor Analysis (MB)

The right ventricle (RV) cavity blood factor was treated as an input function that could take any shape, with unit area. Thus the RV factor, $r(t)$, was considered a free variable vector with M-1 degrees of freedom where M is the number of time frames. The left ventricle (LV) cavity blood was modeled by convolution of the RV blood with a model of the delay and dispersion resulting from transport of the RV blood through the lungs and pulmonary vessels to the LV. A standard gamma-variate function (equation 5-7) was adopted to model

this transport [145,147,148,149,150], where the model parameter t_p represents time delay to peak activity [147], and β controls the broadness of dispersion.

$$G(t) = t^\beta e^{-\beta t/t_p} \qquad \text{5-7}$$

The myocardium factor was modeled by convolution of the LV blood factor with a compartmental response function assumed for the specific tracer. In the case of ⁸²Rb, a one compartment model impulse response function was used [39] with a single free parameter k_2 (tracer washout) as in equation 5-8.

$$M(t) = e^{-k_2 t} \qquad \text{5-8}$$

Since the factors were scaled to unit area as part of the decomposition process, the scaling factors typically included in equations 5-7 and 5-8 are redundant, and so were removed. The use of these models to parameterize two of the three factors reduces the number of free parameters from 3(M-1) with MSO to M+2 with the MB method. In addition, coupling of the factors through the modeled response functions imposes a constraint on the solution that agrees with knowledge of the tracer physiology.

5.2.2.1 Optimization

The factor matrix, $\boldsymbol{F}$, was constructed of columns containing RV blood, LV blood, and myocardium factors (equation 5-9), where the symbol $\otimes$ denotes the discrete point convolution operation and integration over the image time frames.

$$\boldsymbol{F} = \begin{bmatrix} r(t) \\ r(t) \otimes G \\ r(t) \otimes G \otimes M \end{bmatrix}^T \qquad \text{5-9}$$

The model-based decomposition process consisted of optimization of the RV blood factor simultaneously with the model parameters to minimize the objective function, C_{MB}, (equation 5-10) which contains the same error and non-negativity penalties used in MSO, but does not include a penalty for spatial overlap. To ensure uniqueness and robustness of the MB solution two penalties were added, f_{BR} and f_R:

$f_{BR} \in$ [0-1] - Penalizes for blood factors that increase in the uptake phase. This penalty was defined as the area bound by the activity of the last RV blood factor time frame, $\boldsymbol{F}_{1,M}$, and activity of time frames post peak RV blood that are below $\boldsymbol{F}_{1,M}$, as demonstrated by the light shaded area in Figure 5-1. This penalty aids convergence by promoting solutions with monotonic decrease in blood activity past the blood peak activity, again consistent with the known physiology.

$f_R \in$ [0-1] – Penalizes for residual blood activity in the uptake phase (past the first 2 minutes) as demonstrated by the dark shaded area in Figure 5-1.

$$C_{MB} = W_E|\boldsymbol{\varepsilon}| + W_{NF}f_{neg}(\boldsymbol{F}) + W_{NS}\,f_{neg}(\boldsymbol{S}) + W_{BR}\,f_{BR} + W_R f_R \qquad \textbf{5-10}$$

The cost function, C_{MB}, was optimized using the same routine used to optimize C_{MSO}. The penalty weights W_{BR} and W_R were empirically set to 10 and 0.01 respectively, while W_E, W_{NF}, and W_{NS} were maintained the same as for MSO. The model parameters were bound based on typical experimental values (Table 5-1). Thus, while MSO solves the ambiguity problem by minimizing the overlap between structures, MB imposes *a priori* physiologic constraints on the shape of the blood factor, as well as the other factors via the kinetic models.
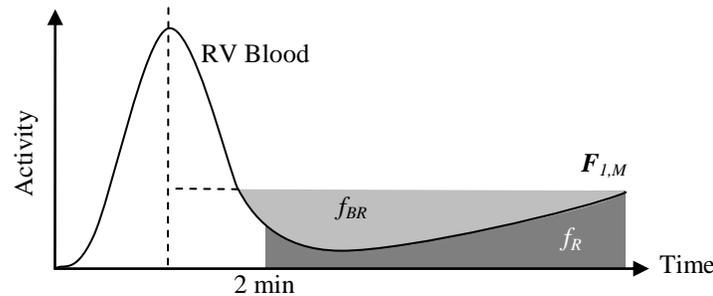
Figure 5-1 – Blood increase penalty, f_{BR}, is the integral of RV blood that is beyond the initial peak and below activity of the last time frame (light shaded area). Residual blood activity, f_R, is the area under the curve from 2 minute to the end of the scan (dark shaded area).

5.2.3   Number of Factors

For both MSO and MB methods, the number of factors (2 or 3 in this case) was determined automatically as the value beyond which $|\boldsymbol{\varepsilon}|$ decreased by less than 1%. In the event of decomposition into only two factors, a single blood factor and a myocardium factor were always resolved. In this case the blood factor was the free variable and the myocardium was modeled using the compartmental model (equation 5-8).

5.2.4   Simulations

5.2.4.1   Canine Simulation

RV blood time activity curves were simulated as a 30 sec, constant rate of activity infusion with dispersion (modeled with a gamma-variate function) en route to the RV cavity. Two forms of RV blood TAC were created to assess the solution's robustness to different input function characteristics:

- Complete clearance of blood activity
- Residual (non-zero) blood activity

Each RV blood TAC was convolved with a gamma-variate impulse response function (equation 5-7) to generate an LV factor. The LV factor in turn was convolved with a one-compartment model impulse response function (equation 5-8) to generate a myocardium factor. The model parameters used for the simulations are shown in Table 5-1. Different

washout parameters, k_2, were selected for the complete blood clearance and residual blood activity cases so that the myocardial TAC had a similar appearance during the late uptake phase of the dynamic image sequence. Each factor was sampled by integrating over 17 time intervals as used in clinical practice (12×10s, 2×30s, 1×60s, 1×120s, and 1×240s).

TABLE 5-1 – ERROR IN RESOLVED PHYSIOLOGIC PARAMETER VALUES WITH MODEL-BASED ANALYSIS (%)

Blood Clearance	Parameter Name	Units	Lower Bound	Initial Value	Upper Bound	Simulated Value	Canine Simulation		Small Animal Simulation	
							No Noise	10% Noise	No Noise	10% Noise
Complete	t_p	sec	2	10	30	15.0	15.0	15.2±0.5	-	-
	β	-	0.25	1	5	2.00	2.00	1.95±0.09	-	-
	k_2	min^{-1}	0.01	0.1	1.5	0.050	0.050	0.051±0.004	0.050	0.049±0.001
Residual	t_p	sec	2	10	30	15.0	15.0	15.6±0.6	-	-
	β	-	0.25	1	5	2.00	2.00	2.24±0.27	-	-
	k_2	min^{-1}	0.01	0.1	1.5	0.500	0.500	0.496±0.036	0.050	0.499±0.037
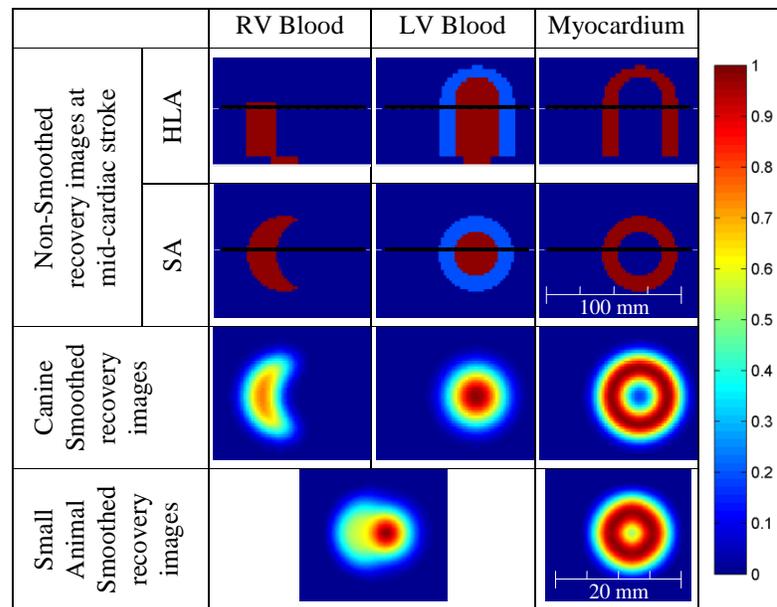
Figure 5-2 – Horizontal long axis (top row) and short axis slices (second row) of simulated structures with a black line showing their intersection. The short-axis slices of the smoothed structures simulate canine images (third row) and small animal images (bottom row). All images are scaled to maximum intensity pixel to emphasize contrast.

These factors were then cross multiplied with their respective recovery images representing the anatomic structures (dimensions shown in Table 5-2) to generate a dynamic sequence of images of tracer redistribution in the heart region. Representative horizontal long axis (HLA) and short axis (SA) images are shown in Figure 5-2. Each recovery image of the simulation was averaged over 36 gates of sinusoidal cardiac motion and wall thickening to preserve the myocardial mass across all gates. Of the dynamic image sequences, one image did not have noise added to it while 5 images had Gaussian distributed random noise added. The images were then smoothed using a 13.6 mm FWHM Gaussian filter. The variance of the noise in each pixel was proportional to the pixel intensity [151].

The noise gain was adjusted (100%) to generate the same post-smoothing image variance in the myocardial region as measured in canine images using a clinical scanner (~10% variance). By adding noise in image-space it was assumed that scatter and attenuation were properly corrected for in the experimental data. Simulated cardiac motion resulted in a spatially variant image blur which is increased in the heart region. Short axis slices of the canine motion blurred and spatially smoothed recovery images are shown in Figure 5-2.

TABLE 5-2 – SIMULATED IMAGE DIMENSIONS

Parameter	Canine	Small Animal
Short axis slice pixel size (mm)	1.72	0.345
Short axis slice thickness (mm)	2.62	0.80
LV diameter (end systole) (mm)	50.40	10.67
Wall thickness (mid cycle) (mm)	7.00	1.00
LV wall motion (mm)	12.60	2.67
RV cavity width (end systole) (mm)	20.59	2.76

5.2.4.2   Small Animal Simulation

Small animal images were simulated in a similar manner as the canine studies, but the dimension were changed as shown in Table 5-2 and the smoothing kernel was set to 4.4 mm FWHM, corresponding roughly to ^{82}Rb imaging with a small animal PET system. Since RV and LV blood could not be distinguished in small animal ^{82}Rb PET images due to the limited temporal resolution of the image, a single blood component was used. The blood structure was created by summation of the LV and RV blood structures. The resulting motion blurred and smoothed recovery images are shown in Figure 5-2. The same LV blood and myocardium TACs from the canine simulation were used for the small animal simulation.

5.2.4.3   Analysis of Simulation Studies

The canine and small animal simulated images were decomposed using both MSO and MB. Factors and structures were compared against the respective TACs and recovery images from the simulation, measuring percent root-mean-squared-error (RMSE%) as shown in equation 5-11 where X_{ref} is a reference matrix from the simulation and X is the results matrix that is being evaluated. For factor evaluation, the weighting matrix, W, was the length of the imaging time frames, and for structure validation W was all ones, weighting each pixel equally. As shown in equation 5-11, the matrices X, X_{ref}, and W were each normalized by their sum.

$$RMSE\% = \left| \frac{W}{\sum W} \cdot \left(\frac{X}{\sum X} - \frac{X_{ref}}{\sum X_{ref}} \right) \right| \times 100\% \qquad \textbf{5-11}$$

Contrast in the myocardium structures was compared with that in the smoothed recovery images. Contrast was defined using equation 5-12, where *Myo* is the maximal

intensity in the myocardium structure and *Cav* is the mean intensity of the four pixels in the center of the cavity of the SA slice shown in Figure 5-2.

$$Contrast = \frac{Myo - Cav}{Myo} \times 100\% \qquad \textbf{5-12}$$

Robustness of convergence of the MB algorithm was assessed by modifying the initial model parameter estimates (default values in Table 5-1) to t_p=5 & 20 sec, β=0.5 & 3, and k_2=0.01 & 1 min^{-1} and decomposing the simulated canine images (resulting in 7 sets of decomposed images). The resulting k_2 parameter estimates were analyzed using box plots for changes in means and/or variances as a result of modifying the initial parameters.

The resolved model parameters from MB were compared to the simulated model parameters. Since, MSO does not resolve similar parameters, an estimate of the washout parameter, k_2', was calculated for both MSO and MB by fitting the one compartment model (equation 5-13) to the LV blood and myocardium factors (*l(t)* and *m(t)* respectively). The parameter *TBF* represents the total blood volume in the ROI and K_1 is the uptake rate, but both these parameters were not analyzed. In this model, it was assumed that the total recovery in the myocardium region consists entirely of LV blood and myocardial tissue due to limited spatial resolution, motion blur, and tissue blood volume.

$$m(t) = TBF \cdot l(t) + (1 - TBF) \cdot K_1 l(t) \otimes e^{-k_2' t} \qquad \textbf{5-13}$$

5.2.5 Experimental Studies

All animal experiments were conducted in accordance with protocols approved by the Animal Care Committee of the University of Ottawa.

5.2.5.1 *Factor Validation with Arterial Blood Sampling*

To test the physiological accuracy of factors (temporal domain), blood factors were compared with activity concentration measurements in arterial blood. Four rats were imaged using ^{82}Rb a total of 6 times with simultaneous and continuous blood sampling. Rats were anaesthetized with 1.5-2% isoflurane and a PE50 catheter was surgically introduced into the carotid artery and fed into the left atrium. A catheter was inserted into the tail vein for tracer injection and a 3-lead ECG, rectal thermometer, and respiration monitor were affixed for physiologic monitoring. A heated bed was used to maintain normal body temperature throughout the experiment.

The rats were placed in an Inveon DPET (Siemens, Knoxville, TN) scanner with the heart centered in the field of view. The arterial catheter was attached to a micro-volumetric blood activity counter [130] (AMI, Sherbrooke, Quebec) for 2-3 mL of blood withdrawal over a 10 min time interval. The PET scan and blood counter were started together approximately 10 seconds before manual injection of ^{82}Rb from a 1 mL syringe, and followed by a 0.4 mL saline flush to clear activity from the catheter lock. List-mode data

were acquired for 10 min using a 350-650 keV energy window and a coincidence timing window of 3.4 ns. The dynamic data (same time frames as simulation) were reconstructed on a 128×128 image matrix with 0.345×0.345×0.80 mm pixel size using OSEM3D/MAP (ß=1.0, OSEM3D iterations=2, MAP iterations=18) with corrections for dead-time, isotope decay, detector efficiencies, and randoms. The image sequences were decomposed using both MSO and MB methods as described above.

Since arterial blood sampled time-activity concentration curves could not be corrected for background activity after tracer injection using the vendor provided software [130], raw counts were analyzed. Counts were corrected for tracer decay, background activity (10 sec preceding first rise in sampled activity), delivery delay, and the spatial resolution of the β^+ detector. In addition, the corrected blood curves were integrated over the same time intervals as the dynamic image sequence. The integrated curves were normalized to unit area before comparison with the MSO and MB derived blood factors using RMSE (%) with each time frames weighed by its length normalized by the total scan duration as in equation 5-11.

5.2.5.2   Structure Validation with [11]CO Blood Pool Imaging

A single dog was anaesthetized using ~2% isoflurane and positioned in a whole-body PET scanner (ECAT ART, Siemens/CTI, Knoxville, TN) with the heart centered in the field-of-view. A series of ten dynamic scans (same time frames as simulation) was acquired with varying [82]Rb constant-activity (150 MBq) rate infusion [35] durations (15, 30, 60, 120, 240, 240, 120, 60, 30, 15 seconds). All images were acquired at rest flow state with blood pressure, heart rate, and respiration maintained constant. The images were reconstructed iteratively (OSEM) to 12 mm resolution.

The images were cropped manually to include the entire heart (same crop applied to all 10 images). The cropped regions were then decomposed using both MSO and MB methods. The number of factors was automatically determined, but in cases having two blood structures (RV and LV), they were summed to form a single combined blood pool structure.

The blood structures extracted from each of the 10 images were compared to a single [11]CO blood pool image of the same animal acquired on a separate day and reconstructed to the same 12 mm resolution. [11]CO binds to haemoglobin in the blood resulting in images of the total blood distribution, therefore serving as a good anatomic reference to validate the accuracy of the factor analysis blood structures.

Contrast in the myocardium structures was compared with that of the uptake phase (last 6 minutes) images. Contrast was defined using equation 5-12, where *Myo* and *Cav* are the mean pixel intensities in the LV myocardium and LV blood cavity ROIs respectively. The ROIs were automatically determined [39,134].

5.2.5.3   Global MBF Reproducibility using Variable Tracer Infusion Durations

Global MBF was quantified in the same canine images. The myocardium ROI was used to sample kinetic modeling output function, $m(t)$, from the dynamic image sequences. Likewise, the LV blood cavity ROI (ROI$_b$) was used to sample the kinetic model input function, $l(t)$. These were used with the kinetic model of equation 5-13 to determine uptake rate, K_1, and MBF was calculated from K_1 using a previously derived Renkin-Crone extraction function [39].

The MSO and MB blood factors were used as alternative input functions in equation 5-13 and were scaled by the average blood structure in the ROI$_b$. If two blood factors (RV and LV) existed they were both scaled using their respective structure ROI$_b$ and summed, thus accommodating incomplete spatial separation of the blood factors into RV and LV cavity blood. The benefit of including the RV blood time activity curve, $r(t)$, in the kinetic model using equation 5-14, where *RVBF* and *LVBF* are the right and left ventricle blood fractions in the myocardium ROI, was also evaluated. The maximum pixel value in the RV structure was used to scale $r(t)$. As in equation 5-13, equation 5-14 also assumed that the total recovery in the myocardial region consists entirely of RV blood, LV blood, and myocardial tissue.

$$
\begin{aligned}
m(t) = RVBF \cdot r(t) + LVBF \cdot l(t) \\
+ (1 - RVBF - LVBF) \cdot K_1 e^{-k_2' t} \otimes l(t)
\end{aligned}
\qquad \textbf{5-14}
$$

Reproducibility of MBF using the ROI based method as well as using all combinations of MB and MSO, with and without RV blood were evaluated.

5.2.5.4   Structure Reproducibility using Variable Tracer Infusion Durations

The myocardium and blood structures obtained from the 10 variable infusion duration images were compared (RMSE%) in all possible combinations (n=45) to determine the reproducibility of blood and myocardium structures. In addition, the coefficient of variation of each pixel across the 10 images was computed and was then averaged across all the pixels in the regions of interest, and was referred to as CV%. CV% was measured for blood structures and myocardium structures both for MSO and MB.

5.2.6   Statistical Analysis

Unless otherwise specified, all values are reported as mean ± standard-deviation. Comparison of means was performed using a two-tailed paired student t-tests, with p=0.05 as the cut-off for significance. Comparison of variability was performed using the parametric f-tests with the same significance cut-off. Both the student t-test and the f-test assume normal Gaussian distribution, which was not explicitly tested. Statistics regarding images and/or structures relate to all pixels within the entire region of interest.

Comparison of population variables is presented using notched box plots showing the median and inter-quartile range. Outliers are identified outside the whiskers extending to

1.5 times the quartiles. Non-overlapping notches reflect significantly different medians with 95% confidence.

The Wilcoxon, non-parametric rank sum test was used to test the significance of differences in CV% with p=0.05 as the cut-off.

5.3 Results

5.3.1 Canine Simulation

Table 5-3 lists the RMSE between the simulated and resolved factors and structures using both decomposition methods. With few exceptions, MB errors were lower than corresponding MSO errors. With no noise the mean factor RMSE was 0.5% with MSO, while all factor RMSEs were <0.05% with MB. With noise the MSO factors had significantly (p<0.001) higher RMSE values (0.5%) compared to MB (0.2%). Similarly, in the absence of noise, the structures mean RMSE were 2.5% and <0.05% for MSO and MB respectively. With noise the MSO and MB structure errors were 4.7% and 3.0% (p <0.001).

TABLE 5-3 – SIMULATED IMAGE RESULTS – ROOT MEAN SQUARED ERROR (%)

Blood Clearance	Factor	Factors					Structures				
		No Noise		10% Noise (n=5)			No Noise		10% Noise (n=5)		
		MSO	MB	MSO	MB	p	MSO	MB	MSO	MB	P
Complete	RV	0.0	0.0	0.3±0.1	0.3±0.2	1.000	1.4	0.0	2.7±0.5	1.7±0.1	**0.015**
	LV	0.6	0.0	0.6±0.1	0.1±0.0	**0.001**	1.3	0.0	2.9±1.2	2.7±0.6	0.658
	Myo	0.2	0.0	0.3±0.1	0.1±0.1	**0.001**	2.2	0.0	4.2±1.0	3.8±0.7	0.059
Residual	RV	1.3	0.0	0.9±0.4	0.2±0.1	**0.027**	0.0	0.0	2.7±0.3	1.6±0.1	**0.002**
	LV	0.2	0.0	0.5±0.2	0.2±0.1	0.095	7.1	0.0	8.0±1.8	2.8±0.6	**0.001**
	Myo	0.5	0.0	0.7±0.2	0.1±0.0	**0.004**	2.9	0.0	7.5±0.8	5.6±1.3	**0.0275**
Mean		0.5	0.0	0.5±0.3	0.2±0.1	**<0.001**	2.5	0.0	4.7±2.5	3.0±1.5	**<0.001**
Rat Simulated Data											
Complete	Blood	1.7	0.0	1.7±0.2	0.2±0.1	**<0.001**	1.8	0.0	6.0±2.9	1.7±0.3	**<0.001**
	Myo	0.2	0.0	0.7±0.3	0.2±0.1	**0.023**	6.2	0.0	6.7±0.8	2.5±0.6	**<0.001**
Residual	Blood	0.4	0.0	0.4±0.1	0.4±0.2	0.529	0.6	0.0	8.4±2.2	1.9±0.6	**<0.001**
	Myo	0.1	0.0	0.8±0.1	0.1±0.0	**<0.001**	4.1	0.0	5.9±1.1	5.9±2.2	**<0.001**
Mean		0.6	0.0	0.9±0.5	0.2±0.1	**<0.001**	3.2	0.0	6.7±2.1	3.0±2.1	**<0.001**

The simulated factors and factors resolved from the images with noise are plotted in Figure 5-3. For the simulation of complete blood clearance, MSO and MB agree with the simulation similarly well. In the simulation of residual blood activity MSO results exhibited systematic deviation from the simulated factors with confidence intervals that do not overlap the simulated lines in the early time frames. MB confidence intervals overlapped the simulated curves.
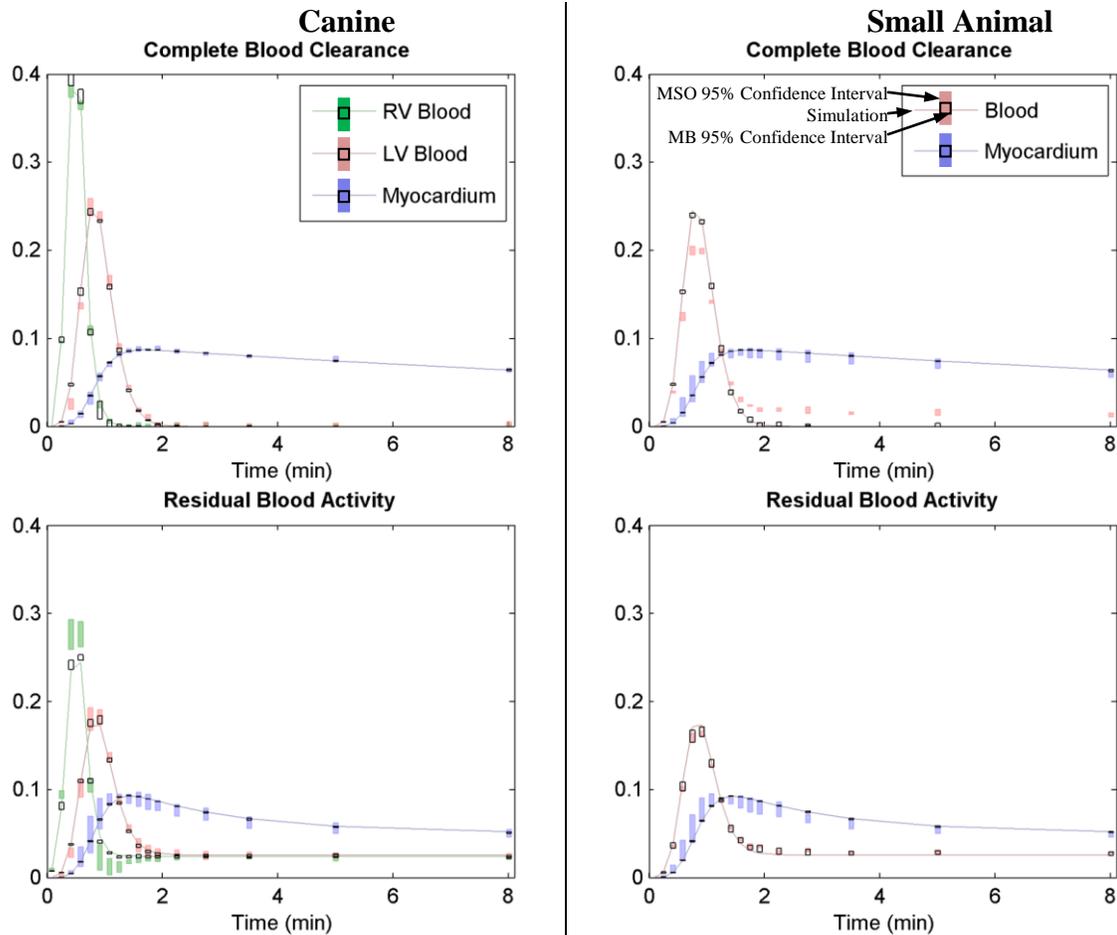
Figure 5-3 – Comparison of resolved RV blood (green), LV blood (red), and myocardium (blue) factors from images with 10% noise (n=5) to the simulated profiles (lines). Top figures represent complete blood clearance and bottom figures represent residual blood activity. Left plots are for canine simulations and right plots are for small animal simulations. The heights of the error bars represent 95% confidence intervals for MSO (color) and MB (black).

Short axis slices of the resolved structures from the simulations without noise using both MSO and MB are shown in Figure 5-4. In general, the myocardium structures reproducibly agreed with the simulated recovery images. However, the MSO derived RV blood structure extended incorrectly into the septal wall (left part of myocardium) and LV blood region for the case with complete blood clearance. Likewise, with residual blood activity the MSO derived LV blood structure extended somewhat into the septal wall and RV region, whereas the MB structures agreed more closely with the simulated recovery images. With residual blood activity the myocardium:blood contrast (superimposed in white) in the uptake image (29%) was markedly improved both with MSO (89%) and MB (82%), but MB agreed more closely with the simulated myocardium structure (82%).
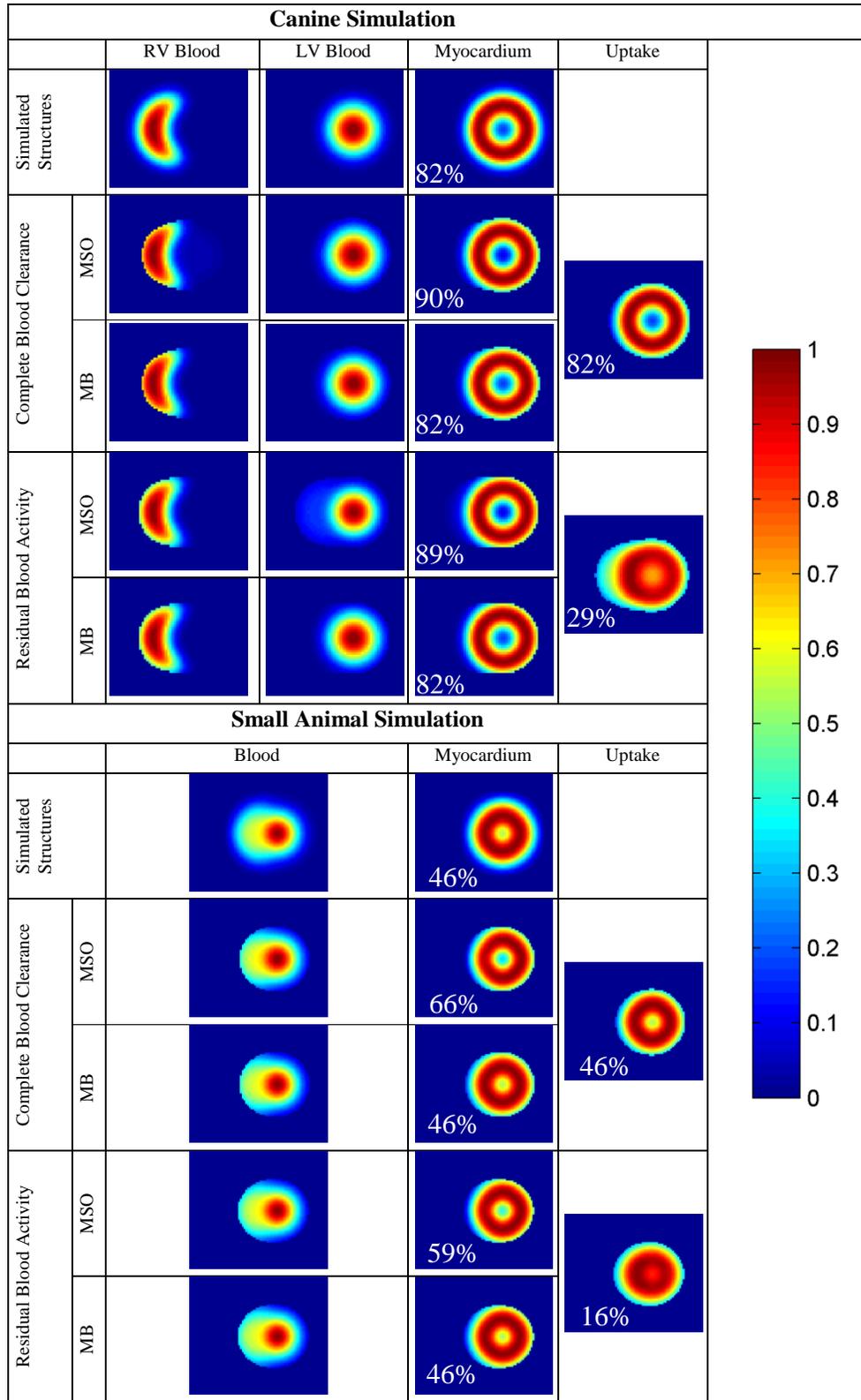
Figure 5-4 – Short axis slices of decomposed structures using MSO and MB methods on canine (top half) and small animal (bottom half) simulated dynamic images are compared with simulated structures and uptake images (frame 17). White numbers are contrast between myocardium and spillover into the LV cavity (equation 5-12).

The MB method recovered the model parameters accurately in the absence of noise and with modest errors in the presence of noise as shown in Table 5-1. In the absence of noise, the simulated values were recovered to within three significant figures. In the presence of noise the simulated values were within the range of the mean ± one standard deviation. The largest bias in parameter estimates was 8.3% for the β, and the smallest average being 3.5% for t_p. The same analysis could not be performed on MSO results because the kinetic model parameters are not resolved as part of the decomposition process.

Estimates of k_2 parameters, k_2', were determined by fitting the kinetic model (equation 5-8) to the LV blood and myocardium factors. For the complete blood clearance cases k_2' were 0.065±0.020 and 0.048±0.004 with MSO and MB respectively, and for residual blood activity the corresponding values were 0.486±0.100 and 0.478±0.032. In all cases the mean did not significantly differ from the simulated values 0.05 and 0.5 (p>0.1). However, the variance of k_2' with MSO was significantly greater than with MB (p<0.001).

Convergence of the MB algorithm was found to be robust regardless of the initial model parameters and is demonstrated by the box plots of k_2 parameter (Figure 5-5) using 5 realizations of noise in the cases of complete blood clearance (C) and residual blood activity (R) for 7 different initial estimate combinations of the model parameters (t_p, β, and k_2). Variances were similar for the complete blood clearance case and identical for the residual blood case. Regardless of the initial estimates, mean k_2 was not significantly different from the true values (green lines). In addition, Figure 5-5 shows the k_2 values from the images without noise as blue stars, all of which deviated less than 0.002% from the simulated values.
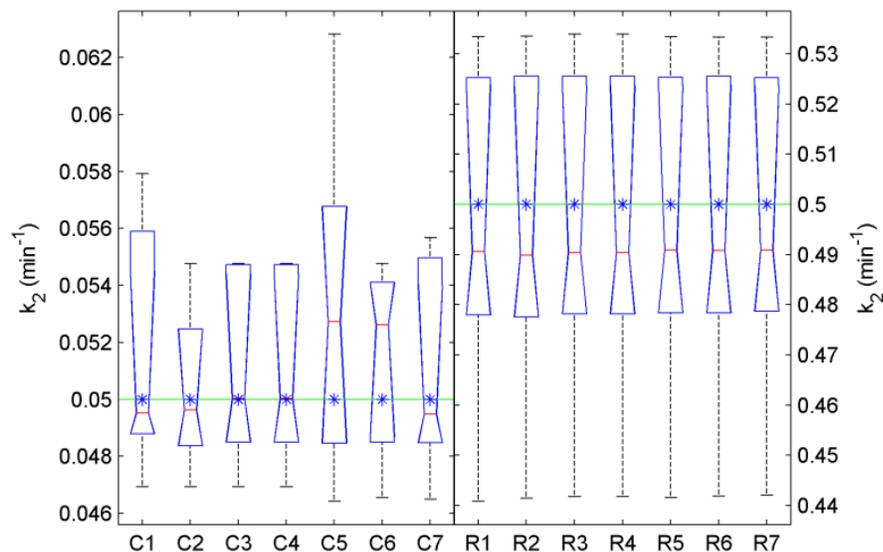
Figure 5-5 – Box plots (n=5 simulated images with noise) of k_2 parameters with 7 different initial parameter estimates each for complete blood clearance and residual blood activity (C and R respectively). The blue stars are results for (n=1) case with no noise and are not included in the box plot analysis.

5.3.2   Small Animal Simulation

In the presence of noise, significantly lower RMSE was obtained with MB factors (p<0.001) and structures (p<0.001) compared to MSO, as shown in Table 5-3. Both the MB factors and structures agreed closely with the simulation data as shown by the estimated structures in Figure 5-4 and the factors in Figure 5-3.

The MSO derived myocardial structure for the case of complete blood clearance had a noticeable reduction in the septal wall as shown in Figure 5-4 and the corresponding blood factors failed to decrease to near zero activity (Figure 5-3). In the case of residual blood activity the MSO derived myocardium factors displayed greater activity at early time frames which is typical of contamination by blood signal [101] and activity in the septal wall was also reduced compared to the rest of the myocardium.

The MB derived myocardium factors had myocardium:blood contrast (46%) that agreed well with the simulation values (Figure 5-4). As expected, MSO increased the contrast to 66% and 59% respectively for the cases of complete blood clearance and residual blood activity. Both methods significantly improved contrast over that of the uptake image (16%) in the case of residual blood activity.

5.3.3   Experimental Factor Validation with Arterial Sampling

Comparisons of blood factors obtained using MSO and MB are shown in Figure 5-7 for all six rats. Various injection profiles were used: fast bolus (a and f), slow bolus (b), dual injections (c, d, and e). Both MB and MSO showed reasonable correspondence with the sampled blood curves in the first 2-3 minutes, but systematically differed in the late time frames (uptake phase). The MSO derived blood factor consistently had residual blood activity, while MB derived blood factors consistently dropped to near zero activity. Blood sampled curves consistently dropped to near zero activity, but not as fast as the MB blood factors did.

Mean RMSE values were 2.2±0.7% and 1.6±0.4% with MSO and MB respectively (shown in the box plots of Figure 5-6). The mean RMSE with MB was significantly lower than with MSO (p=0.027), but the variance was not (p=0.3).
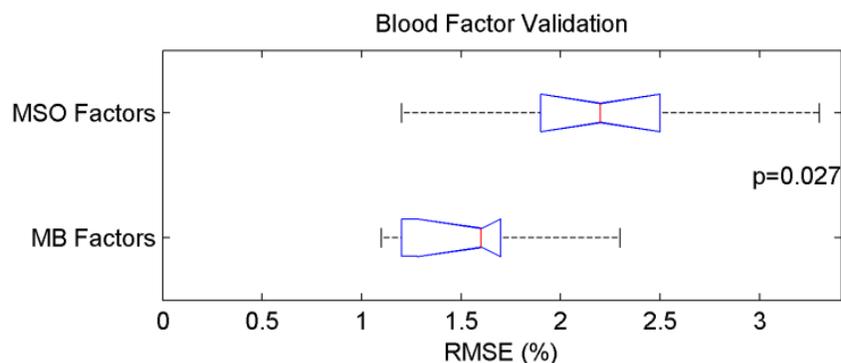
Figure 5-6 – Comparison of MSO and MB derived blood factors to arterial blood sampled curves.
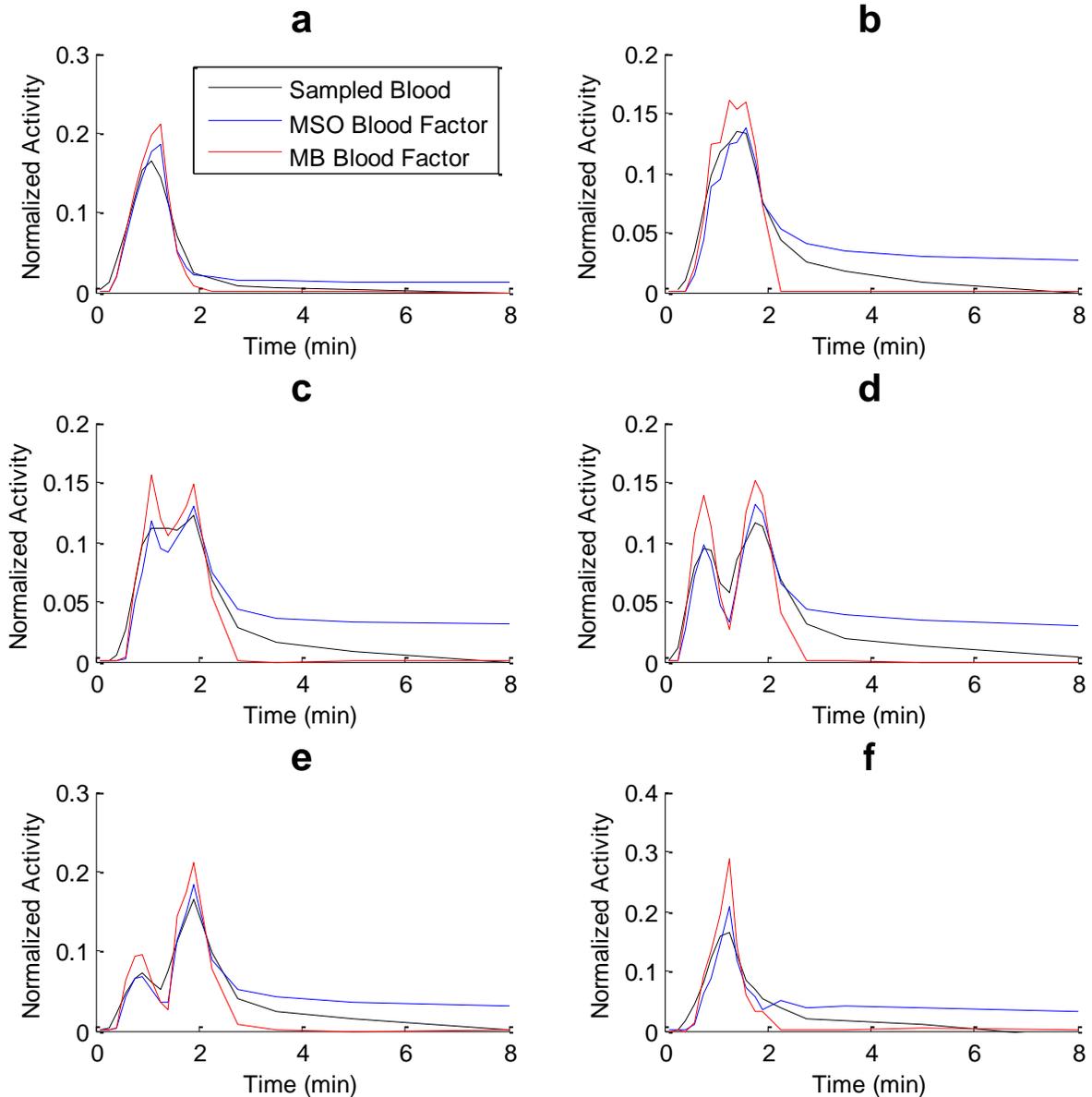
Figure 5-7 – Blood factors obtained using both MSO (blue) and MB (red) methods compared to blood sampled curve (black). All curves are normalized to unity area.

5.3.4   Structure Validation with ^{11}CO Blood Pool Imaging

The number of resolved factors was consistently 2 for long tracer infusions (≥120s) and 3 for short infusions (≤30s). Where 3 factors were resolved, spatially distinct RV and LV structures were observed as demonstrated in Figure 5-8.

Factors were representative of the infusion duration. Blood factors had a more gradual rise and delayed clearance with prolonged infusions. Likewise myocardial uptake was more gradual as expected. In all cases, blood activity cleared almost completely at the last time point, as demonstrated by the factors in Figure 5-8.
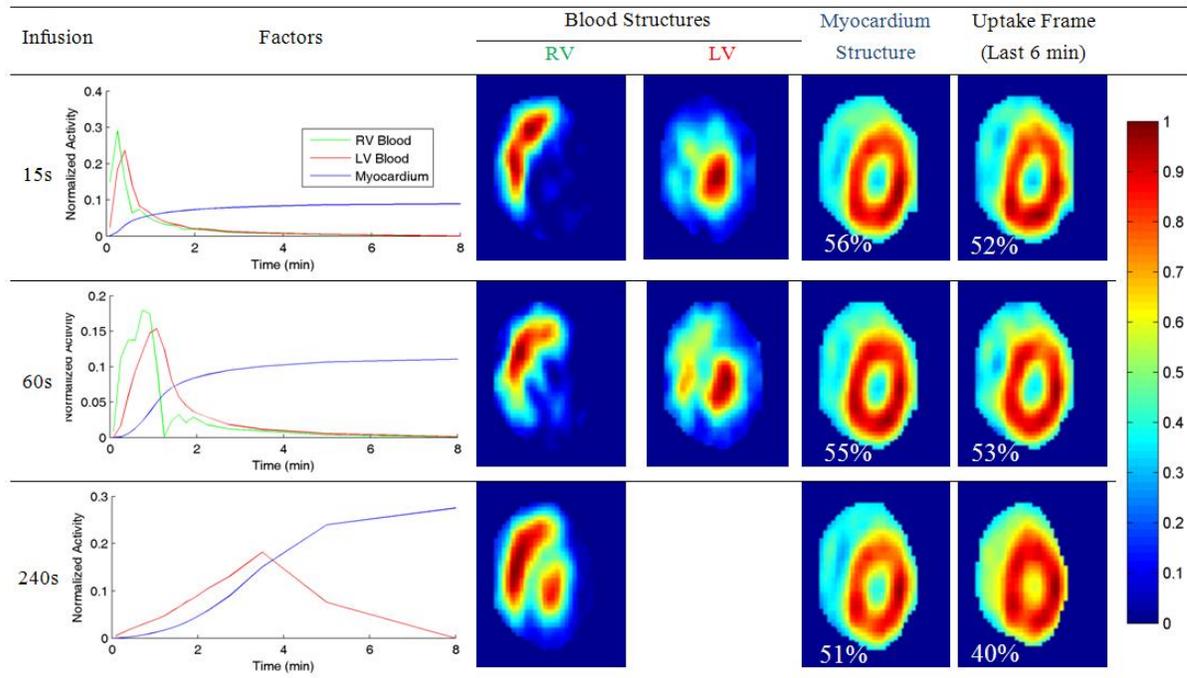
Figure 5-8 – Example short axis slices of resolved factors and structures, and uptake (last 6 min) frames for a 15s, 60s, and 240s infusion duration example in a dog.

Agreement of the blood structures with the ^{11}CO blood pool image of the same animal was good, with RMSE<9.7% in all cases for both MSO and MB. Box plots of the RMSE are shown in Figure 5-9, indicating no significant differences in RMSE (p=0.23) with MB compared to MSO values. No obvious trends in RMSE with infusion duration were observed with either method (data not shown). No significant difference was detected in the variability of RMSE (p=0.8) between MSO and MB.

5.3.5   Structure Reproducibility using Variable Tracer Infusion Durations

Reproducibility of structures was good to excellent. For all RMSE combinations (n=45), RMSE was ≤11.0% with MSO and ≤7.2% with MB. Box plots of the RMSE values for blood and myocardium structure reproducibility are shown in Figure 5-10. Mean myocardial RMSE was 6.2% with MSO vs. 3.9% with MB (p<0.01), and in blood structures respective mean RMSE values were 5.6 % vs. 4.9% (p=0.006). The single outlier (red cross) was in MSO blood RMSE between a 15 and a 60 sec infusion. Visual comparison of the structures in this study with others did not reveal an obvious difference in spatial patterns and a single outlier from 45 sets can be expected due to random distribution.

Myocardium:blood contrasts were 49±5%, 62±7%, and 52±3% in the uptake images, MSO myocardial structures, and MB myocardial structures respectively as demonstrated by the corresponding contrast superimposed on the images in Figure 5-8. Mean contrasts using either MSO or MB were significantly higher than in the uptake images (p<0.001 for MSO

and p=0.04 for MB). The variance in the contrast across the 10 images tended to be reduced with MB compared to MSO (p=0.062) indicating better reproducibility.

The mean CV% (n=75,782 pixels) across the 10 myocardial structures was 12.9% and 6.5% for MSO and MB respectively. Across the 10 blood factors respective CV% was 16.8% and 11.4%. The combined CV% for myocardium and blood structures was 12.9% for MSO and 8.9% for MB. All the differences between MSO and MB were significant (p<0.001), indicating that MB resolved more reproducible structures in the same animal with varying tracer infusion.

Figure 5-9 – Comparison of MSO and MB derived blood structures to [11]CO blood-pool images (CO).
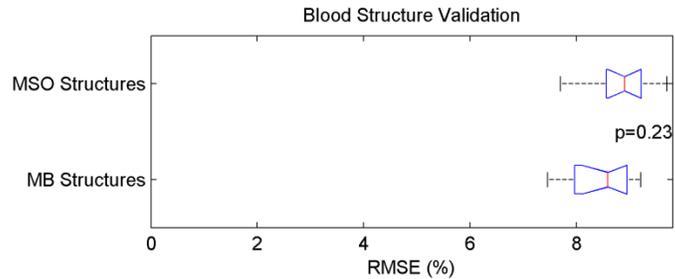
Figure 5-10 – Reproducibility of blood structures (top two rows) and myocardium structures (bottom two rows) obtained from variable duration infusions using MSO and MB.
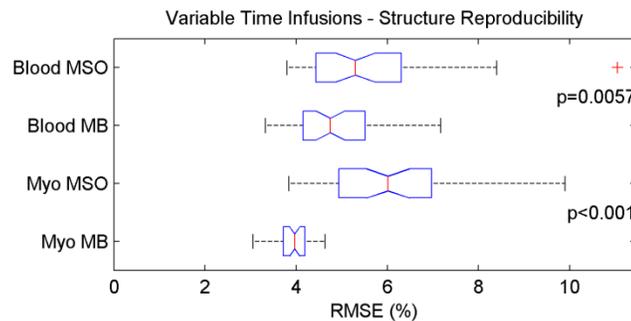
TABLE 5-4 – REPRODUCIBILITY OF MBF QUANTIFICATION
MEAN±STANDARD-DEVIATION (CV%)

	ROI	Without RV Blood		With RV Blood	
		MSO	MB	MSO	MB
K1	0.58±0.06 (10%)	0.76±0.08 (11%)	0.78±0.05 (7%)	0.77±0.08 (10%)	0.80±0.05 (6%)
MBF	0.98±0.17 (17%)	1.56±0.30 (19%)	1.65±0.21 (13%)	1.61±0.29 (18%)	1.71±0.18 (10%)

5.3.6 Global MBF Reproducibility using Variable Tracer Infusion Durations

MBF quantification and estimates (shown in Table 5-4) with MB tended towards smaller variability than with MSO, as indicated by small CV% values, but did not reach statistical significance (p=0.21 and p=0.15 without and with RV respectively for K1, and p=0.32 and p=0.16 for MBF). Amplification of the MBF variability compared to that of K_1 is expected due to the non-linear relationship of the extraction function. Both with MSO and MB factors, variability in global K_1 and MBF estimates did not improve significantly (p>0.7) with the addition of the RV blood in the model.

Mean K_1 and MBF values both with MSO and MB factors were significantly higher than ROI based values (p-value<0.001) indicating that the extraction function may not be applicable for quantification using factors, and that a new calibrated extraction function must be derived.

5.4 Discussion

This work described the development, validation, and comparison of two dynamic image decomposition methods, MSO and MB. These methods were implemented in an identical manner with the exception of the constraints imposed on the solution so as to resolve the non-uniqueness problem. The previously reported MSO method [72,106,124] constrained the solution be minimizing the spatial overlap between structures. The method described in this work, MB, constrained the solution by use of kinetic models between the factors, and penalizing residual blood activity and rise in tracer blood concentrations in the uptake phase of the image to ensure uniqueness of the solution.

Simulation results clearly showed that the MB method outperforms MSO for accuracy in recovering factors and structures, particularly in small hearts where the limited resolution of PET leads to greater spatial overlap between structures. The small animal simulations demonstrated that MSO's inability to separate myocardium and blood signals can result in less accurate blood factors and myocardium factors contaminated by blood signal. In addition, MSO derived myocardium structures may suffer from reduced intensity in the septal wall which could be misinterpreted as a defect. However the higher myocardium to blood pool contrast of MSO derived myocardium structures may be beneficial for registration and segmentation purposes. If regions of pure blood exist in the image, such as in large hearts, MSO and MB are both expected to resolve accurate blood factors that have less noise than ROI based methods. Scatter in the image may be regarded as an additional, broad blurring kernel, in which case MB is expected to yield more accurate blood factors than MSO.

The experimental results largely agreed with simulations and suggested that MB can be more accurate and more reproducible than MSO. Blood factors were more accurate when derived with MB as indicated by arterial blood sampling. However, comparison of blood structures to blood pool imaging did not demonstrate superiority of either MSO or MB.

5.4.1 Residual Signal

The premise of dynamic image decomposition is that most of signals in the image are represented by the factors and that the residual signal contains a combination of noise and smaller signals that can be disregarded. Figure 5-11 demonstrates the residue in decomposition of the canine simulation with no noise and complete blood clearance using MSO and MB. The three columns (left to right) show the original image sequence, the scaled structures that compose the image, and the residue. Both with MSO and MB the residue is

random and is 5 orders of magnitude smaller than the dynamic image sequence. This qualitative information indicates good convergence using both methods as the combined factors and structures accurately represent the dynamic sequences in the image. This supports the notion that any difference in results between MSO and MB are a result of the constraints rather than implementation of the optimization routines.
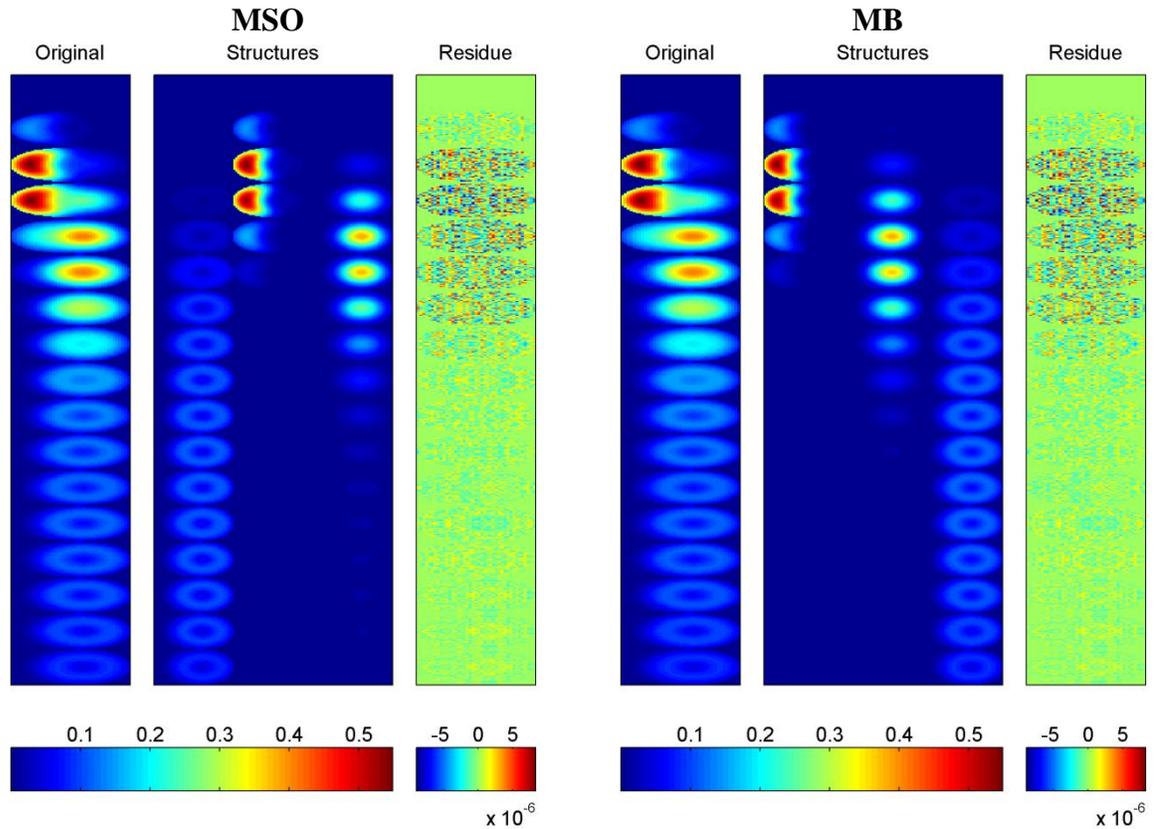
Figure 5-11 – Decomposition results showing original image sequence as a series of frames from top to bottom, the scaled structures for all time frames, and the residual signal for MSO (left) and MB (right) for the noise-free total blood clearance case. The residue image using both methods is completely random and on the scale of 10^{-6}.

5.4.2   Penalty Weights

Both MSO and MB cost functions (C_{MSO} and C_{MB} in equation 5-2 and 5-10 respectively) consist of weighted penalties. The respective weights were adjusted empirically using the simulated data to ensure convergence and good correspondence of factors and structures with the simulated data. Since the respective penalties are all bound between 0 and 1, their weights somewhat determine their relative importance. We prioritized the MSO penalties in order of non-negative factors, non-negative structures, and minimal spatial overlap and for MB, the penalties were prioritized in order of non-negative factors, no rise in blood activity during the uptake phase, non-negative structures, and minimal residual blood activity in the uptake phase. In order to test the sensitivity of the chosen parameters, we varied the weights over 1 order of magnitude and found that the results changed little (data

not shown). The reported penalty weights were used for all images and are assumed suitable for future images (normal and diseased humans and animals). A limitation of this work is that automatic parameter selection was not demonstrated. Future work should evaluate the current penalty weights and/or tune them in a wider population consisting of healthy and diseased individuals.

5.4.3   Execution Time

In 30 of the 40 images used in this work, the execution time with MB was shorter than with MSO. On average the execution times ratio (MSO/MB) was 2.4±2.4. Although MSO requires less computation per iteration compared to MB, MSO has more free parameters to optimize. The median execution time with MSO was 9.6 hours and 5.8 hours with MB on a 2.1 GHz Intel Quad Core 2, with 4GB RAM under Windows XP 32 bit. In a clinical setting, where several dozen images could be acquired in a single day, MB in its current form could not be sustained as part of the routine workflow without powerful computing infrastructure.

In this work, there was little emphasis on performance and more on precision, however there are several potential possibilities for accelerating execution, such as using a subset of pixels and reducing the tolerances on the optimization stopping criteria. Execution time could be reduced by implementing the algorithm in a more efficient, non-interpreter based language such as C as opposed to Matlab. Since the MB optimization is parallelizable and involves many floating point operations, execution could be drastically accelerated by employing a graphical processing unit (GPU) [152,153] such as CUDA (NVIDIA, Santa Clara, California).

Execution time could also be shortened by reducing the number of dixels that are used during the decomposition process. This could be achieved either by defining smaller ROIs, or using a subset of the dixels in the ROI. A commonly used approach in large scale optimization problems is to use ordered subsets of the dixels that change during iterations of the optimization [152,154]. Once decomposition is completed, the resulting factors can be applied to the entire image, or any ROI, to resolve the structures within the same region.

5.4.4   Blood Clearance

Previous studies demonstrated that blood clearance results can vary with different decomposition methods and constraints [139]. The purpose of simulating data with and without blood clearance was to ensure that no bias existed in MB. The results of Figure 5-3 demonstrate an ability to reliably resolve both scenarios using the MB method even in the presence of noise. The blood factors obtained from real images tended towards complete blood clearance which agrees with previous observations [45].

The MSO method did not reliably result in clearance of activity from the blood factors. In the canine simulation where the structures were relatively large compared to

image resolution, blood clearance was resolved correctly. However, this was not the case in the small-animal simulation where the relatively larger blur resulted in no pixels with pure blood signal. In the rat experiments, residual blood activity was observed in all images, agreeing with the simulation results. One could expect more accurate results with MSO in other organs without substantial blood contamination [124]. However in small animal studies and humans with small hearts MSO may be biased, especially with the high positron range of ^{82}Rb.

5.4.5 ^{11}CO Blood Pool Images

Although MB derived blood structures tended to agree better with ^{11}CO blood pool images than MSO derived blood structures, no significant difference was found (p=0.23). Qualitatively, MSO blood structures were more defined, having a smaller LV and RV cavity regions and a larger gap in the septal wall region as demonstrated for a 50 sec elution results in Figure 5-8. The MSO myocardium factors (blue line in Figure 5-12) had greater activity in the early time frames than the MB derived factor (dashed blue line), consistent with blood signal contamination [101]. Thus MSO reduces spatial overlap of myocardium and blood structures by attributing the blood signal in the myocardium region to myocardial signal.
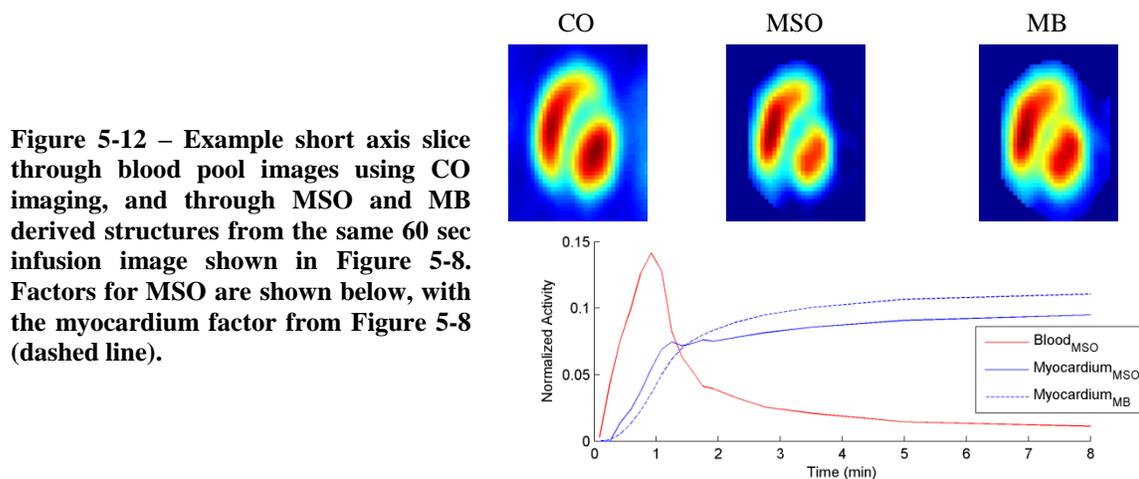
Figure 5-12 – Example short axis slice through blood pool images using CO imaging, and through MSO and MB derived structures from the same 60 sec infusion image shown in Figure 5-8. Factors for MSO are shown below, with the myocardium factor from Figure 5-8 (dashed line).

With either decomposition method, correspondence between blood structures and ^{11}CO blood pool images (Figure 5-9) was worse than between pairs of blood structures (Figure 5-10) as reflected by significantly greater RMSE values (p<0.001). The ^{11}CO image, which was taken on a separate occasion, was translated spatially to align with the blood factors, but no rotation correction was applied. In addition, ^{82}Rb images may suffer from bias due to 777keV prompt gammas that may not be fully corrected [155]. Image spatial resolution may also be slightly different due to positron range even though complimentary smoothing was applied to the ^{11}CO image.

While comparison of structures under different infusion durations enables good reproducibility measurement it does not ensure physiological accuracy. It is desirable to improve the correspondence with CO images. Repeating the experiment with CO imaging on

the same session as ^{82}Rb may be beneficial for optimal evaluation. Also labelling CO with ^{15}O instead of ^{11}C could more closely reproduce ^{82}Rb resolution loss due to the longer positron range.

5.4.6 ^{82}Rb Blood Sampling in Rats

The use of ^{82}Rb as an imaging agent in rats is not ideal due to the combination of small anatomy and large positron range. As a result the image resolution is on the same order (or less) as the size of the imaged organ. Rats were chosen to achieve sufficiently high tracer concentrations in the blood for the micro-volumetric sampler to have adequate precision. This was not possible in larger animals since their larger blood volume significantly dilutes tracer concentrations. More sensitive blood sampling equipment would enable similar experiments in larger animals in which imaging conditions are more favourable.

Although the heart walls could not be resolved in the reconstructed images, it is impressive to note that reasonable decomposition could still be achieved using both MB and MSO methods as demonstrated by the results of Figure 5-6 and Figure 5-7.

MSO blood factors always demonstrated residual blood activity in the late time frames, which was consistent with inaccuracies in the small animal simulations. MB blood factors on the other hand showed complete blood clearance which agreed more closely with the blood samples. Nevertheless, a sudden drop to near zero activity in the MB blood factors is apparent in the rat data, which may indicate that the residual blood penalty is too severe. As mentioned above, penalty weights were manually adjusted and MB could potentially benefit of a more rigorous tuning including the penalty weight and the number of frames which constitute the uptake phase.

5.4.7 ^{82}Rb Infusion Duration

Optimal ^{82}Rb infusion duration for perfusion quantification has been explored previously [36]. While mean perfusion values did not change with infusion durations, regional variability decreased with longer infusions (possibly increasing quantification precision). The disadvantage of long infusions, however, is that the uptake image, reported clinically, suffers from reduced myocardium to blood contrast (Figure 5-8). The reduction in contrast is due to insufficient time for complete tracer clearance from the blood. The myocardium structures obtained with model-based factor analysis can recover image contrast by removing blood signal contribution. Model-based factor analysis may make long ^{82}Rb infusions practical, with improved perfusion quantification and high contrast myocardial structure images for routine clinical applications.

5.4.8   MB with Other Tracers

Previous PET image decomposition methods were not tracer specific. While, the one-compartment model used in this work is also applicable to other tracers, such as ammonia [76], acetate [156], and HED [157], the kinetics of some tracers may be better modeled with

a two-compartment model. The MB method is compatible with two-compartment kinetic models as well as blood metabolite corrections, however further validation is required.

5.4.9   Number of Factors

While MSO can be used to resolve any number of components, MB assumes the existence of specific types of components in the image. This work dealt with solving one blood component and one myocardium component as well as two blood components and one myocardium component. Additional tissue components (such as stomach or liver) could be accommodated with additional factors with a response function as in equation 5-8 or a different model and associated model parameter constraints. Models need to be customized for the tracer and organ in question. Regardless of implementation, the temporal response of additional tissues would have to be sufficiently different from that of the myocardium to obtain reliable component separation.

5.4.10   Application of FA to Quantification of Myocardial Physiology

Regardless of the decomposition method, it is assumed that factors represent uniform temporal responses of image components. This has raised concerns, particularly in diseased myocardium, where the temporal responses of diseased and healthy regions may vary. In MB this issue is manifested by resolving a single washout parameter, k_2, which is assumed constant for the entire myocardium. This issue may be resolved by using the blood factors as the input functions to the kinetic model and ROI sampled myocardial TACs as the output functions[72,106]. The disadvantage of using ROI derived output function compared to myocardium factors is that they contain noise

Quantification of MBF using ^{82}Rb and kinetic modeling requires the implementation of an extraction fraction correction [29,30] which is calibrated to a standard [39]. Calibration of the extraction function can also correct for biases of the input and output TACs and of the physiologic model parameters. In the variable infusion duration results it was evident that the extraction correction function was calibrated for the ROI based method, but not for the use of factors as the input functions (MBF changed from ~0.98 with ROI to ~1.65 with factors). Calibration was not possible in this case since the data did not span the range of physiologic flow values, only rest flows. Thus future work on MBF quantification with factor analysis should include calibration of the extraction function to a standard measured over the full physiologic flow range.

The mean MBF values did not differ significantly between MSO and MB derived factors (p=0.22 and p=0.15 without and with RV blood respectively). This may be explained by the blood factors differing primarily in shape, which is accounted for by the washout parameter k_2, while K_1 (and MBF) are mostly dependent on the scale of the blood factor relative to the myocardium TAC, and which were similar for both MSO and MB scaled blood factors (not shown).

The variance of MBF values using MB tended (p=0.15) to be less than with MSO (CV=10% vs. 18% respectively). The lack of statistical significance may be partially due to the small number of measurements (n=10) in a single animal.

Calibration of the extraction function to a standard is likely to result in similar MBF accuracy between ROI, MSO or MB methods. However, MB is expected to have better precision which could benefit longitudinal follow-up studies to track disease progression or treatment efficacy.

5.5 Conclusion

Constraints must be placed on dynamic cardiac PET image decomposition in order to resolve physiologically accurate factors. Simulation and experimental data were used to compare the physiological accuracy of the MSO and MB methods. Factors and structures obtained using MB agreed with simulations significantly better than MSO. In experimental ^{82}Rb PET data MB agree better than MSO with the physiological standards of arterial blood sampling. In addition, MB had more reproducible structure images and tended towards more reproducible global myocardial blood flow measurements with varying tracer infusion durations. The potential benefit of model-based factor analysis for quantification of myocardial blood flow should be explored in future validation studies.

Chapter 6.

MBF Quantification Using FA

In the previous chapter model-based factor analysis was demonstrated as a physiologically accurate method for decomposing dynamic ^{82}Rb PET image sequences. This chapter develops a method to quantify MBF using the FA results. MBF results are validated against MBF from ^{15}O-water PET imaging. FA derived MBF is also compared with the ROI derived MBF which was described in Chapter 3, and with a previously proposed spillover corrected method. A portion of this chapter has been published in [158].

The normal patient population Rb and Water PET images that are used in this study were provided by The School of Medicine at Hokkaido University, Sapporo, Japan.

6.1 Background

6.1.1 MBF Quantification using ^{82}Rb and Factor Analysis

Factor analysis has been sought as a complimentary method to kinetic modeling primarily in order to derive physiologically accurate blood input functions that are free of noise and signal contamination from neighbouring organs [72,75,106,127]. However, the spatial relationship of the structures has largely been neglected.

6.1.1.1 Scaling of Factors and Structures

Typically with factor analysis, the blood input functions are estimated as the LV blood factor which is scaled to image units using highest intensity pixels in the LV blood structure. The exact number of pixels and their location varies between methods, but in general a trade-off exists between minimizing the number of pixels to avoid recovery loss, due to finite spatial resolution, and increasing the number of pixels to average out noise. Regardless, this approach assumes that the scaling pixels are pure blood, and do not suffer from recovery losses [72,75,106,127]. However, signal mixing, which also results in reduced recovery, is one of the main reasons for pursuing factor analysis [107,108,120]. The decomposed components, although free of spillover contaminations still suffer of recovery loss, since the structures have the same finite spatial resolution as the original image.

In this chapter, an alternative scaling method is proposed, which scales all the structures simultaneously based on an estimated image of the <u>total</u> recovery (TR). It is assumed that the heart is sufficiently large relative to the spatial resolution of the image, and that the TR near the center of the heart approaches unity (i.e. no recovery loss exists). Assuming that the image is entirely decomposed (the residue consisting entirely of random noise), the TR image may be used to scale the structures to recovery coefficient (RC) of the

respective components. The factors, in turn, can be scaled into pure tissue activity concentrations.

6.1.1.2 Blood Input Functions

Cardiac images that are decomposed into two factors are expected to contain a blood and myocardium factor, and the blood factor is used as the input function of the kinetic model [75]. In images that are decomposed into three (or more) factors, RV blood and an LV blood factor are expected and the LV blood factor is used as the input function of the kinetic model [72,102,106,110,159]. RV and LV blood structures are assumed to be spatially separated and that the activity in each is uniformly distributed.

6.1.1.3 Myocardium Output Functions

While it may be tempting to use the myocardium factor for the output function, it assumes a uniform temporal response throughout the myocardium; albeit with varying magnitude. Uniformity cannot be assumed, particularly in the presence of disease [8,137,138,160]. For this reason ROI defined output functions are still used with factor analysis [72,102,106,110,159], even though they may contain more noise. Despite this limitation, myocardial factors have been used to quantify global MBF in small animals [75].

6.1.1.4 RV Blood Spillover Model

Spillover of RV blood signal in the septal region can be accounted for in the myocardial model, but requires a reliable and sufficiently large ROI for RV blood sampling. In addition, the stability of the myocardium model may be jeopardized by adding additional free parameters [48]. With factor analysis, a reliable RV blood TAC may be obtainable and enough noise may be removed to enable modeling of the RV spillover [72,106].

6.1.2 MBF Quantification using [82]Rb and Spillover Correction

A method to correct spillover contamination of the ROI derived blood TAC has been reported in the literature [54,58,81,161,162,163] as an alternative to factor analysis. A pair of signal mixing equations is defined. The equations describe mixing of pure blood and pure myocardium signals in the blood and myocardium TACs. Physiologic constraints are included to enforce a unique solution to the set of equations. A pure blood TAC that is free of recovery loss is estimated and used as the input to the tracer kinetic model. In addition, a global estimate of the myocardium RC can be obtained.

6.1.3 Accuracy Validation

Due to its ideal tracer kinetics, ^{15}O-water PET is considered the gold-standard for non-invasive MBF quantification, and it has been validated extensively [75,164,165,166]. Because water diffuses freely to all perfused tissues of the body, an anatomical image of the myocardium which could be used to register ROIs does not exist. This limitation has been

addressed either through blood pool imaging with additional tracers [58], subtraction of normalized early time frame images from normalized late time frame images to create a myocardium image [159,167], or by using myocardium structures from image decomposition [79]. Image decomposition is preferable for this application since it does not require additional imaging of the patient, thus reducing radiation exposure, simplifying the imaging protocol, and minimizing the chance of image misalignment due to patient motion.

In the following section MBF quantification with ^{15}O-water PET and factor analysis is used to evaluate the accuracy of MBF quantification with ^{82}Rb PET. The ROI-based method described in Chapter 3, a spillover correction based method, and two FA-based methods for ^{82}Rb-MBF quantification are compared.

6.2 Methods

6.2.1   Evaluation of MBF Accuracy

6.2.1.1   Study Population

All participants (n=20) had a low pre-test likelihood of CAD (<5%) based on risk-factors, had a normal resting electrocardiogram and did not have any cardiac medications. Each subject underwent rest, stress, and cold pressor test (CPT) imaging with both ^{15}O-water and ^{82}Rb PET. The ^{15}O-water and ^{82}Rb imaging were performed in a randomized order, 18±13 days apart. There was no significant difference in rest hemodynamics between the ^{15}O-water and ^{82}Rb studies (data not shown). The study was approved by the Hokkaido University Graduate School of Medicine Human Research Ethics Board. Written informed consent was obtained from all participants.

Participants were instructed to fast for at least 6 hours, to refrain from smoking for at least 12 hours, and to abstain from caffeine-containing products for at least 24 hours prior to PET studies [5,168,169]

6.2.1.2   PET acquisition protocol

Participants were positioned in a whole body PET scanner (ECAT HR+, Siemens/CTI, Knoxville, Tennessee). A 6-minute transmission scan was performed for attenuation correction followed by a dynamic emission at rest, adenosine stress, and CPT states in the 2-dimensional acquisition mode. During the entire protocol, symptoms, heart rate, blood pressure, and the electrocardiogram were monitored continuously.

6.2.1.2.1   Water Imaging

Immediately following the transmission scan, participants inhaled 2000 MBq of ^{15}O-labelled CO (0.14% CO mixed with room air) for 1 minute to obtain a blood volume image [5,170]. In this work the CO images were not used. Approximately 10 min later 1500 MBq of ^{15}O labelled water was administered intravenously over a 2 minute interval at rest and a

24-frame dynamic PET acquisition was initiated with varying frame duration (18×10 s, 6×30 s, total = 6 min) [5,170].

Cardiac stress was induced using Adenosine (0.14mg/kg/min) over 9 min and water infusion and imaging were repeated at 3 min. The same dynamic image acquisition used in rest was repeated. Sufficient time was allotted for radioactive decay of ^{15}O-water and return to baseline heart rate and blood pressure and a transmission scan was repeated.

The participant's foot (randomly selected [169]) was immersed into ice water up to the ankle [5,168,169]. PET data acquisition started 60 seconds after the beginning of CPT using the same dynamic sequence as used for rest and stress states. The CPT continued for a total of 4 minutes [168,170].

6.2.1.2.2 ^{82}Rb Imaging

A similar rest, stress, and CPT imaging protocol was performed with ^{82}Rb, except that CO imaging was not performed. Immediately following the transmission scan, 1,480 MBq of ^{82}Rb (Bracco Diagnosis, Princeton, NJ) was administered intravenously over one minute [81]. A 10 minute, 17-frame dynamic scan was initiated with increasing frame durations (12×10 s, 2×30 s, 1×60 s, 1×120 s, 1×240 s) [39,81]. To avoid adaptation, the CPT measurement was performed with immersion of the opposite foot as with ^{15}O-water.

6.2.1.3   Water Image Processing

To obtain an uptake image with good contrast between the myocardium and the surrounding tissues, each image was decomposed using FADS [75,131] followed by oblique rotation of the factors to minimize spatial overlap between structures [106,124]. The myocardium structure was automatically identified based on the temporal profiles of all factors, and criterion of low activity concentration in early time frames relative to late time frames. The myocardium structure was used to reorient the volume and define myocardial and LV blood cavity ROIs as described in Chapter 3 (section 3.2). The myocardium was sampled in 16 rings each having 36 sectors, totalling 576 segments. The ROIs were applied to all dynamic frames to sample arterial blood input functions $C_b(t)$ and myocardial output functions $C_t(t)$.

The image derived blood TAC, $C_b(t)$, was corrected for myocardial to blood pool spillover using established ROI-based methods [58,162]. $C_b(t)$ was modeled as a mixture of β=85% pure arterial blood signal, $C_a(t)$, with spillover (1-β=15%) from pure tissue signal, $C_t(t)$, as shown in 6-1. The blood recovery, β, was determined experimentally for humans using CO blood imaging and the measured activity concentration in blood samples [58].

$$C_b(t) = \beta \cdot C_a(t) + (1 - \beta) \cdot C_t(t)$$ **6-1**

Likewise sampled activity concentrations in the myocardium, $C_m(t)$, were modelled using a spillover model of pure blood and tissue, as shown in equation 6-2, where *TR=RC+TBF* [0-1] is the total recovery of tissue and blood in the myocardium ROI.

$$C_m(t) = TBF \cdot C_a(t) + RC \cdot C_t(t) = TBF \cdot C_a(t) + (TR - TBF) \cdot C_t(t) \qquad \textbf{6-2}$$

A water-specific one-tissue-compartment kinetic model was used to model tissue activity, $C_t(t)$, as a function of myocardial blood flow, MBF_{H2O}, as shown in equation 6-3, where $\lambda = 0.91$ [58,171,172] is the partition coefficient of water in the myocardial tissue and $\rho = 1.04$ g/mL is the density of tissue [58,171,172].

$$C_t(t) = \rho \cdot C_a(t) \otimes MBF_{H2O} e^{-(MBF_{H2O}/\lambda) \cdot t} \qquad \textbf{6-3}$$

In equation 6-1, $C_a(t)$ was isolated and substituted into equation 6-2 which was then fit to the sampled global myocardium TAC by solving for *TBF*, *TR*, and MBF_{H2O} simultaneously.

Regional MBF_{H2O} was then estimated using the pure blood, $C_a(t)$, as the arterial blood input function instead of the sampled blood TAC, $C_b(t)$. The regional sampled myocardium TACs were modeled using equation 6-2 and 6-3. The *TBF* and *TR* were optimized together with MBF_{H2O} to minimize the error of the measured and modeled myocardial TAC ($C_m(t)$).

6.2.1.4   [82]Rb Image Processing

Images were manually cropped to include the entire heart and remove other high uptake organs such as stomach. The cropped image was summed across all time frames and thresholded to 30% maximum pixel intensity. A 3D flooding algorithm was seeded at the pixel of maximum intensity and was used to define a single continuous ROI encompassing the heart.

The dixels in the ROI were then decomposed using the model-based factor analysis algorithm described in the previous chapter into 3 factors (RV blood, LV blood, and myocardium). The factors were then applied to the entire image field-of-view to resolve corresponding structures.

Since the myocardium structure has equal or better contrast than the uptake image of [82]Rb and less noise, it was used to automatically reorient the volumes and to define blood pool and myocardium ROIs. Reorientation and segmentation employed the same methods used for the water images (described in chapter 3). The ROIs could then be applied to the dynamic image sequence, or to the structures. Four methods for MBF quantification using [82]Rb PET were evaluated as listed in Table 6-1 and compared to the standard ^{15}O-water PET method.

TABLE 6-1 – KINETIC MODEL INPUT AND OUTPUT FUNCTION COMBINATIONS

Tracer	Method	Input function	Output function	RC
[15]O-water		Image Derived-SOC	Image Derived	*RC*
[82]Rb	IDF	Image Derived	Image Derived	1-*TBF*
	SOC	Image Derived-SOC	Image Derived	1-*TBF*
	FA	Total Blood Factors	Image Derived	1-*TBF*
	FARV	Total Blood Factors+RV Factor	Image Derived	1-*RVBF-LVBF*

6.2.1.4.1 Quantification Using Image Derived Input Functions (IDF)

The myocardium and blood cavity ROIs were used to sample the dynamic image sequence to derive myocardial output, $C_m(t)$, and arterial blood input, $C_a(t)=C_b(t)$, TACs. A one tissue compartment kinetic model was solved with a geometric recovery correction [56] which accounts for the mixing of blood (*TBF*) and myocardial (*1-TBF*) signals as in Chapter 3 and reiterated in equation 6-4.

$$C_m(t) = TBF \cdot C_a(t) + (1 - TBF) \cdot C_t(t)$$
$$= TBF \cdot C_a(t) + (1 - TBF) \cdot \rho \cdot C_a(t) \otimes K_1 e^{-k_2 \cdot t} \qquad \textbf{6-4}$$

6.2.1.4.2 Quantification Using Spillover Correction (SOC)

Similarly to ^{15}O-water, contamination of the blood signal from myocardial spillover was corrected (SOC). The blood pool and myocardial signals were modeled using equations 6-5 and 6-6, and these equations were combined by isolating $C_a(t)$ in equation 6-6 and substituting into equation 6-4.

$$C_m(t) = TBF \cdot C_a(t) + (TR - TBF) \cdot C_t(t)$$
$$= TBF \cdot C_a(t) + (TR - TBF) \cdot \rho \cdot C_a(t) \otimes K_1 e^{-k_2 \cdot t} \qquad \textbf{6-5}$$

$$C_b(t) = \beta \cdot C_a(t) + (1 - \beta) \cdot C_t(t)$$
$$= \beta \cdot C_a(t) + (1 - \beta) \cdot \rho \cdot C_a(t) \otimes K_1 e^{-k_2 \cdot t} \qquad \textbf{6-6}$$

The cost function shown in equations 6-7, 6-8, and 6-9 was minimized by optimizing *TBF*, *TR*, β, K_1, and k_2 using whole-LV average $C_m(t)$. Equation 6-7 penalizes for the magnitude of error between sampled and modelled myocardial and blood TACs, for negative values in the pure tissue and pure arterial blood TACs, $C_t(t)$ and $C_a(t)$ respectively ($W_{neg}=10^6$). It also penalizes for residual blood activity in the last time frame, *T* ($W_{blood\_residual}=5$). The weighting vector, $w(t)$, was set to the duration of the imaging time frames.

$$C = \left[\left\| w(t) \cdot \left(C_m(t) - C_m{}'(t) \right) \right\| + \left\| w(t) \cdot \left(C_b(t) - C_b{}'(t) \right) \right\| \right] \times$$

$$\left[1 + W_{neg} \sqrt{ \left\| w(t) \cdot H\left(C_t(t) \right) \right\|^2 + \left\| w(t) \cdot H\left(C_a(t) \right) \right\|^2 } + \right. \qquad \textbf{6-7}$$

$$Wblood\_residual \cdot Cblood\_residual$$

$$H\left(x(t) \right) = \begin{cases} 0 & x \geq 0 \\ x & x < 0 \end{cases} \qquad \textbf{6-8}$$

$$C_{blood\_residual} = \frac{w(T) \cdot C_a(T)}{\sum_{t=1}^{T} w(t) C_a(t)} \qquad \textbf{6-9}$$

The pure arterial blood TAC, $C_a(t)$, was used as the blood input function to the kinetic model (equation 6-4).

6.2.1.4.3 Quantification Using Factor Analysis

MB derived structures and factors were scaled, blood input functions were generated from the scaled factors, and tracer kinetic modeling was performed to quantify uptake rates. The ROI sampled myocardial TACs were used as output function for tracer kinetic modelling.

Scaling of Factors and Structures

A map of the total recovery, TR^0, was created using the reorientation and LV segmentation data. The mid-myocardial contour was shifted radially outward in the septal wall region to include some of the RV. A mask containing all pixels enclosed by the contour was then generated as demonstrated in Figure 6-1 top-left. The mask was then smoothed to the same resolution as the image, resulting in an estimate of the TR due to anatomy and image resolution, but neglecting motion. Since motion blur is not accounted for and the recovery contribution of the right chambers is estimated grossly, only a subset of pixels, p, corresponding to TR^0 above a threshold ($TRco$) was included (Figure 6-1 top-right).
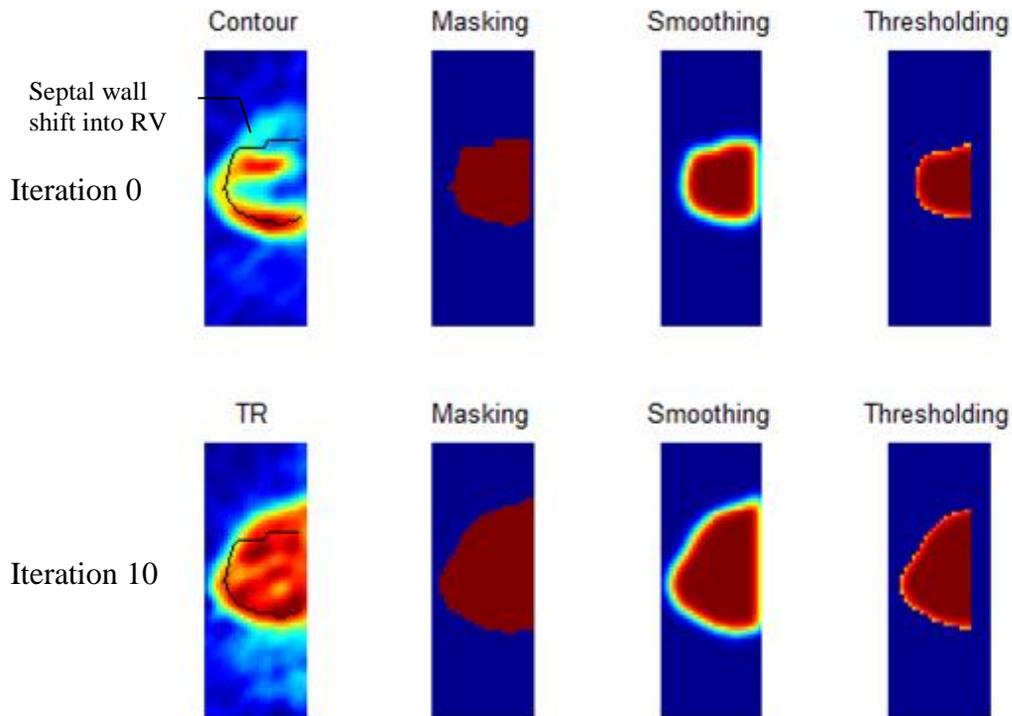
Figure 6-1 – Estimation of TR image using LV myocardium contours.

The scale of each structure, a_k where $k=1..K$, ($K=3$ in this chapter) was optimized to minimize the summed squared differences between scaled structures and TR in each pixel, p, as shown in the first part of equation 6-10. The second part of equation 6-10 penalizes for pixels having $TR>1$.

$$(a_k, k = 1..K) = \min_{a_k} \sum_p \left[TR_p^i - \sum_{k=1}^K a_k S_{k,p} \right]^2 + \sum_p H \left(\sum_{k=1}^K a_k S_{k,p} \right)^2 \qquad \textbf{6-10}$$

$$H(x) = \begin{cases} x - 1, & x > 1 \\ 0, & x \le 1 \end{cases} \qquad \textbf{6-11}$$

To overcome inaccuracies resulting from neglect of the right cavities of the heart, a new TR^i image was estimated by summing the scaled structures (Figure 6-1 bottom-left), generating a mask of all pixels $TR > 50\%$ to detect the edges, and blurring the mask to the original image resolution. Once again the scales, a_k, were optimized for a subset of pixels $TR^i > TRco$ (Figure 6-1 bottom-right) to avoid inaccuracies near the edges of the heart. This process was iteratively repeated 10 times to refine the estimate of TR and the scaling parameters, a_k.
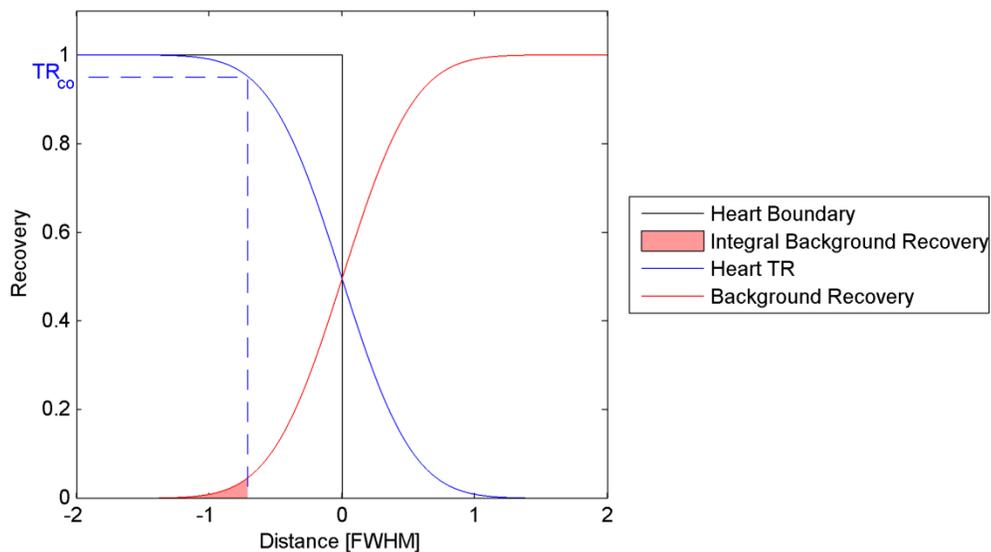
Figure 6-2 – Heart TR without (black) and with Gaussian smoothing (blue) and background activity recovery (red) as a function of distance from the edge of the heart. The TR cut-off (TR_{co}) can be adjusted to reject regions close to the myocardium edge so as to reduce recovery loss and background signal spillover in the structure scaling process (left of dashed blue line).

The TR cut-off (TR_{CO}) can be adjusted to include varying amounts of the heart region in the scaling process. When $TR_{CO} \approx 50\%$ the entire heart region is used, since the edge of the mask approximates the edge of the heart. Values of TR_{CO} which are smaller than 50% include regions outside of the heart and are expected to be more inaccurate since the estimation of TR in these regions neglects background activity from other organs. TR estimates at the center of the heart (TR_{CO} approaches 100%) are expected to be most accurate, but may result in small regions with insufficient mixing ratios between structures to ensure a robust solution. In this work $TR_{CO} = 95\%$, which results in a small reduction in recovery or contamination from background activity as demonstrated in Figure 6-2.

The inverse scaling was applied to respective factors to preserve the original image units. Subsequently structures were in units of recovery coefficient, between 0 and 1, and factors were in image units [Bq/cc] representing the activity of a pure physiologic signal with complete recovery (no recovery loss).

Arterial Blood Input Functions

The scaled LV blood factor was assumed to be physiologically accurate (as is common in the literature [72,102,106,110,159]) and a fully recovered free measure of the arterial blood input function and was labelled $C_a^{FA}(t)$.

Myocardial Models

Two models of the myocardial sample TACs were developed, without and with inclusion of RV blood spillover into the myocardial region. In both cases $C_a(t) = C_a^{FA}(t)$ was used as the blood input function.

1) Factor Analysis without Right Ventricle Blood Spillover (FA)

The same kinetic model used in the ROI based method (equation 6-4) was used.

2) Factor Analysis with Right Ventricle Blood Spillover (FARV)

RV blood spillover into the myocardium region, *RVBF*, was included in the model of the myocardium. The Geometric-model estimation of RC was expanded to include separate RV and LV blood contribution [72] (RVBF and LVBF respectively) as shown in equation 6-12. For simplicity, the RV blood contribution was included in the entire polar-map region (as opposed to the septal region only [90]). The recovery corrected RV blood factor was used for the RV blood TAC, $C_r(t)$.

$$
\begin{aligned}
C_m(t) &= RVBF \cdot C_r(t) + LVBF \cdot C_a(t) + (1 - RVBF - LVBF) \cdot C_t(t) \\
&= RVBF \cdot C_r(t) + LVBF \cdot C_a(t) + \\
&\qquad (1 - RVBF - LVBF) \cdot \rho \cdot C_a(t) \otimes K_1 e^{-k_2 \cdot t}
\end{aligned}
\tag{6-12}
$$

6.2.1.5 *Extraction Fraction Calibration*

A flow dependent extraction fraction relating K_1 and MBF_{Rb} as described by a generalized Renkin-Crone model [29,30] was used as reiterated in equation 6-13. The extraction fraction was calibrated (optimizing parameters *a* and *b*) by minimizing the squared error between extraction corrected $K_{1,i}$ values and $MBF_{H2O,i}$ values as shown in equation 6-14, where *i* denotes an image number. For each combination of water and Rb quantification methods, the extraction function was calibrated using global (average of all 576 polar-map segments) K_1 and MBF_{H2O} values. The respective extraction function parameters were then applied to convert K_1 values to MBF_{Rb} values using equation 6-13.

$$
K_1 = (1 - ae^{-b/MBF_{Rb}})MBF_{Rb}
\tag{6-13}
$$

$$
(a, b) = \min_{a,b} \sum_i \left[MBF_{H2O_i} \left(1 - ae^{-\frac{b}{MBF_{H2O_i}}} \right) - K_{1_i} \right]^2
\tag{6-14}
$$

6.2.1.6   Regional Blood Flow

MBF values were reported for the three vascular territories by segmenting the polar-maps into 17 segments and then averaging the segments in each territory corresponding to the left anterior descending artery (LAD), left circumflex artery (LCX, and right coronary artery (RCA) as described in the ASNC guidelines [46].

6.2.1.7   Comparison with ^{15}O-Water

Rb-derived MBF values were compared with water MBF values. Both global MBF values and regional MBF values of the three vascular territories were analyzed.

6.2.1.8   Polar-map Uniformity

Uniformity of MBF throughout the polar-maps is expected in healthy populations as in this study. Polar-map MBF uniformity was reported as the percent standard-deviation to mean ratio, also referred to as the percent coefficient of variation (CV%). For each MBF quantification method the mean CV% across all subjects were reported for rest, stress, CPT, and all images combined.

6.2.2   Evaluation of MBF in a Patient Population

Images from 30 clinical patients that had undergone a standard rest-stress diagnostic ^{82}Rb PET exam (same population as in Chapter 3) were processed using the same ^{82}Rb MBF quantification methods described above. Since the images were acquired on a different scanner a previously reported extraction function [39] was used. The uniformity of the polarmaps was evaluated.

6.2.3   Statistical Analysis

Rb-derived MBF values were compared with water MBF values using correlation and Bland–Altman analyses [136]. Correlation was reported using a Pearson correlation coefficient, r, and agreement was reported using the coefficient of reproducibility, CR, which is equal to 1.96 times the standard-deviation of the error between MBF_{H2O} and MBF_{Rb}.

Differences in population means were tested using a student t-test, and CV% and CR differences were tested using an f-test, assuming a Gaussian distribution which was not tested. Significant differences in Pearson correlation coefficients were evaluated using the Fisher transform. Differences between average spillover corrections (β) were calculated using a Wilcoxon non-parametric test.

Repeat significance tests across the four Rb MBF quantification methods included a Bonferroni correction of 4. When water data were also compared, a Bonferroni correction of 5 was applied. Differences were considered significant for p-values less than 0.05.

6.3 Results

In all ^{82}Rb images decomposition achieved good quality myocardial structures on which reorientation and segmentation could be conducted. In 1/60 normal and 18/60 patient images, high stomach activity required manual intervention at the reorientation stage, which was limited to adjusting the transaxial slice in all but 11 cases. Respectively, in 0/60 and 4/60 cases manual intervention was required at the segmentation stage as well.

In ~13/60 images, myocardium structures generated from decomposed (FADS with MSO) water images had poor contrast for reorientation and segmentation. Manual intervention was required during 22/60 reorientations and 10/60 segmentations.

6.3.1   Normal Population

6.3.1.1   Extraction Fractions

The extraction function parameters, *a* and *b*, are listed in Table 6-2 and vary with Rb-MBF quantification methods. However, as shown in Figure 6-3, the extraction functions for Rb-IDF and Rb-SOC (green lines) are nearly identical to previously reported extraction functions by the same group that acquired these data [55,81]. The Rb-FA and Rb-FARV extraction functions (blue) had lower extraction values.
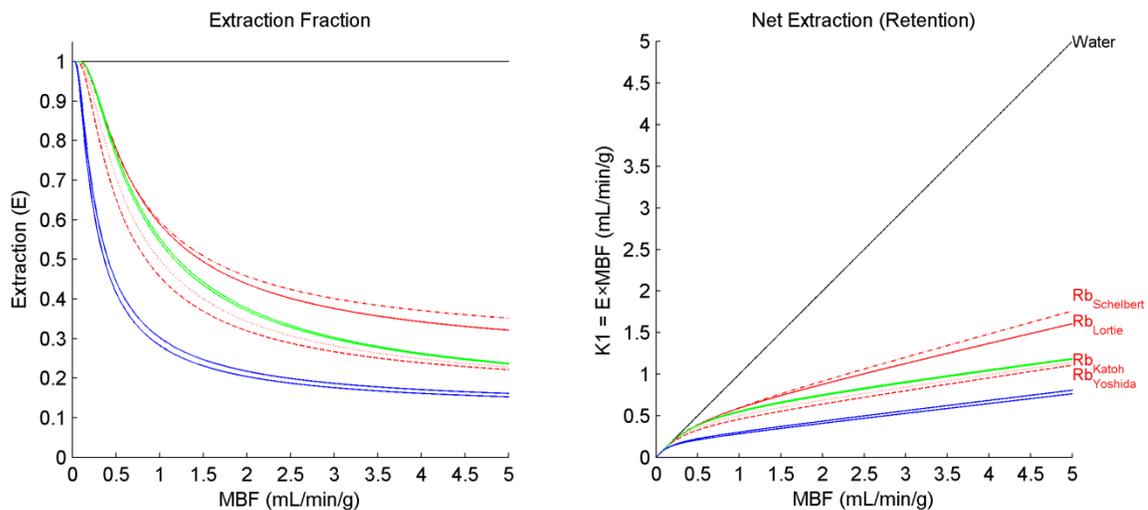
Figure 6-3 – Previously reported (red) ^{82}Rb extraction fractions (left) and corresponding net extractions (right) (references in Table 2-2). The green lines are Rb-IDF and Rb-SOC extraction fractions calibrated to the water-MBF data as shown in Table 6-2. The blue are Rb-FA and Rb-FARV extraction fractions.

TABLE 6-2 – EXTRACTION FUNCTION PARAMETERS AND ACCURACY OF MBF

	Rb method	**Extraction Fraction**		**Correlation & Agreement with water-MBF**			
		a	*b*	*r*	**Slope**	**Intercept**	**CR**
Water-SOC	IDF	0.87	0.67	0.70	0.98	0.23	2.46
	SOC	0.87	0.65	0.70	0.98	0.21	2.46
	FA	0.88	0.21	0.77	0.98	0.09	2.02
	FARV	0.88	0.23	0.74	0.98	0.10	2.24

6.3.1.2   Flow Values

Global MBF values at rest, stress, and CPT are shown in Figure 6-4 for all quantification methods. No significant differences were detected with the exception of FA rest MBF, indicating that the extraction functions were calibrated successfully.
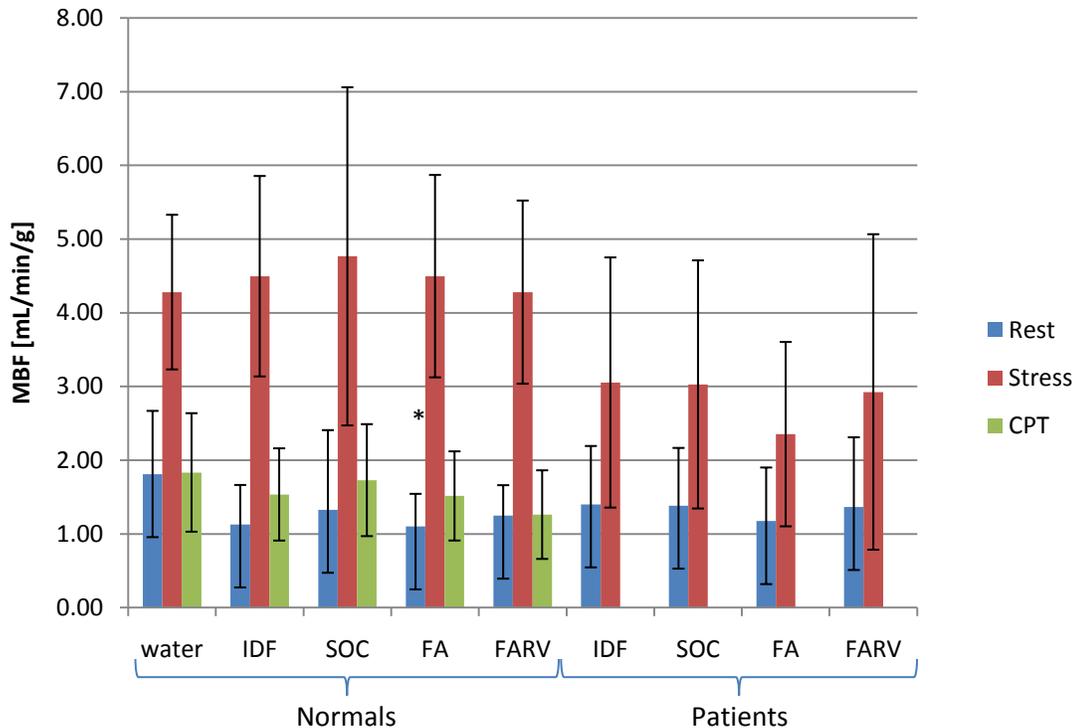
Figure 6-4 – Mean ± one standard-deviation global MBF of all normals (n=20) and all patients (n=30) at rest, stress, and CPT using all quantification methods. * indicate significant differences in MBF compared to water.

6.3.1.3   Accuracy

Agreement parameters of Rb and water derived MBF values are shown in the right half of Table 6-2 and also in the correlation and Bland-Altman plots in Figure 6-5. All linear regression slopes were within 2% of unity, and the intercepts were between 0.09 mL/min/g for Rb-FA and Rb-FARV and 0.23 mL/min/g using Rb-IDF.

Pearson correlation coefficients (r) and coefficients of reproducibility (CR) are graphed in Figure 6-6 for comparison. No significant differences were reported between any two sets of data, although FA values were more favourable (higher r and lower CR). Inclusion of RV in the myocardium TAC model did not result in significant differences (FA vs. FARV) in either r (p=0.67) or CR (p=0.42). Likewise, spillover correction (Rb-SOC) did not significantly improve agreement with water compared to Rb-IDF (p=ns. for both r and CR).
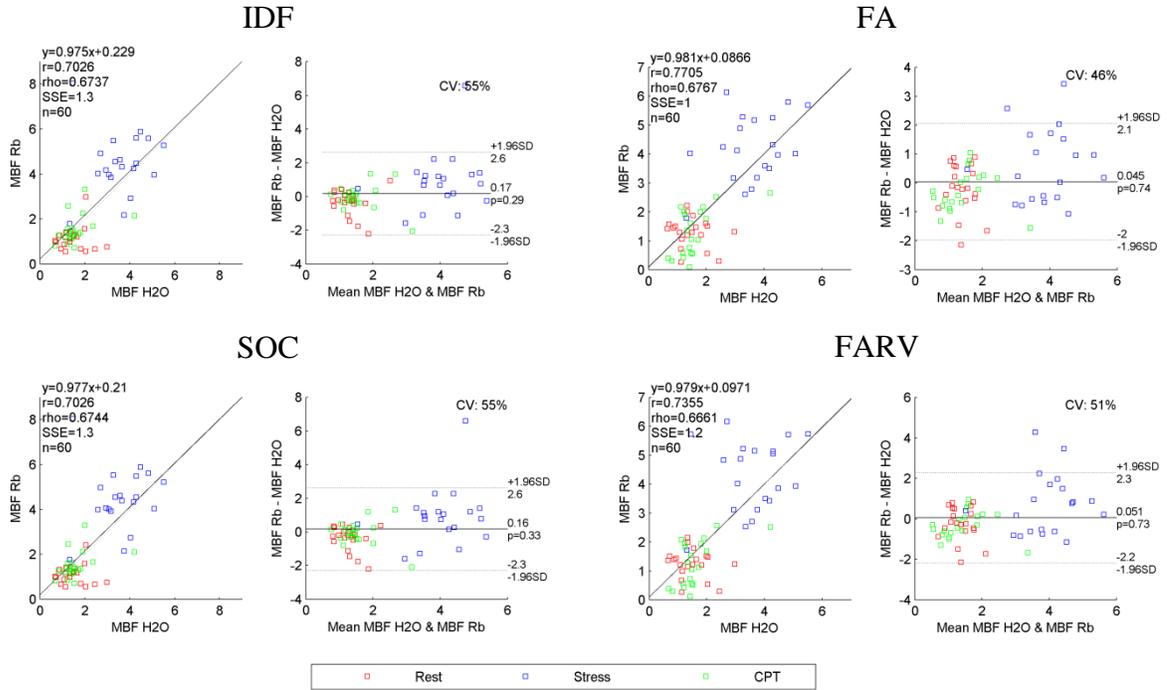
Figure 6-5 – Correlation and Bland-Altman graphs of MBF with Rb compared to water.
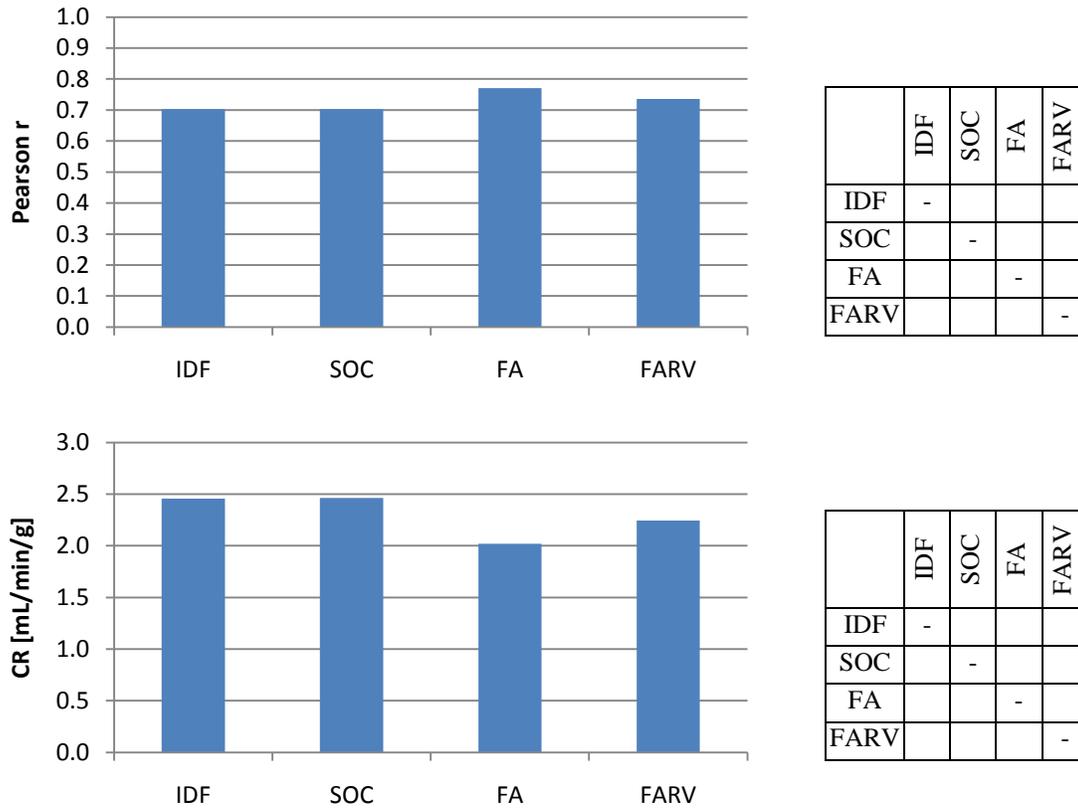
Figure 6-6 – Pearson correlation coefficient (r) (top) and coefficient of reproducibility (CR) (bottom) of MBF values between Rb and water. The tables on the right indicate significant differences (*) between methods. No significant differences in r or CR were found between methods.

With all Rb methods mean biases, as measured with Bland-Altman analysis, did not significantly differ from zero, as expected due to calibration of the extraction functions for each dataset.

6.3.1.4   Polar-map Uniformity

The mean coefficients of variation across all polar-maps are plotted in Figure 6-7 (in red for normals) along with a table of significant differences. The lowest polar-map non-uniformities were achieved using the Rb-FA and Rb-FARV methods which had less than half the variability of either Rb-IDF or Rb-SOC (p<0.001 for all combinations). Rb-IDF had the highest non-uniformity in the group but was not significantly greater than Rb-SOC or water (p=0.70 and p=0.08 respectively). Inclusion of the RV spillover in the myocardium model (FA v.s. FARV) did not significantly change the uniformity of the polar-maps (p=0.65).

	Water	IDF	SOC	FA	FARV
Water	-	na	na	na	na
IDF		-			
SOC			-		
FA	†	†	†	-	
FARV	†	†	†		-

* - p<0.05   † - p<0.001
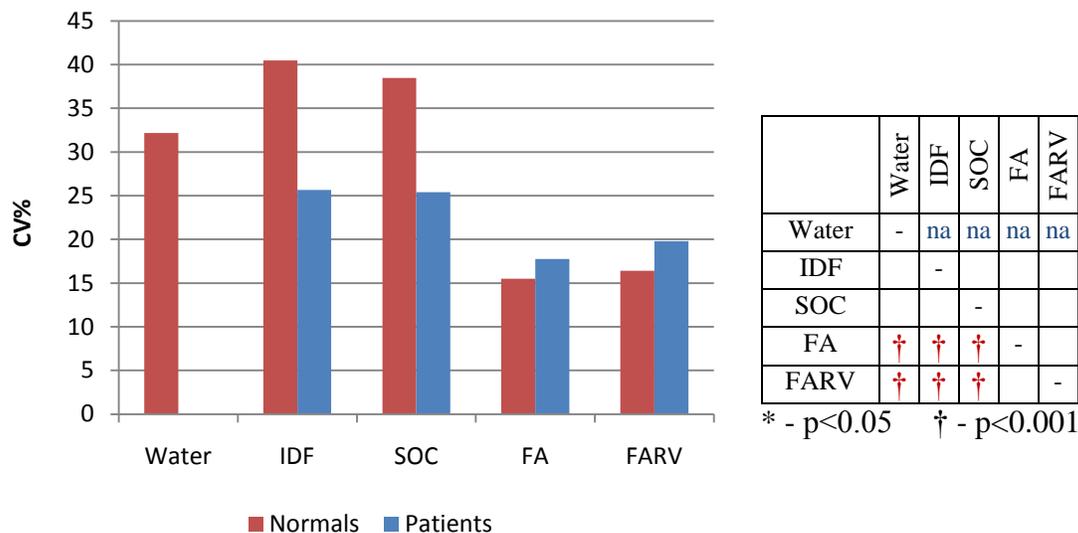
Figure 6-7 – Mean of coefficient of variation (CV%) of MBF polar-maps for normals and patients as measures of average polar-map uniformity. Significant differences between methods are indicated in the table (right) in red and blue corresponding to normal and patient datasets. Factor analysis based methods generated significantly more uniform polar-maps than ROI based methods. Differences between populations using the same method were not significant.

Global CV% at rest, CPT, and stress states are shown in Figure 6-8. Interestingly in all methods rest-CV% and CPT-CV% values were larger than stress-CV%, which may be related to the more non-linear extraction at low MBF, but none of these differences were significant (p=ns).
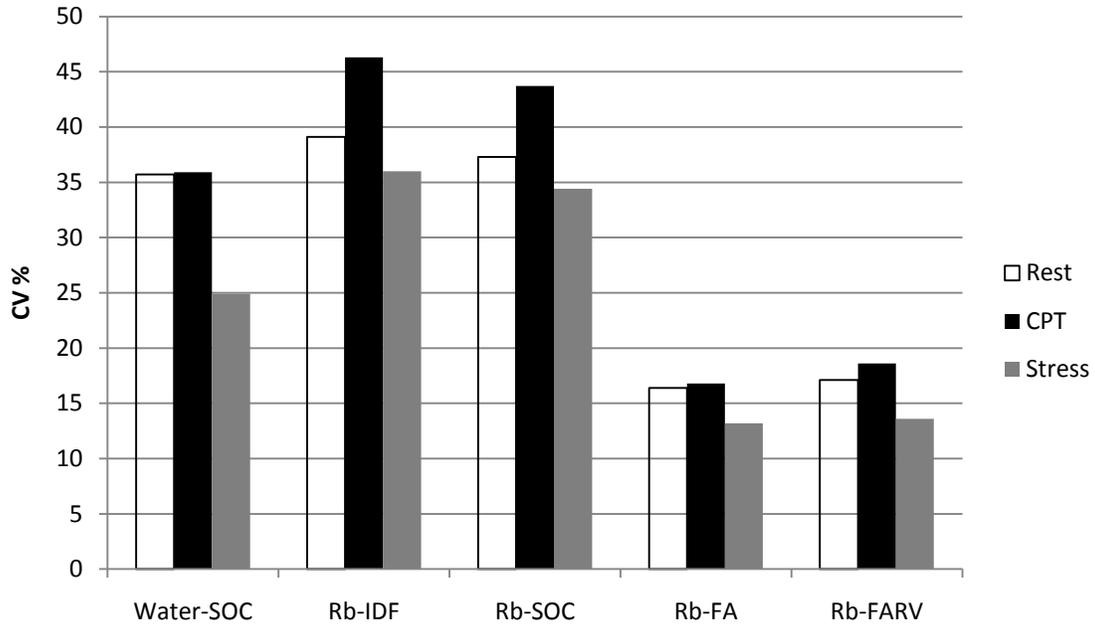
Figure 6-8 – Mean of coefficient of variation (CV%) of MBF polar-maps at rest, CPT, and stress. No significant differences were detected between rest, CPT, or stress.
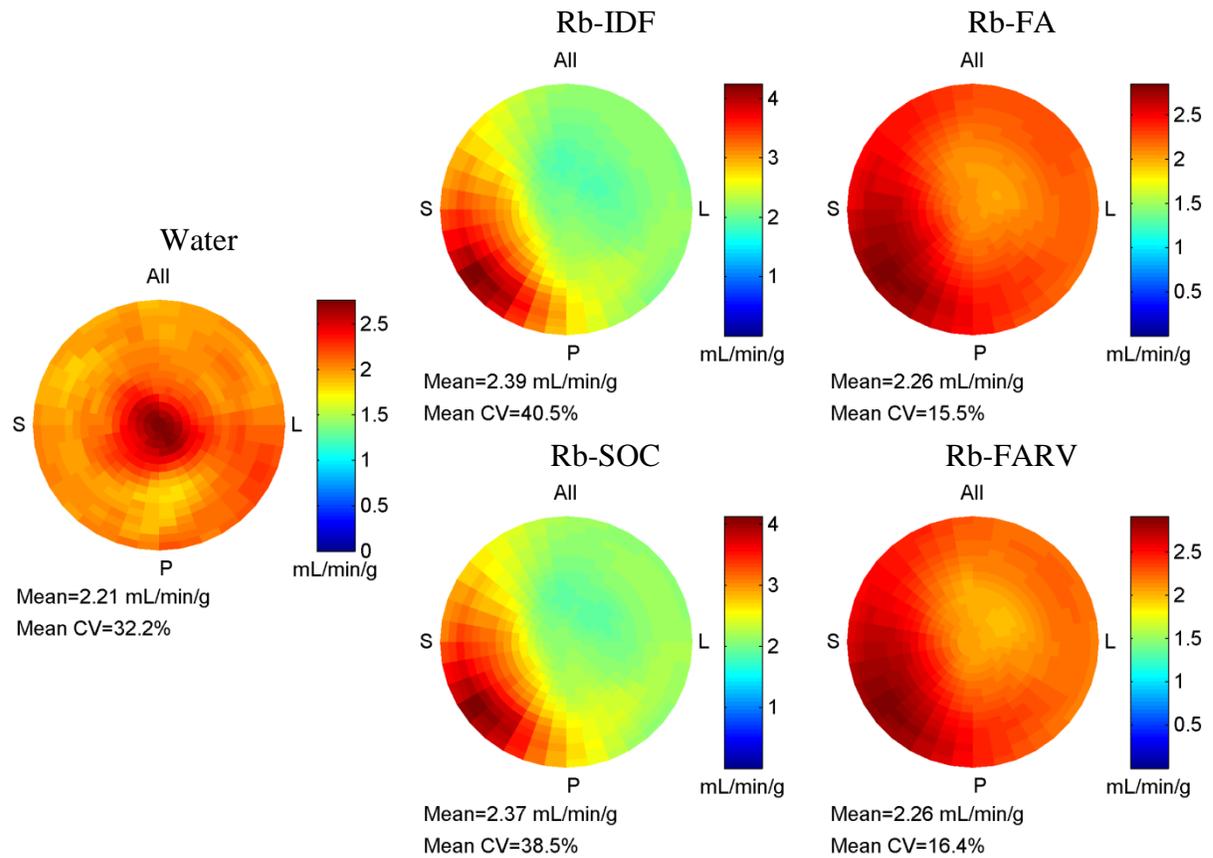
Figure 6-9 – Mean MBF polar-maps across all (n=60) images for each of the quantification methods.

Mean regional MBF polar-maps are shown in Figure 6-9 to demonstrate regional biases that would contribute to non-uniformity. The mean water-MBF polar-map was fairly uniform with slightly higher MBF in the apex region. The Rb-IDF and Rb-SOC methods both had higher MBF in the septal wall which may be due to unaccounted RV blood spillover. The Rb-FA method demonstrated the greatest degree of uniformity, but still had a slight increase (~20%) in the septal region, which was not resolved by including RV spillover in the model.

Regional uniformities (CV%) in the three vascular territories are plotted in Figure 6-10. In all cases uniformity was greatest (smallest CV%) in the LCX territory (lateral wall) compared to LAD ($p < 0.05$) and in ROI based methods also compared to RCA territories ($p < 0.05$). No statistically significance differences were found between territories with water.
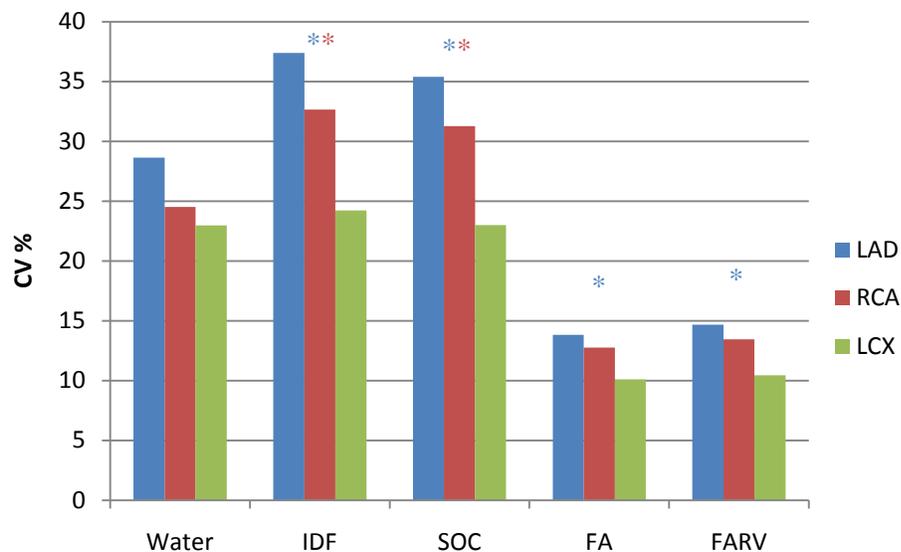
Figure 6-10 – MBF non-uniformity (CV%) in the three vascular territories using each MBF quantification method (average of all rest, stress, and CPT polar-map territories). Non-uniformity was significantly (*) higher in the LAD and RCA vs. LCX using all Rb methods but not with water.

6.3.2 Patient Population

Mean±std MBF values at rest and stress are plotted in Figure 6-4 for the patient population (n=30). There were no significant differences in average rest or stress MBF values between methods (p=ns). MBF rest values were higher than normally reported, indicating that the extraction fraction may not be accurately calibrated for this dataset. The variance of MBF values did not significantly differ between methods.

Polar-map uniformity measures (CV%) for all patients are shown in Figure 6-7 in blue. As in the normal population, CV% values were lower in both FA-based methods compared to ROI based methods, but were not significantly different ($0.13 < p < 0.3$ for all combinations). However, the variations in MBF values (error bars in Figure 6-4) indicates

that the dynamic range of MBF is not restricted with FA compared to ROI. The examples in Figure 6-11 and Figure 6-12 demonstrate that the FA polar-maps appear to maintain the spatial pattern of MBF vs. tracer uptake, as expected. Generally FA results agreed with uptake polar-maps more closely, which may suggest that IDF and SOC are less robust for regional estimates of MBF.
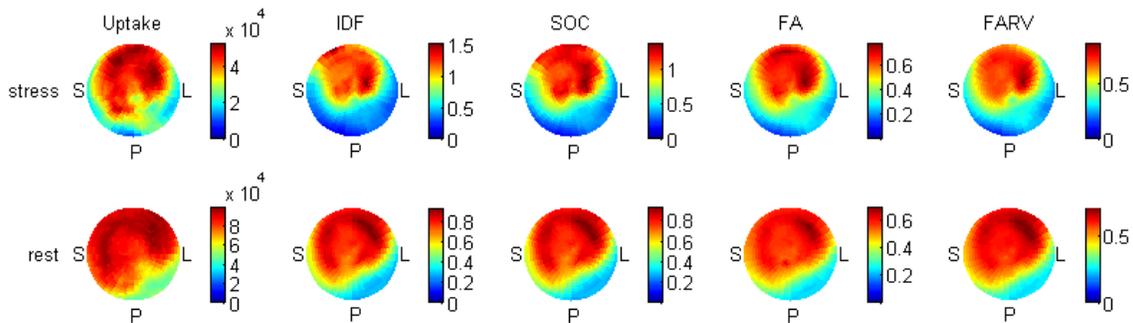
Figure 6-11 – Example with good correspondence between all quantification methods in a patient with reduced MBF in the septal, posterior, and lateral walls that worsens at stress, suggesting obstructed RCA and LCX arteries.
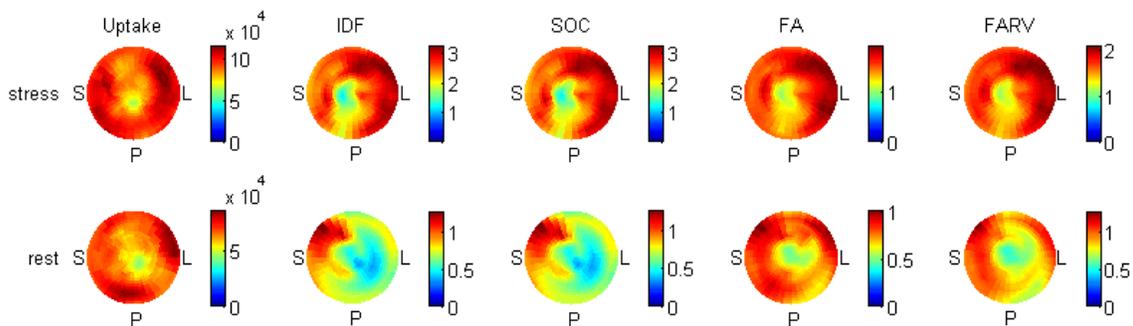
Figure 6-12 – Example of increased heterogeneity in MBF with ROI based methods compared to FA based methods. The FA based results correspond better with uptake images.

Polar-map uniformity values were surprisingly higher (lower CV%) in normal population compared to the patient population, with Rb-IDF and Rb-SOC although not significantly (p=ns). This may be due to the differences in PET cameras and the reconstruction algorithms.

6.4 Discussion:

Four different methods to quantify MBF from [82]Rb PET images were evaluated in this chapter. The findings are summarized in Table 6-3. The accuracy of MBF quantification with [82]Rb PET was evaluated using ^{15}O-water PET. Accuracy (r and CR) did not differ between methods. However, MBF quantification using FA did improve polar-map uniformity significantly in the normal population.

In the patient population, which included the presence of clinically reported CAD (Table 3-2) polar-map uniformity values were also higher using Rb-FA and Rb-FARV, but not significantly, likely due to the increased variability in physiologic flow. Visual inspection

of the MBF polar-maps confirmed that Rb-FA and Rb-FARV can resolve heterogeneous patterns, which indicates that the increased uniformity is not artificial. Thus Rb-FA and Rb-FARV may both be more sensitive to detecting true physiologic variations in MBF.

MBF uniformity in normals has been validated using microspheres [173] suggesting that the FA based methods are physiologically accurate. Mean MBF polar-maps (Figure 6-9) demonstrate biasing in the septal wall using the ROI based methods which may be related to uncorrected RV blood spillover into the myocardium ROI. The water polar-map seems to have slightly elevated MBF values in the apex regions, which may be due to the larger recovery loss in the apex region.

TABLE 6-3 – COMPARISON OF MBF QUANTIFICATION METHODS

Trait	ID	SOC	FA	FARV
Accuracy (compared to ^{15}O-water PET)	=	=	=	=
Uniformity in normals	↓	↓	↑	↑
Uniformity in patients	=	=	=	=
Processing speed	↑	↑	↓	↓

↑ – advantageous   = – equivalent to other methods

↓ – disadvantageous

6.4.1   Blood Spillover Correction

Addition of a myocardium to blood pool spillover correction to the ROI based method did not significantly change the results (correlation, agreement, MBF values, or CFR). The degree of spillover correction is inversely related to the blood pool recovery parameter, β, where $\beta = 1$ implies that no correction was performed. Respective β values for normals and patients were 0.980 ± 0.019 and 0.994 ± 0.016 (p<0.001 for mean and p=ns for variance). It is likely that the slightly greater correction in normals was attributed to smaller heart sizes (due to normal population and the smaller Japanese population) resulting in more spillover into the blood pool. However, the increased spillover may also be attributed to differences in scanner, reconstruction algorithms, and reconstruction parameters between the two datasets.

6.4.2   RV to Myocardium Spillover

Including RV blood spillover in the myocardium model with FA did not result in any significant changes (correlation, agreement, MBF values, or CFR). As the *RVBF* polar-maps for both normals and patients demonstrate (Figure 6-13) the average *RVBF* in the septal region was only ~6%. Assuming that *LVBF* is not greater than 50%, the recovery coefficient, $RC = (1 - LVBF - RVBF)$, which scales K_1, would vary on the order of 12%, or less. Variability of K_1 would decrease for smaller *LVBF* values, which are often assumed to be on the order of 30-40% [42].
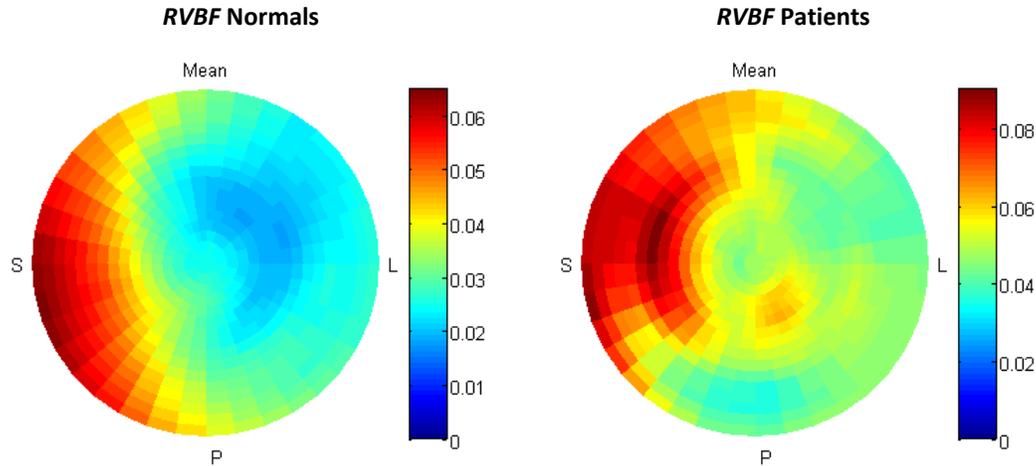
Figure 6-13 – Mean *RVBF* polar-map for all normals (right) and all patients (left) (n=60 for each).

Differences between normals and patients *RVBF* polar-maps can be attributed to a combination of differences in subject populations, instrumentation, reconstruction algorithms, and reconstruction parameters.

6.4.3 Myocardium Structures for ROI

While the ROI-based quantification method described in Chapter 3 used uptake images to determine the ROIs, in this chapter, myocardium structures were used, which were visually validated. Theoretically, shifting of myocardium ROIs radially outwards beyond the mid-myocardium (into the epicardium region) could result in lower *TBF* values, which would lead to higher *RC* values (1-*TBF*), and therefore lower K_1 and MBF values. In the septal region, due to the presence of RV blood which has a similar TAC to LV blood, shifting the myocardium ROI into the RV blood region could result in higher *TBF* values, lower *RC* values, and therefore increased MBF values. If this were the case, polar-map uniformity would decrease (higher CV%) and average flow values would increase, which corresponds with the results observed in this work for the IDF and SOC methods. The difference between ROIs derived from uptake and myocardium FA structures was not evaluated. However, shifting the myocardium ROIs radially inward by 2 mm did effect the results (MBF, accuracy, or polar-map uniformity) only slightly, indicating that the septal wall MBF derived with ROI-based methods may be biased due to physiologically inaccurate blood input functions.

6.4.4 Extraction Functions

The extractions for ROI-based MBF were within the range of previously reported [82]Rb extraction fractions (Figure 6-3 and Table 6-2), however the extraction fractions for the FA based methods were lower over the entire range of MBF values. While the *a* parameters were similar for all the quantification methods, *b* parameters were lower for FA based

methods than ROIs based methods. Physiologically, the results for FA based methods indicate lower baseline permeability x surface-area product, *PS* (ml/min/g), than previously reported using ROI based methods, but similar flow dependence amongst these quantification methods.

The lower extraction fractions of the FA based methods correspond to lower K_1 values which likely resulted from blood input functions with higher intensity peaks due to recovery correction which was not performed in the ROI method. Biases in K_1 are offset by calibrating the extraction function to a standard as was performed in this work using ¹⁵O-water imaging.

6.4.5 Comparison to Previous Work

The accuracy of MBF from ⁸²Rb PET has been evaluated in previous works using other PET tracers or using microspheres. Microsphere measurements are typically conducted simultaneously with the PET image acquisition which is ideal, but are restricted to animal use since they require dissection and extraction of the heart. In humans, studies are often conducted with a PET tracer that has been previously validated in animals. Due to the length of multi-tracer exams and side-effects of pharmacologic stress agents, comparative studies are often conducted on separate days. Ideally the time interval between exams is kept short to mitigate changes in the health of participants, However, baseline variations in MBF may still be present due to diet, sleep patterns, stress levels, etc. In addition, co-registration of images may be compromised.

Table 6-4 lists previous work evaluating the accuracy of MBF using ⁸²Rb PET and reported Pearson correlation coefficients (r).

TABLE 6-4 – MBF CORRELATIONS REPORTED IN PREVIOUS WORK					
Work	**Reference**	**Time apart**	**Subjects**	**Data Points**	**Correlation**
Present work	Water	17±13 days	20	60	0.77
Katoh [55]	Water	n.a.	21	21×16segments	0.89
Lortie, [39]	Ammonia	<14 days	14	28	0.85
El Fakhri, [72]	Ammonia	<14 days	20	40×3segments	0.93
Herrero, [50]	Microspheres	Simultaneous	13 Dogs	36	0.91
Lautamäki, [69]	Microspheres	Simultaneous	9 Dogs	18	0.92

The correlation coefficients in this work are lower than correlation coefficients reported by others. The work of Katoh *et al.* [55] used nearly the same Rb and water data (one more subject but neglecting the CPT images) as in this work. The method of Katoh *et al.* involves significantly more operator intervention which may bias the results. The operator-dependent variability of this method has not been reported.

Lortie *et al.* [39] used the same method described in Chapter 3. The methods in this chapter and in Lortie *et al.* differ in the image used to define the ROI as discussed in section 6.4.3.

In Katoh *et al.*, Lortie *et al.*, and El Fakhri *et al.* the reference MBF and the Rb MBF were calculated using the same methods. Correlation could be high even though accuracy is reduced if the quantification method biases MBF values similarly with Rb and with the reference tracer. In this work several Rb quantification methods were evaluated, of which Rb-SOC was most similar to the water quantification method, but also had the lowest agreement parameter values, but not significantly.

The methods of Herrero *et al.* and Lautamäki *et al.* have been evaluated for accuracy using microspheres in dogs, but have not been reported in humans.

6.4.6 Limitation

Accuracy of MBF quantification using [82]Rb PET and factor analysis did not significantly improve over ROI-based methods. This may be partially due to the small number of patients, particularly in the high flow range. However, disagreements between water and Rb derived MBF in individuals were often high, which is reflected by the modest correlation coefficients ($r \approx 0.7$) and relatively high RC (≈ 2.5 mL/min/g). Agreement between water and Rb MBFs may be partially attributed to the long duration between imaging sessions. Ideally, imaging with both tracers should be conducted under identical conditions and on the same day.

The use of ^{15}O-water PET as a gold-standard for non-invasive MBF quantification is well established [7,58,75,90,131,162], however, the accuracy of ^{15}O-water PET is also finite. The degree of agreement between MBF measurements with water and Rb PET is limited by the accuracy and precision of both methods. Water MBF is useful as a gold-standard so long as water is significantly more accurate than Rb. This work did not evaluate the accuracy of the MBF quantification using water, but reproduced a previously reported and accepted method. Several potential limitations of MBF quantification using water are noted.

Because water is not retained in the myocardium an uptake image with good delineating of myocardium and blood pool does not exist. Image decomposition can be useful to generate myocardium structures from which ROIs can be derived. With the FADS + MSO constraint that was applied in this work, not all the myocardium structures had sufficient contrast for automatic reorientation and segmentation, and some operator intervention was required. Another disadvantage of water imaging is that patient motion is difficult to notice or correct.

Finally, it was observed that the water images tended to be noisier than Rb images, which is likely due to water's diffusion property (high k_2 tracer kinetic model parameter). Instead of being extracted from the blood and retained in the myocardium as Rb, water diffused freely to all perfused tissues, and back into the blood. The concentration of activity in the myocardium region at late time frames is therefore lower than Rb, resulting in images that may be count poor.

6.4.7   TR in Small Hearts

Figure 6-14 shows the RC in the center of a sphere that is blurred with an isotropic Gaussian smoothing kernel. RC approaches unity when the sphere diameter is >3×FWHM of the blurring kernel. In a standard [82]Rb cardiac PET image, with 12 mm spatial resolution, this condition is met at the centre of any heart that is larger than 3.6 cm in diameter at its narrowest cross-section during systole (when heart diameter is smallest). This criterion may be relaxed slightly since the heart is fully contracted for only a fraction of the cardiac cycle [174]. Thus even in small adults [174,175], children, and large animals (e.g. dogs, and pigs >20 kg) this assumption may be valid.
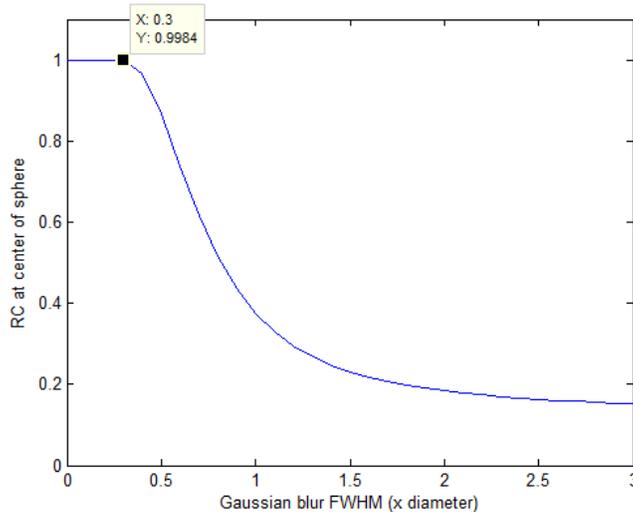
Figure 6-14 – Recovery coefficient at the center of a sphere with uniform activity with varying isotropic Gaussian blur. When the blur FWHM<diameter/3 nearly perfect RC is present at the center of the sphere.

In rats and mice a typical heart diameter is on the order of 10 and 7 mm respectively [174]. [82]Rb is not typically used in small animal imaging due to its long positron range and relatively low activity concentration. PET images using ^{18}F and a dedicated small-animal camera have resolutions on the order of 1.0-1.6 mm depending on the camera and reconstruction algorithm. Thus even in low resolution mouse images the TR scaling method may be applied.

6.4.8   TR in Other Organs

Factor analysis has been explored for quantification in other organs such as the brain [176], prostate [102], kidneys [164], liver [177]. Scaling of factors using TR may be applied in these organs, assuming they are sufficiently large compared to the image spatial resolution, that all the components in the organ region are accurately accounted for, and that the relative recovery of each component is heterogeneous. However, physiologically inaccurate structures may result in inaccurate recovery estimates. Therefore accuracy in each application should be evaluated before quantification is attempted.

6.4.9   Factor Analysis Reproducibility

Reproducibility of MBF using factor analysis is dependent on the reproducibility of the MBF over time, reproducibility of the imaging, and reproducibility of the analysis. It may not be possible to isolate the contribution of each of these elements on test-retest reproducibility. In the context of this work operator-dependent variability influences the reproducibility of image analysis and may be validated by repeat processing of the same images by the same and by different operators as was carried out in Chapter 3 for ROI-based MBF quantification.

In the proposed workflow, operator variability may involve manipulation of the ROI for factor analysis, in addition to optional operator interventions during the reorientation and LV segmentation stage. Ideally, the ROI should be broad enough to include the entire heart, including left and right blood cavities, but narrow enough to reduce contamination from neighbouring high uptake organs (e.g. stomach and liver). Inclusion of dixels with purest temporal response is expected to make the solution more numerically stable due to the non-negativity constraints [104,108].

The results in Chapter 5 indicate that myocardial structures, which are used for reorientation and segmentation, have superior myocardium to blood cavity contrast and less noise than uptake images. The use of myocardium images is therefore expected to improve reproducibility at these stages by minimizing the need for user intervention. Nevertheless, evaluation of operator-dependent variability and test-retest reproducibility are important characteristics of MBF quantification and should be investigated.

6.5 Conclusion

Evaluation of ^{82}Rb MBF accuracy as compared to ^{15}O-water derived MBF did not significantly benefit of factor analysis, but polar-map uniformity in normal individuals did significantly improve. Early evaluation of MBF quantification in patients using ^{82}Rb PET and factor analysis demonstrated that the increase in uniformity is not artificial and does not impair ability to detect regional defects. These results suggest that factor analysis derived blood input functions for MBF quantification with ^{82}Rb may be able to better detect true physiologic changes and may enable detecting CAD at earlier stages than standard ROI based methods.

Chapter 7.

Discussion and Future Directions

7.1 Summary

Coronary artery disease can be effectively treated with early detection and appropriate therapy. While MPI is routinely practiced in the clinic for detection of CAD, it can fail to detect narrowing in multiple coronary arteries when disease is severe. MPI may also be insensitive to detect diffused disease in the micro-vascular (the smallest blood vessels) which can slow delivery of nutrients to the cells and may be associated with early stages of disease. MBF quantification has long been sought as a means to detect multi-vessel disease and diffused micro-vessel disease, to track the progression of disease and response to therapy, to determine prognosis of the patient, and to guide therapy.

Cardiac PET is currently the gold-standard for non-invasive MBF quantification, but has only been used in the clinic on a limited basis, due its perceived high costs associated with installation and with the need for cyclotron produced tracers. The generator produced ^{82}Rb is a suitable tracer for MPI, but is less suited for MBF quantification due to incomplete extraction of the tracer and its physical properties which lead to reduced image spatial resolution.

Region of interest based methods have been used typically to measure image defined arterial blood and myocardial tissue TACs. The blood and myocardium TACs are used as input and output functions respectively to a kinetic model describing the transfer of activity between compartments. The blood-to-myocardium uptake rate constant K_1 along with other model parameters are optimized to fit the measured TACs. MBF is derived from K_1 using an extraction function that has been previously calibrated.

Greater reproducibility enables detection of smaller serial changes, which is important for tracking of disease and determining patient response to therapy. Chapter 3 described a highly automated ROI based method for MBF quantification that was developed to reduce operator-dependent variability and therefore improve reproducibility. Both inter- and intra-operator variability were evaluated using one novice and one expert user. The expert operator had more reproducible results than the novice operator emphasizing the need for adequate training and quality assurance. The inter- and intra-operator-dependent reproducibility of MBF was similar or better than previously reported methods. These findings were published in [132].

Accuracy is a second important characteristic of MBF quantification as it determines the ability to diagnose individuals through comparison to a database of normal MBF. The finite resolution of PET and the existence of arterial blood in the myocardium result in

spillover of signals between myocardial and blood ROIs. Spillover contaminates the TACs and can reduce the accuracy of MBF measurements. Factor analysis uses a mathematical model to decompose an image into distinct components based on unique temporal responses and may be able to correct spillover effects. Each component is modeled by the product of a spatial pattern (structure) and temporal response (factor).

Factor analysis does not guarantee unique solutions and therefore requires constraints to ensure a unique and accurate solution. In Chapter 4 the FADS (factor analysis of dynamic structures) method was constrained by minimizing the structure overlap (MSO) of the components and alternatively by minimizing the factor overlap (MFO) of the components. The MSO and MFO methods were compared using simulation and experimental data. Simulation results showed more accurate decomposition of the image using the MFO constraint. Simulated MSO myocardium factors were contaminated with blood signal, while the blood factors were recovered accurately. A series of images of the same dog were acquired under identical conditions, but with varying tracer infusion intervals. Thus the structures were expected to be reproducible, as confirmed using both MSO and MFO. MSO structures were more defined, had less spatial overlap, and had higher contrast between myocardium and blood pool when compared to MFO structures. MFO blood factors demonstrated more complete clearance from the blood at late time frames which is consistent with the physiology of an extracted tracer such as [82]Rb, suggesting that MFO results may be more physiologically accurate. The content of this chapter was published in [139].

While MSO partially violates our understanding of the physiology by assuming minimal spatial overlap of structures, there is no physiologic basis to support MFO either. In Chapter 5, a physiologically defined constraint was developed. The more general penalized-sum-of-least-squares frame work was used in place of FADS, and the tracer kinetic model was explicitly incorporated, giving rise to the model-based factor analysis (MB) method. The RV blood factor was a free parameter, LV blood factor was modeled as a delayed and dispersed RV blood factor using the gamma-variate model, and the myocardium factor was modeled using a 1-tissue-compartment model of tracer extraction. MB was also constrained to have decreasing blood factors in the late time frames. The MSO constraint was similarly integrated into the penalized-sum-of-least-squares frame work so that the two methods differed only in constraints. Both MSO and MB were evaluated and compared using simulated and experimental data.

Both canine and rodent cardiac structures were simulated, which differed in spatial dimensions, resolution, and cardiac motion – and therefore in the degree of spatial overlap of the structures. Canine simulations consisted of three components (RV blood, LV blood, and myocardium) and rodent simulation consisted of only two components (blood and myocardium). To evaluate if either method was biased, both canine and small animal simulations were generated with complete blood clearance and with residual blood activity. The simulation results indicated that MB was more accurate at resolving factors and

structures, particularly in small animals where structure overlap was more severe. MB results were also more reproducible in the presence of noise and were less variable between cases with complete blood clearance and residual blood activity.

Blood factors were evaluated using continuous arterial blood sampling performed simultaneously with image acquisition in rats. MB derived factors agreed more closely than MSO derived blood factor indicating better physiological accuracy. Accuracy of blood structures derived from dog images with variable ^{82}Rb infusion durations were evaluated using ^{11}CO blood pool imaging, and did not reveal significant differences between MB and MSO. MB did, however, resolve more reproducible blood and myocardium structures than MSO under variable tracer infusion durations.

K_1 and MBF were also measured from the same canine images and tended to be more reproducible using blood TACs derived from MB factors than either MSO derived or ROI derived blood TACs. MBF values derived using MB or MSO were significantly higher than ROI derived values, indicating a need to recalibrate the extraction function in order to achieve accurate MBF quantification. The content of Chapter 5 were also published in [145].

A comparison of the assumptions of the MSO, MFO, and MB methods is summarized in Table 7-1 along with their relative performance properties.

TABLE 7-1 – COMPARISON OF FA METHODS

Assumptions	MSO	MFO	MB
Number of factors is known	X	X	X
Non-negative factors	X	X	X
Non-negative structures	X	X	X
Minimal spatial overlap	X		
Minimal factor overlap		X	
Kinetic model (arterial blood to myocardial tissue)			X
Gamma-variate model (RV blood to LV blood)			X
Blood clearance			X
Performance Property	**MSO**	**MFO**	**MB**
Conforms to knowledge of physiology and physics	↓	↓	↑
Compatible with other tracers	↑	↑	↑ – with appropriate kinetic model
Compatible with other modalities	↑	↑	↓
Accuracy vs. simulation	↓↓	↓	↑
Accuracy of blood factors vs. arterial blood sampling	↓	n.a.	↑
Accuracy of blood structures vs. CO imaging	=	n.a.	=
Reproducibility of structures with varying tracer infusion	↓	↓	↑
MBF reproducibility	=	n.a	=
Myocardium:blood contrast	↑	↓	↓ – better than uptake images
Blood activity clearance	↓	↑	↑
Processing speed	↓	↓	↑

↑ - advantageous   ↓ - disadvantageous   = – equivalent between methods   n.a. – not available

The accuracy of MBF quantification using MB was addressed in Chapter 6 using ^{15}O-water as a gold-standard. While MBF accuracy did not improve significantly compared to ROI based methods, the polar-map uniformity was significantly improved in normals. MBF spatial patterns in patients indicated that the increased uniformity was not artificial. Thus image decomposition could be useful for detecting smaller regional MBF abnormalities than ROI based methods. These results were published in [158].

7.2 Future Work

Before these methods can be employed widely in research and clinical applications further validation of the MBF quantification is recommended. Future work could address the following issues.

7.2.1   Reproducibility

Precision of MBF can be evaluated through repeat measurement using test-retest experiments with representative subject populations for the desired application. For routine clinical applications test subjects should consist of patients with varying degrees of disease. A population of normals, having a low likelihood of disease, should also be considered, especially for research applications and for developing normal population databases for clinical interpretations.

To minimize experimental variability, repeat tests should be conducted under conditions that are as similar as possible. To reduce variability associated with disease progression, subject state, equipment calibration, and staffing, repeat image acquisitions should be conducted as closely as possible. Ideally, tests should be conducted in a single back-to-back session assuming that the state of subject can be maintained stable throughout the exam. Stability of the subject may be of particular concern during stress imaging due to patient fatigue, drug side-effects, and adaptation of the subject to the stressing agent.

In a clinical setting, MBF reproducibility data can be useful for determining confidence intervals on patient data for stratification of patients into risk groups. In research settings reproducibility data can be used to determine sample sizes needed to detect differences of a desired magnitude between groups. Alternatively, for a given sample size, the differences in MBF that can be reliably detected in repeat scans or between groups can be forecasted.

7.2.2   Accuracy in Patient Populations

In this work, accuracy of MBF was only evaluated in a normal, healthy population with a low likelihood of disease. Accuracy in a patient population should also be evaluated. While microsphere measurements are possible for animal applications, in human studies, a non-invasive standard such as ^{15}O-water PET imaging is ideal, and ^{13}N-ammonia is another

possible standard. Alternatively angiography data may be used to evaluate accurate classification of absence or presence of stenosis in the large coronary arteries using MBF.

7.2.3   Quality Assurance

Chapter 3 highlighted the importance of quality assurance of the MBF quantification process as the accuracy of MBF depends on successful application of the quantification process. MBF results alone may not always reveal a problem in the quantification process, and intermediate stages should also be reviewed. The methods described in Chapter 3 consisted of quality assurance reports for each stage. MBF quantification with factor analysis should include quality assurance of the factor-analysis and the factor scaling stages in addition to the reorientation, segmentation, and kinetic model stages described in Chapter 3. This work has only hinted at means of quality assurance during the factor-analysis stage that are based on intuition and anecdotal evidence.
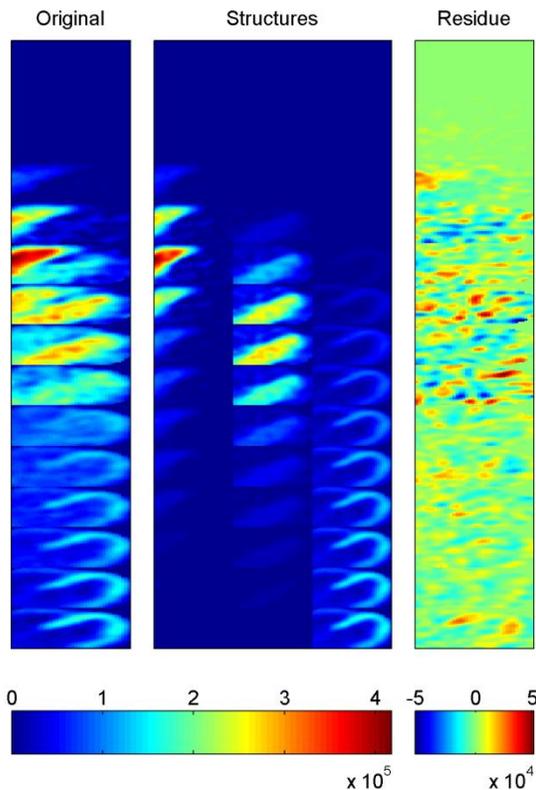
Figure 7-1 – A factor analysis report of a clinical patient showing a cropped transaxial slice through the mid-LV. The dynamic image sequence (Original) was successfully decomposed into three structures (RV blood, LV blood, and myocardium) as revealed by good quality structures and a residue signal with a random pattern. Time frames are from top to bottom.
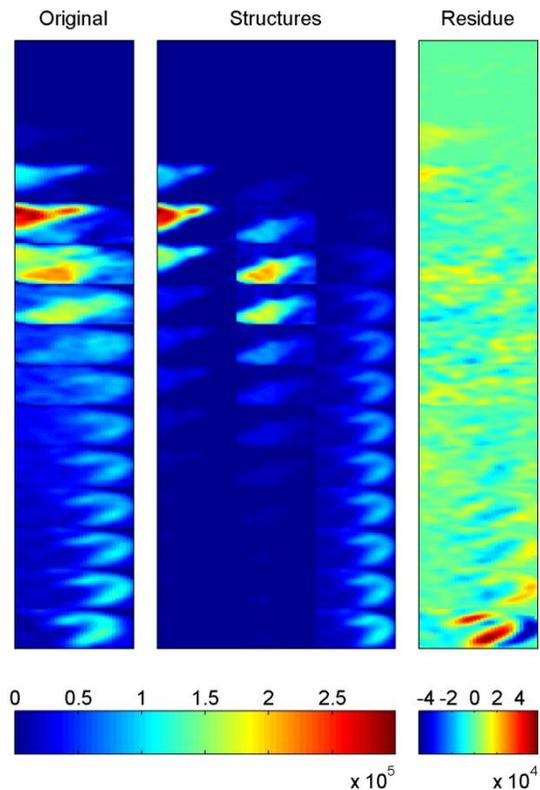
Figure 7-2 – A factor analysis report of a clinical patient showing a cropped transaxial slice through the mid-LV. The image was not well decomposed as indicated by an obvious pattern resembling the LV myocardium in the residue, primarily in the last time frame (bottom). Corresponding motion in the dynamic image (original) is apparent.

An example factor analysis report is demonstrated in Figure 7-1 and Figure 7-2. The residual signal should be inspected for prominent structures that would indicate incomplete decomposition of the image, which may be addressed in some cases by increasing the number of factors. The structures should be visually inspected for obvious anatomical abnormalities, or inappropriate splitting of a single anatomical component into multiple structures, which may be addressed by reducing the number of factors.

A QA report for scaling of structures to recovery units is shown in Figure 7-3. Mid-myocardial horizontal-long-axis slices in the scaled structures as well as their total, which estimates TR, can indicate to the operator cases where scaling may have failed. The TR image should be uniformly scaled to ~1 in the heart regions as demonstrated in Figure 7-3. A histogram of estimated and fitted TR values may also be informative.

The scaling QA could also be used for visual inspection of the individual structures. Structures should correspondence with the known anatomy of the heart as is the case in Figure 7-3. Fragmented structures could indicate decomposition to too many factors and may be addressed by reducing the number of factors. Thus the decomposition report and the scaling reports can both be useful for evaluating the factor analysis results.
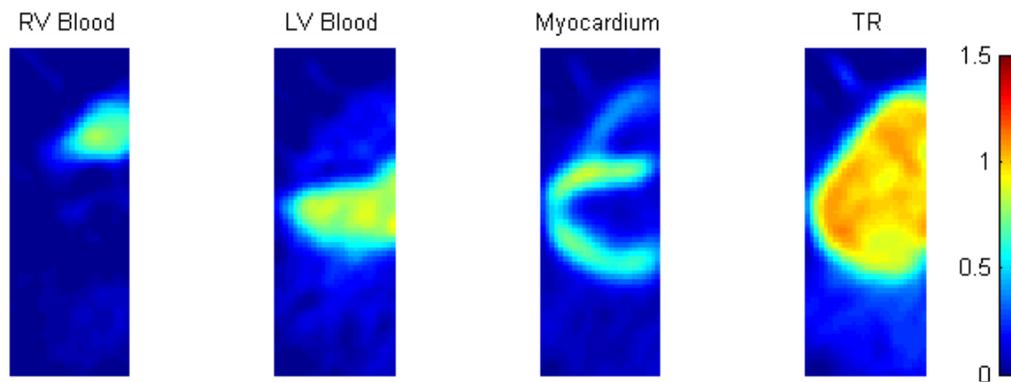
Figure 7-3 – Proposed QA report for scaling of structures to recovery units.

7.3 Clinical Considerations

The increasing prevalence of cardiac disease, reduction in price of PET equipment and [82]Rb, and reimbursement of MPI have all contributed to increase the adoption of [82]Rb PET MPI in recent years. In addition, the demand for routine MBF quantification is increasing and can be conducted without significant increased expenses or study complexity. As [82]Rb PET becomes more prevalent the need for standardization of image acquisition protocols will become more important for comparative studies, multicenter collaboration, and standardized patient reporting.

Standardization should include consideration of tracer infusion including imaging mode (2D or 3D), amount of activity, and infusion time. Since dynamic imaging is required

for MBF quantification, the infusion must be optimized to maximize the activity in the late time frames and to avoid camera saturation in the early time frames.

7.3.1   Imaging Protocol

The number of time frames and their durations, as well as the tracer infusion durations have not been optimized. While short time frames can better resolve fast changes in tracer concentrations, they do so at the expense of image quality. With more efficient, high-count-rate systems, it may be advantageous to shorten the early imaging time frames to 5 s [54,72,75,101], while some have used time frames as short as 0.5 s [54]. A more practical limitation to shortening the duration of time frames is the increased computation cost associated with the increase in number of frames to reconstruct.

An alternative approach could be to lengthen the interval over which [82]Rb is administered so that the difference between RV blood and LV blood TACs becomes negligible (as demonstrated by the variable infusion duration results of Chapter 5) mitigating the potential need to model separate spillover coefficients (*RVBF* and *LVBF* in Chapter 6) [178]. Long infusions can also reduce the high frequency components of the input function directly and of the output function indirectly, and therefore could overcome the need for many short time frames. With an extremely long elution, it may be possible to use a single equilibrium image to measure MBF using the ratio of myocardium and blood tissue concentrations, and possibly remove the need for factor analysis kinetic modelling entirely.

7.3.2   Image Reconstruction

Scanner technology and reconstruction algorithms are constantly evolving and improving the quality of reconstructed images. In general, images reconstructed with modern, iterative algorithms such as OSEM or MAP are considered superior to filtered back-projection images. In addition, iterative reconstruction methods are constrained to resolve non-negative pixel values in accordance with the known properties of tracer concentrations and consistent with the assumption of factor analysis methods [103,104,106]. However, since PET is most commonly used for tumour detection and tracking in static oncology studies, reconstruction algorithms may be optimized for contrast and resolution at the expense of accurate regional quantification [179,180]. Validation of TACs and/or factors should be considered when equipment or reconstructions are modified.

To overcome potential limitations due to reconstruction some have attempted to conduct factor analysis and kinetic modelling on the projection data (pre-reconstruction) [181]. Although a comparison of factor analysis on pre- and post-reconstruction data has been reported [90], it was limited to generating myocardium structures for image segmentation with ^{15}O-water. Manipulation of projection data may limit the operator's ability to reject organs that are not of interest from the analysis. It is not clear how factor analysis of pre- and post-reconstruction data compare for MBF quantification with [82]Rb.

7.4 Additional Utility of Factor analysis

The model based factor analysis method described in this work was designed for the specific purpose of quantifying MBF with [82]Rb PET. As discussed in Chapter 5, this method could be adapted to other tracers by incorporating their kinetic model. The software consists of an application programming interface (API) that can be used to rapidly prototype kinetic models for other tracers. The API accommodates models with and without RV blood spillover components as demonstrated in Chapter 6, and with and without an estimate of RC. The API also supports models for correcting blood TACs for accumulation of radio-labelled metabolites (e.g. ^{13}N-ammonia [182]). Since these kinetic models can be included as part of the decomposition process as well as the quantification process, both processes may benefit from accurate modeling of tracer kinetics.

In multi-tracer imaging protocols, sufficient delay is needed for tracer decay between exams. Factor analysis has been explored for multi-tracer applications to remove background activity from previous injections, provide rapid imaging in a single session, and therefore improve patient comfort and image co-registration [183,184]. For this application, the current form of MB is inappropriate, however a form with two independent input functions and associated tracer kinetic models could be conceived.

7.5 Validation Data

The need for a non-invasive, accurate, precise, affordable and readily available means to quantify MBF in a clinical setting persists. Currently [82]Rb PET is the most suitable technology to address this need, particularly in light of the recent shortage of SPECT isotopes. However, the biochemical and physical properties of [82]Rb limit its accuracy and precision. This work and that of others have proposed methods to overcome these limitations. After nearly two decades, application of MBF quantification with [82]Rb PET is still limited to research applications.

Clinical application of MBF quantification with [82]Rb PET has been limited due to a shortage of rigorous, large population data to support its diagnostic and prognostic value, as well a shortage of data to characterize its accuracy and precision in a diverse clinical setting. While several groups have developed MBF quantification methods, comparison is difficult or impossible due to a lack of standardization. The reported methods are evaluated using different species and populations and with a range of equipment, protocols, and reconstructions. In addition, the evaluation methods vary and rarely consist of accuracy, precision, and reproducibility measures. In addition, the datasets are often too small to instil confidence.

The following data could be useful to validate factor analysis and MBF quantification results using [82]Rb PET. Variations of these experiments could also be useful to factor analysis and physiological function quantification with other tracers and organs.

7.5.1   Animal Studies

Imaging of large animals (e.g. dogs or pigs) using ^{82}Rb can generate images with similar attenuation, scatter, anatomy, and physiology as humans and are therefore accepted evaluation methods. In addition, controlled disease states can be induced in animals. A comprehensive imaging protocol is proposed in Figure 7-4 consisting of repeat ^{82}Rb acquisitions, $C^{15}O$ blood pool imaging, arterial blood sampling, and microsphere measurements. Repeated attenuation scans should be included between scans to avoid misregistration between attenuation and emission data due to motion.
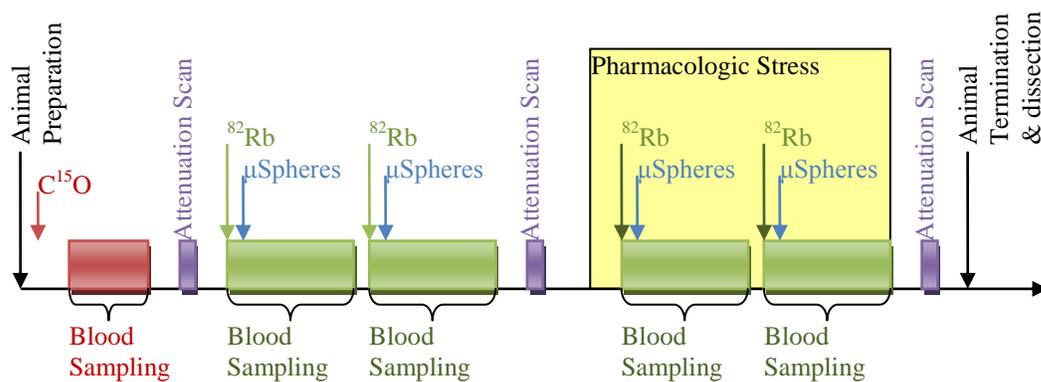
Figure 7-4 – Proposed image acquisition protocol for a factor analysis and MBF validation experiment using ^{82}Rb in a large animal.

MBF reproducibility can be evaluated using repeat acquisitions with ^{82}Rb under constant imaging conditions, while sets of rest and stress measurement can be used to evaluate MFR reproducibility. Reproducibility of factor analysis derived structures can also be evaluated using all (rest and stress) image sets.

With the addition of a $C^{15}O$ blood pool image acquisition in the same session, blood structures can be evaluated for anatomical accuracy. The activity concentration could be measured in a blood sample taken during the $C^{15}O$ image acquisition and used to convert the blood pool images to units of recovery, which could be used to validate scaling of the blood structures. This requires quantitative calibration of the camera.

Arterial blood sampling can be conducted simultaneously with ^{82}Rb image acquisition in order to validate arterial blood factors. With proper calibration, blood factors can be validated not only for temporal shape, but also for scaling. Blood samples must be corrected for background activity, for transport delay from the end of the catheter to the detector, and for radio-active decay. Since blood pool sampling requires insertion of a catheter to the aorta or left atrium via an artery, surgery is required and the animal may need to be terminated at the end of the exam.

Microspheres can be administered at the same time as ^{82}Rb injections in order to measure MBF for evaluating accuracy. The microspheres must be administered to the left

atrium through a catheter and a continuous, fixed flow rate withdrawal of blood must be conducted simultaneously at a distal artery (e.g. femoral artery) as a standard. At the end of the exam the animal must be terminated, the heart excised, and dissected to segments corresponding to image ROIs. To perform several microsphere measurements in the same animal, microspheres labelled with different radio-nuclides or fluorescent dyes must be used.

Validation of structures may also be possible using anatomical imaging modalities such as CT or MRI. These images would need to be acquired over all phases of the cardiac and respiratory cycles and averaged in order to account for cardiac and respiratory motion. In addition the images would require spatial smoothing to match the resolution of PET. Anatomical information may be useful for validating not only the shape of the structures, but potentially recovery correction and structure scaling as well.

7.5.2   Human Studies

Validation studies in humans are limited to minimally-invasive measurements. Accuracy and test-retest (including operator-dependent variability) studies are of key concern for characterization of MBF measurements. Large cohorts and diverse populations are required to understand the incremental value of MBF and to instil confidence, which would support clinical use of MBF. Participant cohorts should consist of both sexes, a range of ages, and a range of disease states. Multicentre trials are most likely to produce such data.

7.5.3   Clinical Trials

Once MBF is reported routinely, guidelines for clinical interpretation will undoubtedly need to be developed and evaluated. Evaluation will include accuracy of diagnosis using standards such as angiography to confirm interpretation of disease in the large coronary arteries. In addition, inter- and intra-reader reproducibility will be of interest to evaluate the robustness of MBF based reporting.

Retrospective studies may be useful to give first indications of the added diagnostic and prognostic benefit of clinical utility of MBF. Data on patients, with past scans and whose outcomes are already known can be evaluated to determine MBF's ability to forecast patients' outcomes (prognosis) such as myocardial infractions or death. In addition, these data could be used to develop guidelines for treatment planning based on MBF interpretation.

Current trends indicate that widespread clinical use of MBF may still be a few years away. Only after MBF is available routinely in the clinic can prospective and follow-up studies be conducted. These studies will ultimately determine the true value of MBF quantification for affecting patient outcome.

References

[1] T. Thom, N. Haase, W. Rosamond, V. J. Howard, J. Rumsfeld, T. Manolio, Z.-J. Zheng, K. Flegal, C. O'Donnell, S. Kittner, D. Lloyd-Jones, D. C. Goff, and Y. Hong, "Heart disease and stroke statistics - 2006 update", *Circ.*, vol. 113, pp. e85-151, 2006.

[2] C. J. Murray and A. D. Lopez, "Global mortality, disability, and the contribution of risk factors: Global burden of disease study", *Lancet*, vol. 349, no. 9063, pp. 1436-42, 1997.

[3] M. Gulati, D. K. Pandey, M. F. Arnsdorf, D. S. Lauderdale, R. A. Thisted, R. H. Wicklund, A. J. Al-Hani, and H. R. Black, "Exercise capacity and the risk of death in women", *Circ.*, vol. 108, pp. 1554-9, 2003.

[4] G. A. Mensah and D. W. Brown, "An Overview Of Cardiovascular Disease Burden In The United States", *Health Affects*, vol. 26, no. 1, pp. 38-48, 2007.

[5] K. Yoshinaga, C. Katoh, K. Noriyasu, Y. Iwado, H. Furuyama, Y. Ito, Y. Kuge, T. Kohya, A. Kitabatake, and N. Tamaki, "Reduction of coronary flow reserve in areas with and without ischemia on stress perfusion imaging in patients with coronary artery disease: a study using oxygen 15–labeled water PET", *J. Nuc. Cardiol.*, vol. 10, no. 3, pp. 275-83, 2003.

[6] M. F. Di Carli, S. Dorbala, J. Meserve, G. El Fakhri, A. Sitek, and S. C. Moore, "Clinical myocardial perfusion PET/CT", *J. Nucl. Med.*, vol. 48, no. 5, pp. 783-93, 2007.

[7] K. Yoshinaga, N. Tamaki, T. D. Ruddy, R. A. deKemp, and R. S. B. Beanlands, "Evaluation of Myocardial Perfusion," in *Principles and Practice of PET and PET/CT*, 2nd ed., R. L. Wahl, Ed. Philadelphia, PA, USA: Lippincott Williams & Wilkins, 2009, ch. 11.1, pp. 541-64.

[8] J. B. Bassingthwaighte, R. B. King, and S. A. Roger, "Fractal nature of regional myocardial blood flow heterogeneity", *Circ. Res.*, vol. 65, pp. 578-590, 1989.

[9] L.H. Opie, *The heart physiology and metabolism*, 2nd ed. New York, New York: Raven Press, 1991.

[10] K. Yoshinaga, B. J. W. Chow, K. Williams, L. Chen, R. A. deKemp, L. Garrard, A. L.-T. Szeto, M. Aung, R. A. Davies, T. D. Ruddy, and R. S. B. Beanlands, "What is the prognostic value of myocardial perfusion imaging using rubidium-82 positron emission tomography?", *J. Am. Coll. of Cardiol.*, vol. 48, no. 5, pp. 1029-39, 2006.

[11] F. Hermansen and A. A. Lammertsma, "Linear dimension reduction of sequences of medical images: I. Optimal inner products", *Phys. Med. Biol.*, vol. 40, pp. 1909-20, 1995.

[12] R. A. Tio, A. Dabeshlim, H.-M. J. Siebelink, J. de Sutter, H. L. Hillege, C. J. Zeebregts, R. A. J. O. Dierckx, D. J. van Veldhuisen, F. Zijlstra, and R. H. J. A. Slart, "Comparison between the prognostic value of left ventricular function and myocardial perfusion reserve in patients with ischemic heart disease", *J. Nucl. Med.*, vol. 50, no. 2, pp. 214-9, 2009.

[13] F. Dayanikli, D. Grambow, O. Muzik, L. Mosca, M. Rubenfire, and M. Schwaiger, "Early detection of abnormal coronary flow reserve in asymptomatic men at high risk for coronary artery disease using positron emission tomography", *Circ.*, vol. 90, no. 2, pp. 808-17, 1994.

[14] T. H. Schindler, E. U. Nitzsche, H. R. Schelbert, M. Olschewski, J. Sayre, M. Mix, I. Brink, X.-L. Zhang, M. Kreissl, N. Magosaki, H. Just, and U. Solzbach, "Positron emission tomography-measured abnormal responses of myocardial blood flow to sympathetic stimulation are associated with the risk of developing cardiovascular events", *J. Am. Coll. Cardiol.*, vol. 45, no. 9, pp. 1505-12, 2005.

[15] F. M. Bengel, T. Higuchi, M. S. Javadi, and R. Lautamäki, "Cardiac positron emission tomography", *J. Am. Coll. Cardiol.*, vol. 54, no. 1, pp. 1-15, 2009.

[16] M. E. Phelps, *PET: Physics, Instrumentation, and Scanners*. New York: Springer, 2006.

[17] G.V. Heller, D. Calnon, and S. Dorbalba, "Recent advances in cardiac PET and PET/CT myocardial perfusion imaging", *J. Nucl. Med.*, vol. 16, no. 6, p. 962, 2009.

[18] R. Bergmann and B. E. Sobel, *Positron Emission Tomography of the Heart.*: Futura Publishing Inc., 1992.

[19] I. Koike, M. Ohmura, M. Hata, N. Takahashi, T. Oka, I. Ogino, J. Lee, T. Umezawa, K. Kinbara, K. Watai, Y. Ozawa, and T. Inoue, "FDG-PET scanning after radiation can predict tumor regrowth three months later", *Int. J. of Radiation Oncology Biology Physics*, vol. 57, no. 5, pp. 1231-8, 2003.

[20] J. N. Talbot, Y. Petegnief, K. Kerrou, F. Montravers, D. Grahek, and N. Younsi, "Positron emission tomography with [18F]-FDG in oncology", *Nucl. Inst. and Meth. in Phys. Res.*, vol. 504, no. 1-3, pp. 129-138, 2003.

[21] K. Mah, C. B. Caldwell, Y. C. Ung, C. E. Danjoux, J. M. Balogh, S. N. Ganguli, L. E. Ehrlich, and R. Tirona, "The impact of 18 FDG-PET on target and critical organs in CT-based treatment planning of patients with poorly defined non-small-cell lung carcinoma: a prospective study", *Int. J. of Radiation Oncology Biology Physics*, vol. 52, no. 2, pp. 339-350, 2002.

[22] R. S. Beanlands, "Positron emission tomography in cardiovascular disease", *Can. J. Cardiology*, vol. 12, no. 10, pp. 875-883, 1996.

[23] M. R. Costanzo, S. Augustine, and R. Bourge, "Selection and treatment of candidates for heart transplants", *Circulation*, vol. 92, pp. 3593-612, 1995.

[24] H. Schelbert, R. Bonow, E. Geltman, J. Maddahi, and M. Schwaiger, "Position statement. Clinical use of cardiac positron emission tomography", *J. Nucl. Med.*, vol. 34, pp. 1385-8, 1993.

[25] K. Baete, J. Nuyts, W. Van Paesschen, P. Suetens, and P. Dupont, "Anatomical-based FDG-PET reconstruction for the detection of hypo-metabolic regions in epilepsy", *IEEE Trans. on Med. Imag.*, vol. 23, no. 4, pp. 510-9, 2004.

[26] C. K. Yen, Y. Yano, T. F. Budinger, R. P. Friedland, S. E. Derenzo, R. H. Huesman, and H. A. O'Brien, "Brain tumor evaluation using Rb-82 and positron emission tomography", *J. Nucl. Med.*, vol. 6, no. 23, pp. 532-7, 1982.

[27] T. Jones, "Clinical uses of 82Sr/82Rb generators", *Appl. Radiat. and Isot.*, vol. 38, no. 3, pp. 171-3, 1987.

[28] A. P. Selwyn, R. M. Allan, A. L'Abbate, P. Horlock, P. Caminci, J. Clark, H. A. O'Brien, and P. M. Grant, "Relation between regional myocardial uptake of rubidium-82 and perfusion: absolute reduction of cation uptake in ischemia", *J. Am. Cardiol.*, vol. 50, no. 1, pp. 112-21, 1982.

[29] E. M. Renkin, "Transport of potassium-42 from blood to tissue isolated mammalian skeletal muscles", *Am. J. Physiol.*, vol. 197, pp. 1205-10, 1959.

[30] C. Crone, "Permeability of capillaries in various organs as determined by use of the indicator diffusion method", *Acta. Physiol. Scand.*, vol. 58, pp. 292-305, 1963.

[31] T. M. Alvarez-Diez, R. A. deKemp, R. S. Beanlands, and J. Vincent, "Manufacture of strontium-82/rubidium-82 generators and quality control of rubidium-82 chloride for myocardial perfusion imaging in patients using positron emission tomography", *Appl. Radiat. Isot.*, vol. 50, no. 6, pp. 1015-23, 1999.

[32] R. E. Patterson, R. L. Eisner, and S. F. Horowitz, "Comparison of cost-effectiveness and utility of excercise ECG, single photon emission computer tomography, positron emission tomography, and coronary angiography for diagnosis of coronary artery disease", *Circulation*, vol. 91, pp. 54-65, 1995.

[33] J. Maddahi and S. S. Gambhir, "Cost-effective selection of patients for coronary angiography", *J. Nucl. Cardiol.*, vol. 4, pp. S141-51, 1997.

[34] M. E. Merhige, W. J. Breen, V. Shelton, T. Houston, B. J. D'Arcy, and A. F. Perna, "Impact of myocardial perfusion imaging with PET and (82)Rb on downstream invasive procedure utilization, costs, and outcomes in coronary disease management", *J. Nucl. Med.*, vol. 48, no. 7, pp. 1069-76, 2007.

[35] R. Klein, A. Adler, R. S. Beanlands, and R. A. deKemp, "Precision-controlled elution of a 82Sr/82Rb generator for cardiac perfusion imaging with positron emission tomography", *Phys. Med. Biol.*, vol. 52, pp. 659-73, 2007.

[36] R. deKemp, R. Klein, M. Lortie, and R. Beanlands, "Constant-activity-rate infusions for myocardial blood flow quantification with 82Rb and 3D PET", *IEEE NSS-MIC Conference Record*, vol. 6, pp. 3519-21, 2006.

[37] A. A. Lammertsma, "Myocardial perfusion in 3 dimensions", *J. Nucl. Med.*, vol. 48, no. 8, pp. 1041-3, 2002.

[38] R. A. deKemp, K. Yoshinaga, and R. S. B. Beanlands, "Will 3-dimensional PET-CT enable the routine quantification of myocardial blood flow?", *J. Nucl. Cardiol.*, vol. 14, no. 3, pp. 380-97, 2007.

[39] M. Lortie, R. S. B. Beanlands, K. Yoshinaga, R. Klein, J. N. DaSilva, and R. A. deKemp, "Quantification of myocardial blood flow with 82Rb dynamic PET imaging", *Eur. J. Nucl. Med. Mol. Imaging*, vol. 34, no. 11, pp. 1765-74, 2007.

[40] K. Yoshinaga, R. Klein, and N. Tamaki, "Generator produced rubidium-82 positron emission tomography myocardial perfusion imaging – From basic aspects to clinical applications", *J. Of Cardiol.*, vol. 55, no. 2, pp. 163-173, 2010, in press.

[41] K. Yoshida, N. Mullani, and L. G. Gould, "Coronary flow and flow reserve by PET simplified for clinical applications using rubidium-82 or nitrogen-13-ammonia," vol. 37, no. 10, pp. 1701-12, October 1996.

[42] R. Parkash, R. A. deKemp, T. D. Ruddy, A. Kitsikis, R. Hart, L. Beauschene, K. Williams, R. A. Davies, M. Labinaz, and R. S. B. Beanlands, "Potential utility of rubidium 82 PET quantification in patients with 3-vessel coronary artery disease", *J. Nucl. Cardiol.*, vol. 11, no. 4, pp. 440-9, 2004.

[43] R. J. Gropler and P. Soto, "Recent advances in cardiac positron emission tomography in clinical management of the cardiac patient," vol. 6, no. 1, pp. 20-26, 2004.

[44] K. L. Gould, "Quantification of coronary artery stenosis in vivo", *Circ. Res.*, vol. 57, no. 3, pp. 341-53, 1985.

[45] I. N. Weinberg, S. C. Huang, E. J. Hoffman, L. Araujo, C. Nienaber, M. Grover-McKay, M. Dahlbom, and H. Schelbert, "Validation of PET-acquired input functions for cardiac studies," *J Nucl Med*, vol. 29, no. 2, pp. 241-7, 1988.

[46] V. Dilsizian, S. L. Bacharach, R. S. Beanlands, S. R. Bergmann, D. Delbeke, R. J. Gropler, J. Knuuti, H. R. Schelbert, and M. I. Travin. (2009, July) http://www.asnc.org.

[47] M. D. Cerquiera, N. J. Weissman, V. Dilsizian, A. K. Jacobs, S. Kaul, W. K. Laskey, D. J. Pennell, J. A. Rumberger, T. Ryan, and M. S. Verani, "Standardized myocardial segmentation and nomenclature for tomographic imaging of the heart", *Circ.*, vol. 102, pp. 539-542, 2002.

[48] K. Zierler, "A critique of compartmental analysis," *Ann. Rev. Biophys. Bioeng.*, vol. 10, pp. 531-62, 1981.

[49] R. S. Beanlands, S. Thorn, J. N. DaSilva, T. Ruddy, and J. Maddahi, "Myocardial Viability," in *Principles and Practice of Positron Emission Tomography, second edition*, R. Wahl, Ed. Philadelphia: Lippincott Williams & Wilkins, 2009.

[50] P. Herrero, J. Markham, M. E. Shelton, and S. R. Bergmann, "Implementation and evaluation of a two-compartment model for quantification of myocardial perfusion with rubidium-82 and positron emission tomography", *Circ. Res.*, vol. 70, pp. 496-507, 1992.

[51] P. G. Coxson, R. H. Huesman, and L. Borland, "Consequences of using a simplified kinetic model for dynamic PET data", *J. Nucl. Med.*, vol. 38, no. 4, pp. 660-667, 1997.

[52] P. G. Coxson, K. M. Brennan, R. H. Huesman, S. Lim, and T. F. Budinger, "Variability and reproducibility of rubidium-82 kinetic parameters", *J. Nucl. Med.*, no. 36, pp. 287-96, 1995.

[53] K. Knešaurek, J. Machac, and Z. Zhang, "Repeatability of regional myocardial blood flow calculation in 82Rb PET imaging", *BMC Med. Phys.*, vol. 9, no. 1, p. 2, 2009.

[54] Y.- H. D. Fang and R. F. Muzic, "Spillover and partial-volume correction for image-derived input functions for small-animal 18F-FDG PET studies", *J Nucl Med*, vol. 49, no. 4, pp. 606-14, 2008.

[55] C. Katoh, K. Yoshinaga, O. Manabe, and N. Tamaki, "New quantification algorithm of regional myocardial blood flow with 82rubidium PET [abstract]", *J. Nucl. Med.*, vol. 49, no. suppl 1, p. 384P, 2008.

[56] G. D. Hutchins, J. M. Caraher, and R. R. Raylman, "A region of interest strategy for minimizing resolution distortions in quantitative myocardial PET studies", *J. Nucl. Med.*, no. 33, pp. 1243-50, 1992.

[57] N. A. Mullani, R. A. Goldstein, K. L. Gould, S. K. Marani, D. J. Fisher, H. A. O'Brien, and M. D. Loberg, "Myocardial perfusion with rubidium-82. I. Measurement of extraction fraction and flow with external detectors", *J. Nucl. Med.*, vol. 24, no. 10, pp. 898-906, 1983.

[58] C. Katoh, K. Morita, T. Shiga, N. Kubo, K. Nakada, and N. Tamaki, "Improvement of algorithm for quantification od regional myocardial blood flow using 15O-water with PET", *J. Nucl. Med.*, vol. 45, no. 11, pp. 1908-1916, 2004.

[59] H. R. Schelbert, M. E. Phelps, S. C. Huang, N. S. MacDonald, H. Hansen, C. Selin, and D. E. Kuhl, "N-13 Ammonia as an indicator of myocardial blood flow", *Circulation*, vol. 63, pp. 1259-72, 1981.

[60] R. S. B. Beanlands, O. Muzik, M. Mintun, T. Mangner, K. Lee, N. Petry, G. D. Hutchins, and M. Schwaiger, "The kinetics of copper-62-PTSM in the normal human heart", *J. Nucl. Med.*, vol. 33, no. 5, pp. 684-690, 1992.

[61] G. Glatting, K. P. Bergmann, J. C. Stollfuss, P. Weismueller, M. Kochs, V. Hombach, and S. N. Reske, "Myocardial Rb extraction fraction: determination in humans", *J. Am. Coll. Cardiol.*, vol. 25, pp. 364A-5A, 1995.

[62] M.E. Phelps, *PET: Molecular Imaging and It's Biological Application*. New York: Springer-Verlag New York, LLC, 2004.

[63] C. A. Wyss, P. Koepfli, K. Mikolajczyk, C. Burger, G. K. von Schulthess, and P. A. Kaufmann, "Bicycle exercise stress in PET for assessment of coronary flow reserve - repeatability and comparison with adenosine stress", *J. Nucl. Med.*, vol. 44, no. 2, pp. 146-54, 2003.

[64] G. D. Hutchins, M. Schwaiger, K. C. Rosenspire, J. Krivokapich, H. Schelbert, and D. E. Kuhl, "Noninvasive quantification of regional blood flow in the human heart using N-13 ammonia and dynamic positron emission tomographic imaging", *J. Am. Coll. Cardiol.*, vol. 15, no. 5, pp. 1032-42, 1990.

[65] H. Gerwitz, H. A. Skopicki, S. A. Abraham, H. Castano, R. E. Dinsmore, N. M. Alpert, and A. J. Fischman, "Quantitative PET measurements of regional myocardial blood flow: Observations in humans with ischemic heart disease", *Cardiology*, vol. 88, no. 1, pp. 62-70, 1997.

[66] R. A. deKemp, T. D. Ruddy, T. Hewitt, M. M. Dalipaj, and R. S. B. Beanlands, "Detection of serial changes in absolute myocardial perfusion with 82Rb PET", *J. Nuc. Med.*, vol. 41, no. 8, pp. 1426-35, 2000.

[67] P. A. Kaufmann and P. G. Camici, "Myocardial blood flow measurements by PET: Technical aspects and clinical applications", *J. Nucl. Med.*, vol. 46, no. 1, pp. 75-88, 2005.

[68] V. Schächinger, M. B. Britten, and A. M. Zeiher, "Prognostic impact of coronary vasodilator dysfunction on adverse long-term outcome of coronary heart disease", *Circ.*, vol. 101, pp. 1899-1906, 2000.

[69] R. Lautamäki, R. T. George, K. Kitagawa, T. Higuchi, J. Merrill, C. Voicu, A. DiPaula, S. G. Nekolla, J. A. C. Lima, A. C. Lardo, and F. M. Bengel, "Rubidium-82 PET-CT for quantitative assessment of myocardial blood flow: validation in a canine model of coronary artery stenosis", *Eur. J. Nucl. Med. Mol. Imaging*, vol. 36, pp. 576-86, 2009.

[70] R. A. deKemp, R. Klein, J. M. Renaud, A. Alghamdi, M. Lortie, J. DaSilva, and R. S. B. Beanlands, "3D listmode cardiac PET for simultaneous quantification of myocardial blood flow and ventricular function", *IEEE NSS-MIC Conference Record*, pp. 5215-8, 2008.

[71] S. V. Nestrov, C. Han, M. Mäki, S. Kajander, A. G. Naum, H. Helenius, I. Lisinen, H. Ukkonen, M. Pietilä, E. Joutsiniemi, and J. Knuuti, "Myocardial perfusion quantification with 15O-labeled water PET: high reproducibility of the new cardiac analysis software Carimas™)", *Eur. J. Nucl. Med. Mol. Imaging*, vol. 36, no. 10, pp. 1594-1602, 2009.

[72] G. El Fakhri, A. Kardan, A. Sitek, S. Dorbala, N. Abi-Hatem, Y. Lahoud, A. Fischman, M. Coughlan, T. Yasuda, and M. F. Di Carli, "Reproducibility and accuracy of quantitative myocardial blood flow assessment with 82Rb PET: Comparison with 13N-ammonia PET", *J. Nucl. Med.*, vol. 50, no. 7, pp. 1062-71, 2009.

[73] PMOD Technologies. [Online]. http://www.pmod.com

[74] G. D. Buckberg, J. C. Luck, D.B. Payne, J. I. E. Hoffman, J. P. Archie, and D. E. Fixler, "Some sources of error in measuring regional blood flow with radioactive microspheres", *J. Appl. Physiology*, vol. 31, no. 4, pp. 598-604, 1971.

[75] P. Herrero, J. Kim, T. L. Sharp, J. A. Engelbach, J. S. Lewis, R. J. Gropler, and M. J. Welch, "Assessment of myocardial blood flow using 15O-water and 1-11C-acetate in rats with small-animal PET", *J. Nucl. Med.*, vol. 47, no. 3, pp. 477-85, 2006.

[76] T. R. DeGrado, M. W. Hanson, T. G. Turkington, D. M. Delong, D. A. Brezinski, J.-P. Vallée, L. W. Hedlund, J. Zhang, F. Cobb, M. J. Sullivan, and R. E. Coleman, "Estimation of myocardial blood flow for longitudinal studies with 13N-labeled ammonia and positron emission tomography", *J. Nucl. Med.*, vol. 3, no. 6, pp. 494-507, 1996.

[77] O. Muzic, R. S. B. Beanlands, G. D. Hutchins, T. J. Mangner, N. Nguyen, and M. Schwaiger, "Validation of nitrogen-13-ammonia tracer kinetic model for quantification of myocardial blood flow using PET", *J. Nucl. Med.*, vol. 34, no. 1, pp. 83-91, 1993.

[78] K. S. Lekx, R. A. deKemp, R. S. B. Beanlands, G. Wisenberg, R. Glenn Wells, R. Z. Stodilka, M. Lortie, R. Klein, P. Zabel, M. Kovacs, S. Jane, and F. S. Prato, "Quantification of regional myocardial blood flow in a canine model of stunned and infarcted myocardium: comparison of rubidium-82 positron emission tomography with microspheres", *Nuclear Medicine Communications*, vol. 31, no. 1, pp. 67-74, 2010.

[79] F. Frouin, P. Merlet, Y. Bouchareb, V. Frouin, J.-L. Dubois-Rande, A. De Cesare, A. Herment, A. Syrota, and A. Todd-Pokropek, "Validation of myocardial perfusion reserve measurements using regularized factor images of H2-15O dynamic PET scans", *J. Nucl. Med.*, no. 42, pp. 1737-46, 2001.

[80] A. Kolin, "An electromagnetic catheter blood flow meter of minimal lateral dimensions", *Proc. Natl. Acad. Sci. USA*, vol. 66, no. 1, pp. 53-6, 1970.

[81] O. Manabe, K. Yoshinaga, C. Katoh, M. Naya, R. A. deKemp, and N. Tamaki, "Repeatability of rest and hyperemic myocardial blood flow measurements with 82Rb dynamic PET", *J. Nucl. Med*, vol. 50, no. 1, pp. 68-71, 2009.

[82] P. Chareonthaitawee, S. D. Christenson, J. L. Anderson, B. J. Kemp, D. O. Hodge, E. L. Ritman, and R. J. Gibbons, "Reproducibility of measurements of regional myocardial blood flow in a model of coronary artery disease: Comparison of H2 15O and 13NH3 PET techniques", *J. Nucl. Med.*, vol. 47, no. 7, pp. 1193-1201, 2006.

[83] M. Di Carli, J. Czernin, C. K. Hoh, V. H. Gerbaudo, R. C. Brunken, S.-C. Huang, M. E. Phelps, and H. R. Schelbert, "Relation among stenosis severity, myocardial blood flow, and flow reserve in patients with coronary artery disease", *Circ.*, vol. 91, pp. 1944-1951, 1995.

[84] N. S. Scott, M. R. Le May, R. A. deKemp, T. D. Ruddy, M. Labinaz, J.-F. Marquis, L. A. Laramee, E. R. O'Brien, W. L. Williams, L. A. Higginson, and R. S. B. Beanlands, "Evaluation of myocardial perfusion using rubidium-82 positron emission tomography after myocardial infarction in patients receiving primary stent implantation or thrombolytic therapy", *Am. J. Cardiol.*, vol. 88, no. 8, pp. 886-9, 2001.

[85] S. Sawada, O. Muzik, R. S. Beanlands, E. Wolfe, G. D. Hutchins, and M. Schwaiger, "Interobserver and interstudy variability of myocardial blood flow and flow-reserve measurements with nitrogen 13 ammonia-labeled positron emission tomography", *J. Nucl. Med.*, vol. 2, no. 5, pp. 413-22, 1995.

[86] S. Nagamachi, J. Czernin, A. S. Kim, K. T. Sun, M. Böttcher, M. E. Phelps, and H. R. Schelbert, "Reproducibility of measurements of regional resting and hyperemic myocardial blood flow assessed with PET", *J. Nucl. Med.*, vol. 37, no. 10, pp. 1626-31, 1996.

[87] P. A. Kaufmann, T. Gnecchi-Ruscone, J. T. Yap, O. Rimoldi, and P. G. Camici, "Assessment of reproducibility of baseline and hyperemic myocardial blood flow measurements with 15O-labeled water and PET", *J. Nucl. Med.*, vol. 40, no. 11, pp. 1848-56, 1999.

[88] R. Jagathesan, P. A. Kaufmann, S. D. Rosen, O. E. Rimoldi, F. Turkeimer, R. Foale, and P. G. Camici, "Assessment of the long-term reproducibility of baseline and dobutamine-induced myocardial blood flow in patients with stable coronary artery disease", *J. Nucl. Med.*, vol. 46, no. 2, pp. 212-19, 2005.

[89] T. H. Schindler, X.-L. Zhang, J. O. Prior, J. Cadenas, M. Dahlbom, J. Sayre, and H. R. Schelbert, "Assessment of intra- and interobserver reproducibility of rest and cold pressor test-stimulated myocardial blood flow with 13N-ammonia and PET", *Eur. J. Nucl. Med. Mol. Imaging*, vol. 34, pp. 1178-88, 2007.

[90] I. Adachi, O. Gaemperli, I. Valenta, T. Schepis, P. T. Siegrist, V. Treyer, C. Burger, K. Morita, and P. A. Kaufmann, "Assessment of myocardial perfusion by dynamic O-15-labeled water PET imaging: Validation of a new fast factor analysis", *J. Nucl. Cardiol.*, vol. 14, no. 5, pp. 698-705, 2007.

[91] G. Germano, P. B. Kavanagh, H.-T. Su, M. Mazzanti, H. Kiat, R. Hachamovitch, K. F. Van Train, J. S. Areeda, and D. S. Berman, "Automatic reorientation of three-dimensional, transaxial myocardial perfusion SPECT images", *J. Nucl. Med.*, vol. 36, no. 6, pp. 1107-14, 1995.

[92] R. Wassenaar, "Extravascular density imaging for regional partial volume correction of 18FDG cardiac PET images," Ottawa, ON, ISBN 0494083530, 2005.

[93] O. Rousset, A. Rahmim, A. Alavi, and H. Zaidi, "Partial volume correction strategies in PET", *PET Clinics*, vol. 2, no. 2, pp. 235-249, 2007.

[94] A. Rahmim, O. Rousset, and H. Zaidi, "Strategies for motion tracking and correction in PET", *PET Clinics*, vol. 2, no. 2, pp. 289-294, 2007.

[95] F. Lamare, M. J. Ledesma Carbayo, T. Cresson, G. Kontaxakis, A. Santos, C. Cheze Le Rest, A. J. Reader, and D. Visvikis, "List-mode-based reconstruction for respiratory motion correction in PET using non-rigid body transformations", *Phys. Med. Biol.*, vol. 52, pp. 5187-5204, 2007.

[96] A. J. Reader, "The promise of new PET image reconstruction", *Physica Medica*, vol. 24, pp. 49-56, 2008.

[97] J. Ma, "Deconvolution using singular integral regularization and curvelet shrinkage", *Physics Letters A*, vol. 368, no. 3-4, pp. 245-250, 2007.

[98] M. Ahmad and A. Todd-Pokropek, "Non-uniform resolution recovery using median priors in tomographic image reconstruction methods," in *Computer Analysis of Images and Patterns*. Berlin / Heidelberg: Springer, 2007, pp. 270-277.

[99] H. W. Müller-Gärtner, J. M. Links, J. L. Prince, R. N. Bryan, E. McVeigh, J. P. Leal, C. Davatzikos, and J. J. Frost, "Measurement of radiotracer concentration in brain gray matter using positron emission tomography: MRI-based correction for partial volume effects.", *J. Cereb. Blood Flow Metab.*, vol. 12, pp. 571-83, 1992.

[100] K.-H. Su, J.-S. Lee, J.-H. Li, Y.-W. Yang, R.-S. Liu, and J.-C. Chen, "Partial volume correction of the microPET blood input function using ensemble learning independent component analysis", *Phys. Med. Biol.*, vol. 54, pp. 1823-46, 2009.

[101] J. Kim, P. Herrero, T. Sharp, R. Laforest, D. J. Rowland, Y.-C. Tai, J. S. Lewis, and M. J. Welch, "Minimally invasive method of determining blood input function from PET images in rodents", *J. Nucl. Med.*, vol. 47, no. 2, pp. 330-6, 2006.

[102] C. Schiepers, C. K. Hoh, J. Nuyts, H.-M. Wu, M. E. Phelps, and M. Dahlbom, "Factor Analysis in Prostate Cancer: Delineation of Organ Structures and Automatic Generation of In- and Output Functions", *IEEE Trans. Nucl. Med.*, vol. 49, no. 5, pp. 2338-43, 2002.

[103] I. Buvat, H. Benali, and R. Di Paola, "Statistical Distribution of Factors and Factor Images in factor Analysis of Medical Image Sequences", *Phys. Med. Biol.*, vol. 43, pp. 1695-1711, 1998.

[104] I. Buvat, H. Benali, F. Frouin, J. P. Banzin, and R. Di Paola, "Target apex-seeking in factor analysis of medical image sequences", *Phys. Med. Biolo.*, vol. 38, pp. 123-138, 1993.

[105] E. E. Cureton and R. B. D'Argostino, *Factor Analysis, an Applied Approach*.: Lawrence Erlbaum Ass., 1983.

[106] G. El Fahkri, A. Sitek, B. Guerin, M. F. Kijewski, M. F. Di Carli, and S. C. Moore, "Quantitative Dynamic Cardiac 82Rb PET Using Generalized Factor and Compartment Analyses", *J. Nuc. Med*, vol. 8, no. 46, pp. 1264-71, 2005.

[107] F. Frouin, J.-P. Bazin, M. Di Paola, O. Jolivet, and R. Di Paola, "FAMIS: A software package for functional feature extraction from biomedical multideimensional images", *Computerized Medical Imanging and Graphics*, vol. 16, no. 2, pp. 81-91, 1992.

[108] A. Sitek, E. V. R. Di Bella, and G. T. Gullberg, "Factor analysis with a priori knowledge – application in dynamic cardiac SPECT", *Phys. Med. Biolo.*, vol. 45, pp. 2619-38, 2000.

[109] A. Sitek, E. V. R. Di Bella, G. T. Gullberg, and R. H. Huesman, "Removal of Liver Activity Contamination in Teboroxime Dynamic Cardiac SPECT Imaging with the Use of Factor Analysis", *J. Nucl. Cardiol.*, vol. 9, no. 2, pp. 197-205, 2002.

[110] H.-M. Wu, C. K. Hoh, Y. Choi, H. R. Schelbert, R. A. Hawkins, M. E. Phelps, and S.-C. Huang, "Factor analysis for extraction of blood time-activity curves in dynamic FDG-PET studies", *J. Nucl. Med.*, vol. 36, no. 9, pp. 1714-22, 1995.

[111] F. Hermansen, J. Ashburner, T. J. Spinks, J. S. Kooner, P. G. Camici, and A. A. Lammertsma, "Generation of myocardial factor images directly from the dynamic oxygen-15-water scan without use of oxygen-15-carbon monoxide blood-pool scan", *J. Nucl. Med.*, vol. 39, no. 10, pp. 1696-702, 1998.

[112] I. Buvat, S. Hapdey, H. Benali, A. Todd-Pokropek, and R. Di Paola, "Spectral factor analysis for multi-isotope imaging in nuclear medicine", *Conf. Proc. IPMI'99 LNCS*, vol. 1613, pp. 442-7, 1999.

[113] M. Bentourkia, "Kinetic modeling of PET data without blood sampling", *IEEE Trans. Nucl. Sci.*, vol. 25, no. 3, pp. 697-702, 2005.

[114] D. Bnaks, L. House, F. R. McMorris, P. Arabie, and W. Gaul, *Classification, Clustering, and Data Mining Applications*.: Springer, 2004.

[115] A. Hyvarinen and E. Oja, "Independent Component Analysis Algorithms and Applications", *Neural Netw.*, vol. 13, no. 4-5, pp. 411-30, 2000.

[116] R. Gorsuch, *Factor Analysis 2nd Edition*.: Lawrence Erlbaum Ass., 1983.

[117] M. J. Greenacre, *Correspondence Analysis in Practice*.: Academic Press Ltd., 1993.

[118] N. C. Nigiri, *Multivariate Statistical Analysis*.: Marcel Dekkers Inc., 2004.

[119] B. Thompson, *Exploratory and Confirmatory Factor Analysis*.: America Psychological Association, 2004.

[120] D. C. Barber, "The use of principal components in the quantitative analysis of gamma camera dynamic studies", *Phys. Med. Biol.*, vol. 25, no. 2, pp. 283-92, 1980.

[121] R. Di Paola, J.-P. Bazin, F. Aubry, A. Aurengo, F. Cavailloles, Y. Herry, and E. Kahn, "Handling of dynamic sequences in nuclear medicine", *IEEE Trans. Nucl. Med.*, no. 29, pp. 1310-21, 1982.

[122] H. Benali, I. Buvat, F. Frouin, J.-P. Bazin, and R. Di Paola, "A statistical model for the determination of optimal metric in factor analysis if medical image sequences (FAMIS)", *Phys. Med. Biol.*, no. 38, pp. 1065-80, 1993.

[123] F. Frouin, A. De Cesare, Y. Bouchareb, A. Todd-Pokropek, and A. Herment, "Spatial regularization applied to factor analysis of medical image sequences (FAMIS)", *Phys. Med. Biol.*, vol. 44, pp. 2289-306, 1999.

[124] A. Sitek, G. T. Gullberg, and R. H. Huesman, "Correction for Ambiguous Solutions in Factor Analysis Using Penalized Least Squares Objectives", *IEEE Trans. Med. Imag.*, vol. 21, no. 3, pp. 216-225, 2002.

[125] F. Esposito, T. Scarabino, A. Hyarinen, J. Himberg, E. Formisano, S. Comani, G. Tedeschi, R. Goebel, E. Seifritz, and F. Di Salle, "Independent component analysis of fMRI group studies by self-organizing clustering", *NeoroImage*, vol. 25, pp. 193-205, 2005.

[126] H. H. Harman, *Modern Factor Analysis 3rd Edition*.: Uni. of Chicago Press, 1976.

[127] H.-M. Wu, C. K. Hoh, D. B. Buxton, W. G. Kuhle, H. R. Schelbert, Y. Choi, R. A. Hawkins, M. E. Phelps, and S.-C. Huang, "Quantification of myocardial blood flow using dynamic nitrogen-13-ammonia PET studies and factor analysis of dynamic structures", *J. Nucl. Med.*, vol. 36, no. 11, pp. 2087-2093, 1995.

[128] C. Schiepers, C. K. Hoh, H. M. Wu, M. Dahlbom, and M. E. Phelps, "Factor analysis for generation of input functions replaces blood sampling in tracer kinetic modeling", *J. Nucl. Med.*, vol. 39, p. S06, 1998.

[129] C. Schielpers, H. M. Wu, J. Nuyts, M. Dahlbom, C. K. Hoh, S. C. Huang, and M. E. Phelps, "Fluoride PET: Is noninvasive quantitation feasible with factor analysis?", *J. Nucl. Med.*, vol. 38, p. 93P, 1997.

[130] L. Convert, G. Morin-Bassard, J. Cadorette, M. Archambault, M. Bentourkia, and R. Lecomte, "A New Tool for Molecular Imaging: The Microvolumetric ß Blood Counter", *J. Nucl. Med.*, vol. 48, no. 7, pp. 1197-1206, 2007.

[131] J. Y. Ahn, D. S. Kee, J. S. Kee, S.-K. Kim, G. J. Cheon, J. S. Yeo, S.-A. Shin, J.-K. Chung, and M. C. Lee, "Quantification of regional myocardial blood flow using H2 15O PET and factor analysis", *J. Nucl. Med.*, vol. 42, no. 5, pp. 782-787, 2001.

[132] R. Klein, J. M. Renaud, M. C. Ziadi, S. L. Thorn, A. Adler, R. S. Beanlands, and R. A. deKemp, "Intra- and inter-operator repeatability of myocardial blood flow and myocardial flow reserve measurements using Rubdium-82 PET and a highly automated analysis program", *J. Nucl. Cardiol.*, 2010, In Press.

[133] S. G. Nekolla, C. Miethaner, N. Nguyen, S. I. Ziegler, and M. Schwaiger, "Reproducibility of polar map generation and assessment of defect severity and extent in myocardial perfusion imaging using postiron emission tomography", *Eur. J. Nucl. Med.*, vol. 25, no. 9, pp. 1313-21, 1998.

[134] R. Klein, M. Lortie, A. Adler, R. S. Beanlands, and R. A. deKemp, "Fully automated software for polar-map registration and sampling from PET images", *Nucl. Sci Symp. and Med. Imag. Conf. Record*, pp. 3185-8, 2006.

[135] H. Gerwitz, A. J. Fischman, S. Abraham, M. Gilson, H. W. Strauss, and N. M. Alpert, "Positron emission tomographic measurements of absolute regional myocardial blood flow permits identification of nonviable myocardium in patients with chronic myocardial infarction", *J. Am. Coll. Cardiol.*, vol. 23, pp. 851-59, 1994.

[136] D. G. Altman and J. M. Bland, "Measurement in medicine: the analysis of method comparison studies", *Statistician*, no. 32, pp. 307-17, 1983.

[137] R. E. Austin, G. S. Aldea, D. L. Coggins, A. E. Flynn, and J. I. E. Hoffman, "Profound spatial heterogeneity of coronary reserve - discordance between patterns of resting and maximal myocardial blood flow", *Circ. Res.*, vol. 67, no. 2, pp. 319-31, 1990.

[138] P. Chareonthaitawee, P. A. Kaufmann, O. Rimoldi, and P. G. Camici, "Heterogeneity of resting and hyperemic myocardial blood flow in healthy humans", *Circ. Res.*, vol. 50, no. 1, pp. 151-61, 2001.

[139] R. Klein, M. Bentourkia, R. R. S. Beanlands, A. Adler, and R. A. deKemp, "A minimal factor overlap method for resolving ambiguity in factor analysis of dynamic cardiac PET," in *Nucl Sci Symp Conf Record*, vol. 5, Honolulu, HI, 2007, pp. 3268-72.

[140] A. S. Houston, "The effect of apex-finding errors on factor images obtained from factor analysis and oblique transformation", *Phys. Med. biol.*, vol. 9, no. 29, pp. 1109-16, 1984.

[141] M. Samal, M. Karny, H. Surova, P. Penicka, E. Marikova, and Z. Dienstbier, "On the existence of an unambiguous solution in factor analysis of dynamic studies", *Phys. Med. Biol.*, vol. 2, no. 34, pp. 223-8, 1989.

[142] M. Van Daele, J. Joosten, P. Devost, A. Vandecruyst, J. L. Willems, and M. De Roo, "Background correction in factor analysis of dynamic scintigraphic studies: necessity and implementation", *Phys. Med. Biol.*, vol. 11, no. 35, pp. 1477-85, 1990.

[143] K. S. Nirjan and D. C. Barber, "Factor analysis of dynamic function studies using a priori physiological information", *Phys. Med. Biol.*, vol. 10, no. 31, pp. 1107-17, 1986.

[144] A. Sitek, E. V. R. Di Bella, and G. T. Gullberg, "Factor analysis of dynamic structures in dynamic SPECT imaging using maximum entropy", *IEEE Trans. Nucl. Sci.*, vol. 46, no. 6, pp. 2227-32, 1999.

[145] R. Klein, R. S. Beanlands, R. W. Wassenaar, S. Thorn, M. Lamoureux, J. N. DaSilva, A. Adler, and R. A. deKemp, "Kinetic model based factor analysis of dynamic sequences for 82-rubidium cardiac positron emission tomography", *Med. Phys.*, 2010, In Press.

[146] H. Benali, I. Buvat, F. Frouin, J. P. Bazin, and R. Di Paolo, "Foundations of factor analysis of medical image sequences: a unified appraoach and some practical implications", *Img. and Vis. Comp.*, vol. 12, no. 6, pp. 375-385, 1994.

[147] M. T. Madsen, "A Simplified Formulation of the Gamma Variate Function," *Phys. Med. Biol.*, vol. 37, no. 7, pp. 1597-1600, 1992.

[148] M. D. Harper and M. L. Lecklitner, "Derivation of gamma variate indicator dilution function from simple convective dispersion model of blood flow", *Med. Phys.*, vol. 11, no. 5, pp. 690-692, 1984.

[149] R. Davenport, "The Derivation of the Gamma-Variate Relationship for Tracer Dilution Curves", *J. Nucl. Med.*, vol. 24, no. 10, pp. 945-948, 1983.

[150] H. K. Thompson, C. F. Starmer, R. E. Whalen, and H. D. McIntosh, "Indicator Transit Time Considered as a Gamma Variate", *Circ. Res.*, vol. 14, no. 6, pp. 502-515, 1964.

[151] Q. Jinyi and R. M. Leahy, "Resolution and noise properties of MAP reconstruction for fully 3-D PET", *IEEE Trans. Med. Imaging*, vol. 19, no. 5, pp. 493-506, 2000.

[152] F. Xu, W. Wu, M. Jones, B. Keszthelyi, J. Sedat, D. Agard, and K. Mueller, "On the efficiency of iterative ordered subset reconstruction algorithms for acceleration on GPUs", *Computer Methods and Programs in Biomedicine*, In Press.

[153] M. J. Inman and A. Z. Elsherbeni, "Optimization and parameter exploration using GPU based FDTD solvers", *Microwave Symposium Digest, 2008 IEEE MTT-S International*, pp. 149-152, 2008.

[154] A. Ben-Tal, T. Margalit, and A. Nemirovski, "The Ordered Subsets Mirror Descent Optimization Method with Applications to Tomography", *SIAM J. on Optimization*, vol. 12, no. 1, pp. 79-108, 2001.

[155] C. Watson, C. Hayden, M. Casey, J. Hamill, and B. Bendriem, "Prompt gamma correction for improved quantification in 82Rb PET", *J. Nucl. Med.*, vol. 49, no. (Supplement 1), p. 64P, 2008.

[156] J. ven den Hoff, W. Burchert, H. G. Wolpers, G. J. Meyer, and H. Hundeshagen, "A kinetic model for cardiac PET with [1-carbon-11]-acetate", *J. Nucl. Med.*, vol. 37, no. 3, pp. 521-529, 1996.

[157] T. Wichter, M. Schäfers, C. G. Rhodes, M. Borggrefe, H. Lerch, A. A. Lammertsma, F. Hermansen, O. Schober, G. Breithardt, and P. G. Camici, "Abnormalities of cardiac sympathetic innervation in arrhythmogenic right ventricular cardiomyopathy : Quantitative assessment of presynaptic norepinephrine reuptake and postsynaptic ß-adrenergic receptor density with positron emission tomography", *Circ.*, vol. 101, pp. 1552-1558, 2000.

[158] R. Klein, K. Yoshinaga, C. Katoh, A. Adler, R. Beanlands, N. Tamaki, and R. deKemp, "Improved homogeneity of normal MBF using factor analysis with 82Rb PET", *S. Nucl. Med. Annual Meeting abstract* , 2010, In Press.

[159] J. S. Lee, D. S. Lee, J. Y. Ahn, G. J. Cheon, S. -K. Kim, J. S. Yeo, K. S. Park, J. -K. Chung, and M. C. Lee, "Parametric image of myocardial blood flow generated from dynamic H2 15O PET using factor analysis and cluster analysis", *Med. Biol. Eng. Comput.*, no. 43, pp. 678-85, 2005.

[160] R. B. King, J. B. Bassingthwaighte, J. R. S. Hales, and L. B. Rowell, "Stability of heterogeneity of myocardial blood flow in normal awake baboons", *Circ. Res.*, vol. 57, pp. 285-295, 1985.

[161] R. Klein, C. Katoh, K. Yoshinaga, A. Adle, R. B. S. Beanlands, and R. A. deKemp, "Evaluation of myocardium to blood pool spillover correction in quantification myocardial blood flow with 82Rb PET," in *World Molecular Imaging Conference*, Montreal, Quebec, 2009, In Press.

[162] H. Iida, I. Yokoyama, D. Agostini, T. Banno, T. Kato, K. Ito, Y. Kuwabara, Y. Oda, T. Otake, Y. Tamura, E. Tadamura, T. Yoshida, and N. Tamaki, "Quantitative assessment of regional myocardial blood flow using oxygen-15-labelled water and positron emission tomography: a multicentre evaluation in Japan", *Eur. J. Nucl. Med.*, vol. 27, no. 21, pp. 192-201, 2000.

[163] G. Z. Ferl, X. Zhang, H.-M. Wu, and S.-C. Huang, "Estimation of the 18F-FDG input function in mice by use of dynamic small-animal PET and minimal blood sample data", *J. Nucl. Med.*, vol. 48, no. 12, pp. 2037-2045, 2007.

[164] J.Y. Ahn, K. Seo, J.S. Lee, and D.S. Lee, "Factor analysis for the quantification of renal cortical blood flowusing O-15 water dynamic PET," in *Nuclear Science Symposium Conference Record*, vol. 3, Lyon, France, 2000, pp. 153-156.

[165] S.R. Bergmann, P. Herrero, J. Markham, C.J. Weinheimer, and M.N. Walsh, "Noninvasive quantitation of myocardial blood flow in human subjects with oxygen-15 labeled water and positron emission tomography," *J. Am. Coll. Cardiol.*, vol. 1414, p. 639–652, 1989.

[166] O. Rimoldi, K. P. Schafers, R. Boellaard, F. Turkheimer, L. Stegger, M. P. Law, A. A. Lammerstma, and P. G. Camici, "Quantification of subendocardial and sbepicardial blood flow using 15O-labled water and PET: Experimental validation," *J. Nucl. Med.*, vol. 47, no. 1, pp. 163-172, January 2006.

[167] J. S. Lee, D. S. Lee, J. Y. Ahn, J. S. Yeo, G. J. Cheon, S. -K. Kim, K. S. Park, J. -K. Chung, and M. C. Lee, "Generation of parametric images of regional blood flow using H2-15O dynamic PET and a linear least-squares method", *J. Nucl. Med.*, no. 46, pp. 1687-95, 2005.

[168] M. Naya, T. Tsukamoto, K. Morita, C. Katoh, T. Furumoto, S. Fujii, N. Tamaki, and H. Tsutsui, "Olmesartan, but not amlodipine, improves endothelium-dependent coronary dilation in hypertensive patients", *J. Am. Coll. Cardiol.*, vol. 50, pp. 1144-1149, 2007.

[169] P. T. Siegrist, O. Gaemperli, P. Koepfli, T. Schepis, M. Namdar, I. Valenta, F. Aillo, S. Fleischmann, H. Alkadhi, and P. A. Kaufmann, "Repeatability of cold pressor test-induced flow increase assessed with H(2)(15)O and PET", *J. Nucl. Med.*, vol. 47, pp. 1420-1426, 2006.

[170] H. Furuyama, Y. Odagawa, C. Katoh, Y. Iwado, K. Yoshinaga, Y. Ito, K. Noriyasu, M. Mabuchi, Y. Kuge, K. Kobayashi, and N. Tamaki, "Assessment of coronary function in children with a history of Kawasaki disease using (15)O-water positron emission tomography", *Circ.*, vol. 105, pp. 2878-2884, 2002.

[171] H. IIda, C.G. Rhodes, R. de Silva, L.I. Araujo, P.M. Bloomfield, A.A. Lammertsma, and Jones Terry, "Use of the left ventricular time-activity curve as a noninvasive input function in dynamic oxygen-15-water positron emission tomography," *J. Nucl. Med.*, vol. 33, no. 9, pp. 1669-1677, September 1992.

[172] H. Iida, I. Kanno, A. Takahashi, S. Miura, M. Murakami, K. Takahashi, Y. Ono, F. Shishido, A. Inugami, and N. Tomura, "Measurement of absolute myocardial blood flow with H215O and dynamic positron-emission tomography. Strategy for quantification in relation to the partial-volume effect," *Circ*, vol. 78, pp. 104-115, 1988.

[173] F.W. Prinzen, G.J. van der Vusse, and R.S. Reneman, "Blood flow distribution in the left ventricular free wall in open-chest dogs," *Basic Res. Cardiol.*, vol. 76, pp. 431-437, 1981.

[174] A. Wessels and D. Sedmera, "Developmental anatomy of the heart: a tale of mice and man", *Physiol. Genomics*, vol. 15, pp. 165-176, 2003.

[175] R.S. Snell, *Clinical anatomy for medical students*, 5th ed.: Little, Brown and Company, 1995.

[176] U. Kimura and P. Herscovitz, *Brain imaging using PET*, M. Senda, Y. Kimura, and P. Herscovitch, Eds.: Gulf Professional Publishing, 2002.

[177] S. Petras, A. Aurengo, D. Le, M. Di Paola, C. Jeanguillaume, and P. Galle, "Factor analysis in successive hepatobiliary imaging of native and transplant livers ", *J. Nucl.Med.*, vol. 37, no. 5, pp. 847-851, 1996.

[178] R. Klein, R.S. Beanlands, and R.A. deKemp, "Quantification of Myocardial Blood Flow and Flow Reserve - Technical Aspects", *J. Nucl. Cardiol.*, 2010, In Press.

[179] R. Boellaard, A. van Lingen, and A.A. Lammertsma, "Experimental and clinical evaluation of interative reconstruction (OSEM) in dynamic PET: Quantitative characteristics and effects on kinetic modeling", *J. Nucl. Med.*, vol. 42, no. 5, pp. 808-817, 2001.

[180] A. Seret, "Number of iterations whrn comparing MLEM/OSEM with FBP", *J. Nucl. Med.*, vol. 45, no. 12, pp. 2125-2126, 2004.

[181] M. Bentourkia, "PET kinetic modeling of 11C-acetate from projections", *Computerized Medical Imaging ang Graphics*, vol. 27, no. 5, pp. 373-379, 2003.

[182] A. Khorsand, S. Graf, C. Pirich, O. Muzik, K. Kletter, R. Dudczak, G. Maurer, H. Sochor, E. Schuster, and G. Porenta, "Assessment of myocardial perfusion by dynamic N-13 ammonia PET imaging: Comparison of 2 tracer kinetic models", *J. Nucl. Cardiol.*, vol. 12, no. 4, pp. 410-417, 2005.

[183] N.F. Black, S. McJames, and D.J. Kadrmas, "Rapid multi-tracer PET tumor imaging with 28F-FDG and secondary shorter-lived tracers", *IEEE Trans. Nucl. Sci.*, vol. 56, no. 5, pp. 2750-2758, 2009.

[184] G. El Fakhri, A. Sitek, and B. Guerin, "Simultaneous dual tracer PET using generalized factor analysis of dynamic sequences," *IEEE Nuclear Science Symposium Conference Record*, vol. 4, pp. 2128-2130, October 2006.

[185] M.F. Smith, "Advances in Rubidium PET and integrated imaging with CT angiography", *Current Cardiology Report*, vol. 10, pp. 135-141, 2008.